THERMALLY INDUCED VIBRATIONS DUE TO RUB IN REAL ROTORS

N. BACHSCHMID
Dipartimento di Meccanica,
Politecnico di Milano,
Via La Masa, 34, I-20156, Milano, Italy.
nicolo.bachschmid@polimi.it

P. PENNACCHI
Dipartimento di Meccanica,
Politecnico di Milano,
Via La Masa, 34, I-20156, Milano, Italy.
paolo.pennacchi@polimi.it

A. VANIA
Dipartimento di Meccanica,
Politecnico di Milano,
Via La Masa, 34, I-20156, Milano, Italy.
andrea.vania@polimi.it

RUB INDUCED VIBRATIONS IN REAL ROTORS

Pages: 37
Tables: 2
Figures: 48

Please send proofs to:
PROF. P. PENNACCHI
Dipartimento di Meccanica,
Politecnico di Milano,
Via La Masa, 34, I-20156, Milano, Italy.

SUMMARY

The analysis of the effects of the rotor-to–stator rub in the rotor dynamics field has produced many models, often non-linear or with particular attention to chaotic behaviour, but with scarce correspondence with real rotors since Jeffcott-like rotors are mainly used without thermal transients, or sometimes real rotors are used but with very simple thermal modelling. One of the most remarkable aspects of the rotor-to–stator rub at operating speed is the possibility of observing *spiral vibration* phenomena in the synchronous vibration, i.e. the vibration vector changes its amplitude and rotates even at the rated speed. This is due to the combined effect of the contact forces which introduce heat and of the resulting thermal bow. The phenomenon is also called *vector turning* or *thermally induced vibrations*. It is interesting to analyze the dynamical behaviour of the machine: the spirals can have a self-propagating trend or conversely a self-correcting trend.

The model presented in the paper for the analysis of the spiral vibration has a unique characteristic in that it allows real machines to be analyzed, since it uses a fully assembled machine model (rotor, bearings and foundation) and implements a rather sophisticated thermal and contact model.

The experimental validation of the proposed model is performed on data coming from a real machine: the generator of a 50 MW combined cycle power plant, in which unstable spiral vibrations were observed at the operating speed during a power increase.

1. INTRODUCTION

The rubbing phenomenon that occurs in rotating machinery has been studied more intensively in recent years, since higher efficiency requirements often lead to the reduction of clearances in seals in newly designed machines. This fact, sometimes combined with thermal induced misalignment, makes the event of rubbing more frequent, as it is reported by machine manufacturers and by final users.

Rotor-to-stator rubs involve many different aspects, since the contact between the stator and rotor can be caused by different reasons and can occur in different sections of the rotor such as bladed parts, journals of bearings, seals, etc. Therefore in the past years many studies have appeared in literature that analyse or model a particular effect.

Turbine blade contact with the casing is analyzed by Ahrens et al. [1,2] using a model-based method to predict impact contact forces. Sinha [3] presents a method to illustrate the non-linear dynamic effect of blades rubbing against the rigid outer case in a rotating machinery. The effect of rub on torsional vibration of the rotor is studied by Edwards et al. [4], by Huang [5] who presents an experimental study on the coupling of torsional and lateral vibrations and by Deng et al. [6] who uses a simplified Jeffcott rotor model to study the effect of the friction coefficient on the FFT full-spectrum of the torsional vibration. A study on axial rubbing is presented by Childs and Siddiqui [7].

Several papers take into consideration the problem of the stability of the rubbing rotor. Since the rub is a typical non-linear phenomenon, this has increased the interest of many researchers to develop theories related to stability. Childs [8] uses a Jeffcott rotor model to explain the presence of the half-frequency whirl. Curami et al. [9] use a 4 d.o.f. model to explain the rubbing behaviour of a 320 MW steam turbo-generator. Isaksson [10] investigates the *jump* phenomenon with a Jeffcott rotor model. Goldmann and Muszynska [11] present a simplified model, in which both contact

forces and thermal aspects are considered. Bently et al. [12,13] use a simplified model to study the dry friction related instability (known also as *dry whip*), which was observed on a small scale test-rig. Choy et al. [14,15] use a FFT full-spectrum to study super-harmonic, sub-harmonic and jump phenomenon in a small scale test-rig. Jiang and Ulbrich [16,17] use a Jeffcott rotor model to perform the stability analysis of the full annular rub. A similar topic is studied by Muszynska [18]. Ehehalt and Markert [19-21] study the stability thresholds by means of a Jeffcott rotor. Keogh and Cole [22] use a Jeffcott rotor model to analyse the stability of the rotor-to-stator contact of a test rig and then [23,24] use an auxiliary magnetic bearing to control the position recovery of the shaft.

However, all these papers, which are all interesting from a mathematical point of view, scarcely correspond to reality since they generally neglect, with the exception given by [11], the thermal aspect, which plays a primary role in the rotor-to-stator contact (as stressed by several authors, especially by Adams [25]), and give qualitative rather than quantitative explanations of the phenomenon involving simple systems with few degrees of freedom.

The presence of non-linearities has also encouraged many authors to investigate the chaotic aspect of the phenomenon and some papers have been published in the last ten years. Yang and al. [26,27] present bifurcation maps of a simple rotor with contact forces. Adams and Abu-Mahfouz [28] use a two d.o.f.s orbital motion model to introduce chaos related indicators such as fractal dimension or Poincaré maps and suggest their use as a diagnostic tool. Muszynska and Goldmann [29] employ a modal approach and obtain bifurcation diagrams. Wu and Chen [30] use two d.o.f.s and obtain bifurcation diagrams. Dai et al. [31] introduce a four d.o.f.s system and partial or full annular rub, obtaining limit cycles for the rotor orbits, Poincaré maps and bifurcation diagrams. Zapoměl et al. [32] analyze the impacts of a simple rotor and study the form of the orbits, Poincaré maps, bifurcation diagrams and Lyapunov exponents. Similar analysis tools, along with power spectra, are suggested also by Sawicki [33]. Feng and Zhang [34] use two d.o.f.s to study partial and full annular contacts as a function of the friction coefficient value. Hu and Wen [35] use Lyapunov

exponents to forecast chaotic response of a test-rig. Yuan et al. [36] present a numerical example of a four d.o.f.s model with Poincaré maps, power spectrum, phase maps, bifurcation diagrams and Lyapunov exponents. Similar concepts are proposed in a diagnostic tool by Lucifredi et al. [37]. Zhang et al. [38,39] use a statistical approach to study a 2 d.o.f.s rubbing system. Qin et al. [40] use a transfer matrix representation for the rotor and Poincaré maps.

While respecting the mathematical soundness of these models, they reproduce at most the behaviour of small scale test-rigs (like those of [29,37]), but scarcely the behaviour of real machines, especially those of a large size. These are normally equipped with oil-film bearings with high damping, they have rotors with great mass and inertia and the rotors are much stiffer than the seals so that their dynamical behaviour is not characterized by rotor bouncing on the stator and the impacts are generally non-elastic. Moreover, in real machines, thermal aspects, which are disregarded by models dealing with chaos, are definitely not negligible during rubbing. Experimental evidence and models related to the alteration of rotor system dynamical properties due to thermal effects, asymmetrical heating and rotor bow are presented in literature. Ehrich [41] indicates the thermal effect due to rubs as a cause of self-excitation in rotor dynamics. Kennedy [42] observes that rubs induce a heavy thermal gradient. Hashemi [43] presents experimental results about the effect of load changes and the consequent rotor bow in the high pressure turbine of a 500 MW steam turbo generator. Larsson [44,45] puts in evidence the effect of heating due to the temperature distribution in the journal and then extends his analysis [46,47] using a simplified thermal approach to the bow induced by rubbing in a seal. Adams [25] describes the *vibration vector turning* in the exciter of a 760 MW steam turbo generator. Takahashi et al. [48] present a study about asymmetric heating of a journal due to magnetic bearings and present an active control to reduce thermally induced vibrations. Other authors have dealt with the behaviour of rotors presenting rub during speed transients. Yanabe [49] uses a Jeffcott rotor to study the passage through critical speed of a power limited rotor. With regard to actual machine behaviour, Vania et

al. [50] analyse a light rub in the high-intermediate turbine of a 320 MW steam turbo-generator during a coast-down and use a model based identification technique to locate the rubbing position. Bachschmid et al. [51] use the same technique to identify the rub in the low pressure turbine of 320 MW steam turbo-generator.

Finally, rotor-to-stator rub, for instance in seals, at constant (operating) speed can cause so-called *spiral* or *thermally induced* vibration to occur. The amplitude and the phase of the one per revolution (in the following 1X) vibration changes at constant speed, so that some other authors prefer to define this phenomenon as *vector turning from synchronously modulated rub*. Experimental evidences on the synchronous vibration are shown by Kellenberger [52] on a 722 MVA turbo generator operating at 3600 rpm, by Schmied [53] on a 600 MVA turbo generator, by Stegemann et al. [54] on a 100 MW 3-stage condensation turbine with re-heater during different output power operating, by Muzynska [55] on a turbine rotor (the same diagram is also reported in [33]), and by Liebich and Gasch [56] who present the results measured by Drechsler on a combined cycle plant operating at 3000 rpm. In [52] some criteria are also presented to establish the relationships between stability and the critical speeds vs. operating speed.

This kind of dynamical behaviour, which is also called *Newkirk effect* from the author of the first literature paper in 1926 [57] (even if the phenomenon was already described in a GE report of 1924 by Taylor [58]), is indeed most relevant in real machines and has been studied by many authors that have presented different simplified models in order to simulate the dynamic behaviour that can be related both to heavy and light rubs. With very few exceptions (those of Schmeid [53], Liebich and Gasch [56] and Liebich [59] use simplified thermal models), these papers use a simple Jeffcott rotor to model the rotating machine while a rigid stator is often considered, so that its motion can be neglected and a restricted number of degrees of freedom are taken into account (see the models proposed by Kellenberger [52], Gruber [60], Larsson [46,47] and Sawicki et al. [61]). This kind of simplification does not allow one to model in detail the thermal phenomena that are

related to rotor-to-stator contacts although they can significantly affect the machine dynamic behaviour and rub development. The consequence of the shaft heating is not negligible as the tangential force due to the friction may cause a significant thermal bow of the shaft and spiral vibrations can be engaged. Moreover, the anisotropy of oil-film bearings causes not circular orbiting of the shaft, and the condition in which the rotor comes into contact with the stator should be carefully analyzed. An accurate model for a real rotor-bearing-foundation system has to take into consideration the contact forces, the shaft thermal bow induced by the heat introduced by the friction and the stability analysis of the dynamical behaviour. Finally the model should be validated by means of experimental results.

In the recent past, the authors [62-64] proposed a rather sophisticated model in which the rotor dynamics behaviour was studied by means of 1D finite beams and a 3D model was used to calculate the temperature distribution and the associated thermal bow. The well-known Fourier's equations with suitable boundary conditions were solved numerically by means of a finite difference approach. The bow, determined by the thermal conditions and calculated by means of the 3D model, was then reproduced by means of a set of suitable bending moments (this method was also used in [11,46,47] and validated in [62]), which were applied to the nodes of the beam element model of the rotor.

In this paper the model is improved in order to take into consideration 1X filtered elliptical orbits of the shaft. This aspect is more accurate for large rotating machines, which are usually supported by oil-film journal bearings. In this case, the definition of the rotor arc that comes in contact with the stator is not trivial and the complete discussion is presented here. The stability thresholds of the rotor motion are analyzed with regard to the rotating speed vs. critical speed for two different machines, showing that if the dynamical response of the machine is characterized by several critical speeds, both of rotor and foundation, instability with spiralling, stability and limit cycles are possible. Finally the model is employed here to simulate a rotor-to-stator rub in a bakelite

casing of a generator of a 50 MW plant. The simulated results are then compared with the experimental ones obtained during an actual rub of the machine.

2. MODEL DESCRIPTION

Often, owing to the flexibility of the seal mountings and to the causes of the rub phenomena, the rotor to stator contacts are not severe impacts, but large partial arc rubs or full annular rubs. In these cases, the contact forces gradually rise and decrease during the rub. In accordance to this, many partial arc rubs in real machines show only a single contact per revolution. When the rubs show this characteristic, the machine dynamic behaviour is rarely affected by chaotic motion. Conversely, the synchronous (1X) component often gives the most important contribution to the harmonic content of the shaft vibrations, as shown in the experimental results of [52,56]. When these conditions are satisfied, 1X spiral vibrations induced by the thermal effects due to the friction forces can occur.

The presence of higher order harmonic components can be caused by non-linear effects in the oil-film of the journal bearings as well as time varying radial stiffness during rubs. Although these effects can occur, they give less contribution to the machine dynamical behaviour than that of the thermal bow. Experimental results shown in [50,56] for rated and transient speed support this statement, since the super-synchronous components have limited amplitude with respect to 1X components.

In general the changes in the 1X vibration vector take place in a rather long time and rub phenomena that occur during subsequent complete revolutions of the shaft are rather similar, therefore the dynamic behaviour of a real rotating machine can be evaluated in the frequency domain by means of a model based method. In this investigation, rotor-to-stator rubs that cause impacts have not been considered. On the contrary, full annular rubs or large partial arc rubs have been studied. Therefore, the model of the fully assembled machine has been used to evaluate only

the synchronous vibrations. The motion equations of the system could be integrated in the time domain along with the thermal equations, but, owing to the absence of impacts, the dynamic behaviour of the rotating machine can be studied in the frequency domain. Furthermore it is important to consider that also the evolution of the thermal effects occurs in longer times than the period of revolution of the shaft. Finally, with regard to the evolution of the thermal effects, the equations are integrated in the time domain.

In accordance to previous assumptions, Figure 1 shows the flowchart of the *domain swap* method proposed here. Starting from the consideration of a rotating machine, its fully assembled model is taken into account and the 1X dynamical behaviour in frequency domain is calculated at the operating speed on the basis of the initial exciting conditions. In this phase a standard 1D finite beam element model [25,65], with gyroscopic, shear and secondary inertia effects, is used for the rotor.

The rub conditions are then analyzed. If the rotor interferes with the stator, for instance in a seal, the first step of the simulation starts: the interaction causes contact forces on the rotor and, due to the friction, heat is introduced in a small part of the rotor surface (see also [47]). This determines temperature gradients in radial and axial directions in the cylindrical rotor part which is close to the rubbing section. In order to calculate the strain distribution, this rotor part is modelled by means of a 3D mesh and the Fourier's equations are applied and integrated in the time domain. The integration time step should longer than the period of revolution of the shaft. The thermal strain distribution can cause a thermal bow of the rotor, that can be reproduced by means of equivalent bending moments as shown in [11,46,47,62-64] on the 1D finite beam model.

This way the equivalent exciting system acting on the rotor is given by the initial exciting conditions (the original unbalance and bow of the rotor), by the contact forces determined in the present simulation step and by the equivalent bending moments that reproduce the thermal bow of the rotor in the present step. Then the 1X response is again calculated in the frequency domain, the

rub conditions are analyzed and the next simulation step starts. In all the following steps, if the rotor does not come in contact with the stator, contact forces are equal to zero, no heat is introduced, but Fourier's equations are solved anyway to define the new temperature and strain distribution and finally the new values of the equivalent bending moments.

The procedure is valid as long as the thermal transient time constant is much higher than the vibrational transient time constant, as is also observed in [11]. This condition is usually satisfied in large rotating machines that have considerable thermal inertia.

2.1. Determination of the rub conditions in real rotors

Let's consider a rotating machine, supported by oil-film bearings, that presents rotor-to–stator rub in a general section, which could be a seal for convenience. In general, the 1X rotor orbit in the seal, that can be considered circular, is elliptical and not centred in the centre of the seal (due to bearing and seal alignment errors and uncertainties in the journal offset inside the bearing).

Three reference systems will be considered (Figure 2). The first, $S(x,O,y)$, is rigidly connected to the seal and its origin O is in the centre of the seal. The second, $S'(x',O',y')$, has the axes parallel to those of S and is centred in the centre O' of the orbit; $(O'–O)$ is the misalignment between the seal and the rotor in the rubbing section. The last, $S''(x'',O'',y'')$, has its centre O'' coincident with that of S' and is rotated by the angle ψ so that axis x'' coincide with the major axis of the elliptic orbit (Figure 3).

Angle α is the angular position of phase reference KP (key-phasor dot) in the reference S' and γ is the angle of KP in the reference S''.

Figure 4 shows the geometry of the interaction between the rotor and the seal that causes a relative deflection. Owing to the higher stiffness of the shaft than that of the seal mountings, in the paper the deflection is assumed to be a contribution of the seal only. The seal is simply modelled as

a linear spring of suitable stiffness. The rotor and seal interaction can be conveniently analyzed by means of comparison of the rotor orbit (centred on O′) and clearance in the seal, that is represented by a circumference centred in O. Obviously the interaction between the rotor and the stator does not occur in only a point called *hot-spot* HS, as in the simplified models [53,56,59], but on arcs in the section corresponding to the seal. The HS concept can be extended anyway, as shown in the following, in order to consider it as the point of the rotor where the resultant contact forces acting on the arc can be applied. The meaning of the STR point is explained in the following. Three different rubbing conditions can arise, but in any case both the amount of the real deflection of the seal and the HS position change during rotation.

In the first condition, shown in Figure 5 with regard to the rotor orbit and the clearance and in Figure 6 with regard to deflection and its phase with respect to the KP as a function of the rotor rotation angle, is a *partial annular* rub with one interference zone only. In Figure 6, the phase is defined only when the deflection of the seal is greater than zero.

The second rubbing condition, shown in Figure 7 and Figure 8, is instead a *partial annular* rub with two interference zones. In this case also, the phase is defined only when the deflection is greater than zero.

The third rubbing condition is the *full annular rub*, shown in Figure 9 and Figure 10.

From the analysis of Figure 5 to Figure 10 it is evident that, due to the ellipticity of the orbit and the misalignment between the rotor and the seal centre, in any possible rubbing condition the deflection (once given the rotor and seal stiffnesses) is a function of the rotor rotation angle. Since the 1X dynamical behaviour is considered, it is necessary to calculate, on the basis of the deflection, the 1X component of the contact forces on the rotor and to define the thermal power generated by the friction. The equations of the rotor orbit in reference system *S* are:

$$\begin{cases} x(t) = x_{O'} + X\,\mathrm{Re}\left(e^{i(\Omega t+\varphi_X)}\right) \\ y(t) = y_{O'} + Y\,\mathrm{Re}\left(e^{i(\Omega t+\varphi_Y)}\right) \end{cases} \tag{1}$$

where X , Y are the amplitudes of the 1X vibration in horizontal and vertical directions, while φ_X and φ_Y are the respective phases.

If R is the clearance between the rotor and the seal, the deflection $\delta(t)$ results:

$$\delta(t) = \begin{cases} \sqrt{x^2(t)+y^2(t)} - R & \sqrt{x^2(t)+y^2(t)} > R \\ 0 & \sqrt{x^2(t)+y^2(t)} \le R \end{cases} \tag{2}$$

The average deflection is then calculated over the rotation period T_r:

$$\overline{\delta} = \frac{1}{T_r}\int_0^{T_r} \delta(t)\,dt \tag{3}$$

Now we must state the criteria that defines the HS in which the contact forces are applied. By the consideration of the deflection diagrams in Figure 6, Figure 8 and Figure 10 it follows that a particular point of the rotor can rub once (as for instance the point at phase reference of 60° in Figure 6), twice (point at 45° in Figure 10) or never in a revolution (point at 30° in Figure 6, at 70° in Figure 8 and at 60° in Figure 10). It seems reasonable to apply the contact force at the rotor point, indicated in the diagrams as STR, where the contact occurs at the maximum rotor deflection. In order to locate point STR and the HS on the rotor, it is necessary to consider some angles shown in Figure 11.

Angle ξ is the phase reference of STR in S' reference system. Angle β is the angle between KP and STR and has the same direction as the orbit precession and is equal to:

$$\beta = \begin{cases} \xi - \alpha & \xi \ge \alpha \\ 2\pi - (\alpha - \xi) & \xi < \alpha \end{cases} \tag{4}$$

Since the phase reference in the rotor reference system is considered vertical with counter clockwise positive θ rotation, as shown in Figure 12, when the centre of the rotor is the STR point

of its orbit, the rotor has its phase reference which has rotated by angle β from the vertical direction in the rotating speed direction Figure 13. Then the HS is defined as the point of the rotor external surface that is laying on the line, whose slope is angle τ, passing through STR and the centre of *S* reference system. The HS phase in the rotor reference system is therefore:

$$\sigma = \tau - \left(\beta + \frac{\pi}{2} \right) \tag{5}$$

2.2. Contact forces

Once the phase σ of the HS is calculated, the contact forces applied to the rotor are fully known (Figure 14). If k_s is the stator stiffness, elastic deformation is considered and μ the friction coefficient, the normal contact force $\mathbf{F}_n$ and the tangential friction force $\mathbf{F}_t$ are equal to:

$$\begin{aligned} \mathbf{F}_n &= -k_s \, \overline{\delta} \, e^{i\sigma} \\ \mathbf{F}_t &= \mu \, k_s \, \overline{\delta} \, e^{i\left(\sigma - \pi/2\right)} \end{aligned} \tag{6}$$

Note that moment of the tangential force with respect to the rotor centre is not zero and it therefore torsionally excites the rotor. This aspect is neglected in the present model however since it is devoted to the analysis of lateral vibrations only, which are involved in the spiral vibration effect.

Once the friction force is calculated, the thermal power that is used as the input in the 3D thermal model is given by:

$$\dot{Q} = \mu \, k_s \, \overline{\delta} \, \Omega \frac{D}{2} \tag{7}$$

where Ω is the machine angular speed and *D* is the shaft diameter at the cross section where the rub occurs.

2.3. Temperature distribution

As previously mentioned, only a part of the rotor close to the seal has been considered for the calculation of the temperature distribution.

This fact is due to the necessity to limit the number of nodes in the 3D mesh (Figure 15), but can be accepted by considering that the thermal effects at a distance of a diameter from the seal are reduced greatly.

The evolution of the temperature distribution clearly depends on the heat exchange modes between the rotor and the surroundings as well as within the rotor itself. A widely accepted idealisation is as follows:

- the seal-rotor contact gives rise to power generation that is modelled as a localised heat source for the rotor; obviously if the rotor does not rub in the considered time step, no heat is introduced;
- pure heat conduction takes place in the interior of the rotor;
- convection takes place all over the skin of the rotor to account for interactions with the external environment.

By writing the Laplacian operator in cylindrical co-ordinates, one gets the well-known Fourier's equation in the form:

$$\frac{\partial T}{\partial t} = \frac{K}{\rho C}\left(\frac{\partial^2 T}{\partial r^2} + \frac{\partial T}{r\,\partial r} + \frac{\partial^2 T}{r^2\,\partial \vartheta^2} + \frac{\partial^2 T}{\partial z^2}\right) \tag{8}$$

where K is the thermal conductivity coefficient [W/m K], ρ is the mass per unit volume [kg/m^3], t the time [s], z the axial co-ordinate [m], r the radial co-ordinate [m], ϑ the angular co-ordinate [rad], C is the specific heat [J/kg K] and T [K] is the temperature. Eq. (8) is a parabolic PDE in the unknown temperature distribution $T = T(r, \vartheta, z, t)$. An initial uniform temperature distribution T_0 as well as boundary conditions as specified below (see Figure 16) are coupled to Fourier's equation for

evaluating the temperature distribution on the external surface. Except for the HS, thermal balance requires that the thermal power that flows into the rotor through its external surface and that diffuses by conduction inside the rotor is equal to the thermal power exchanged by convection between the rotor and the surrounding fluid. Therefore the heat transfer rate due to each element of surface *dS* by conduction is:

$$\dot{Q} = -K \nabla T \, dS = -K \left(\frac{\partial T}{\partial r} + \frac{\partial T}{r \, \partial \theta} + \frac{\partial T}{\partial z} \right) dS \tag{9}$$

The heat transfer rate due to convection on the infinitesimal section *dS* of the external surface is:

$$\dot{Q} = H \left(T - T_f \right) dS \tag{10}$$

where H is the thermal convective coefficient [W/m^2 K] and T_f the temperature of the surrounding fluid [K]. Considering eqs. (9) and (10) the temperature on the external surface of the rotor is given by:

$$-K \left(\frac{\partial T}{\partial r} + \frac{\partial T}{r \, \partial \theta} + \frac{\partial T}{\partial z} \right) = H \left(T - T_f \right) \tag{11}$$

In the element having the HS on its surface, the boundary condition has to consider the thermal power introduced by the rubbing so Fourier's equation (8) becomes:

$$\frac{\partial T}{\partial t} = \frac{K}{\rho C} \left(\frac{\partial^2 T}{\partial r^2} + \frac{\partial T}{r \, \partial r} + \frac{\partial^2 T}{r^2 \, \partial \vartheta^2} + \frac{\partial^2 T}{\partial z^2} \right) + \frac{\hat{Q}}{\rho C} \tag{12}$$

where $\hat{Q}$ is the specific thermal power [W/m^3].

The numerical solution of the Fourier's PDE may be classically approached via well-consolidated finite-element schemes. For the purpose of this investigation, however, a finite-difference approach has been adopted, mainly to get an easier link to the other blocks of the simulating code. One should in fact recall that, for any given time instant, the Fourier equation is solved, and the temperature gradients are used to derive the corresponding strains and eventually

equivalent moments are computed. They represent the input of a frequency-domain analysis providing amplitude and phase of the response, i.e. the rotor deflection.

Without entering into detail, it is appropriate to show the discrete version of the Fourier's equation that, after finite-differentiation and some algebra, reads:

$$T_n(r,\vartheta,z) = T_o(r,\vartheta,z) + D\,dt\left[\frac{T_o(r+1,\vartheta,z) - 2\cdot T_o(r,\vartheta,z) + T_o(r-1,\vartheta,z)}{dr^2} + \right.$$
$$+\frac{T_o(r+1,\vartheta,z) - T_o(r-1,\vartheta,z)}{r\,dr} + \frac{T_o(r,\vartheta+1,z) - 2\cdot T_o(r,\vartheta,z) + T_o(r,\vartheta-1,z)}{r^2\,d\vartheta^2} + \tag{13}$$
$$\left.+\frac{T_o(r,\vartheta,z+1) - 2\cdot T_o(r,\vartheta,z) + T_o(r,\vartheta,z-1)}{dz^2}\right] + \frac{dt\,\dot{Q}}{\rho\,C\,dr\,d\vartheta\,dz}$$

where $D=K/\rho C$ is the thermal diffusivity coefficient, dt is the time step and T_n and T_o denote the new (unknown) and old (converged) values of the temperature respectively. The last term in eq. (13) exists only if the rotor rubs on the seal and the element of the 3D mesh is the HS. Furthermore, notations such as $r+1$ and similar notations denote the value of the relevant quantity (temperature) at an adjacent node. The discrete Fourier's equation is written for all internal points of the rotor part with the 3D mesh (Figure 15) and coupled to the discrete boundary conditions giving rise to a linear system of equations having the current temperatures as unknowns. At the end sections of the meshed cylinder, an axial temperature gradient $\partial T/\partial z$ is assumed equal to that of the closest elements. This slightly overestimates the heat flow through the end sections, but is a much better estimate than zero heat flow. Some examples of the temperature distribution on the surface are shown in the following, see Figure 23. Note that the migration of the element of highest temperature on the rotor surface is evident in this figure, recalling that that element does not necessarily correspond to the HS as it was defined in the paper. The discussion about the convergence of the numerical solution is reported in Appendix 1.

2.4. Thermal strains and stresses

Once the temperature distribution is evaluated, thanks to the isotropy of the rotor, standard thermo-mechanical relations are used to get the thermal strains along the main directions as:

$$\begin{aligned} &\varepsilon_r = \varepsilon_\vartheta = \varepsilon_z = \hat{\alpha}\,(T - T_0) \\ &\gamma_{xy} = \gamma_{yx} = \gamma_{zx} = 0 \end{aligned} \tag{14}$$

where $\hat{\alpha}$ is a material-dependent thermal expansion coefficient. The components of the strain tensor are then used to compute the stresses in the rotor by using standard isotropic elasticity relations as:

$$\begin{Bmatrix} \sigma_x \\ \sigma_y \\ \sigma_z \\ \tau_{xy} \\ \tau_{yz} \\ \tau_{zx} \end{Bmatrix} = \frac{E}{(1+\nu)(1-2\nu)} \begin{bmatrix} 1-\nu & \nu & \nu & 0 & 0 & 0 \\ & 1-\nu & \nu & 0 & 0 & 0 \\ & & 1-\nu & 0 & 0 & 0 \\ & & & \frac{1-2\nu}{2} & 0 & 0 \\ & \textit{symm.} & & & \frac{1-2\nu}{2} & 0 \\ & & & & & \frac{1-2\nu}{2} \end{bmatrix} \begin{Bmatrix} \varepsilon_x \\ \varepsilon_y \\ \varepsilon_z \\ \gamma_{xy} \\ \gamma_{yz} \\ \gamma_{zx} \end{Bmatrix} \tag{15}$$

These are the stresses which would arise if appropriate constraints would prevent any elongation and the rotor can be considered within the limits of the Euler's beam theory. The axial stress distribution, equal to:

$$\sigma_z = \frac{E}{(1+\nu)(1-2\nu)} \left(\nu\,\varepsilon_x + \nu\,\varepsilon_y + (1-\nu)\,\varepsilon_z \right) = \frac{E}{(1-2\nu)}\,\varepsilon_z \tag{16}$$

allows calculation of an equivalent bending moment [11,46,47,62-64], which should generate similar strains and a similar overall deformation, as shown below.

The local radial deformation u_r due to rotor-to–stator rub is calculated starting with its finite difference derivative definition:

$$\frac{\partial u_r}{\partial r} = \frac{u_r(r,\vartheta,z,t) - (r-1,\vartheta,z,t)}{dr} \quad \rightarrow \quad u_r(r,\vartheta,z,t) = (r-1,\vartheta,z,t) + \varepsilon_r\,dr \tag{17}$$

The local radial deformation u_r is much less than the overall thermal bow and could be neglected. It contributes however to the seal deflection and in this paper is considered in the calculation of eq. (2).

2.5. Equivalent bending moments due to the thermal bow

The first step for determining the modulus M of the equivalent moment is to take into account the strains ε given by eq. (14). A typical ε_z axial strain distribution in the HS section is shown in Figure 17, in which also the generated bow and the local radial deformation u_r are emphasized. The axial strain distribution over the cross section is not linear and the cross sections subject to the temperature gradient due to the concentrated heating at the HS, are very much distorted.

This strain distribution, due to the thermal action, has to be modelled by mechanical loads, which should reproduce at least the resulting bow.

For the evaluation of the bow, the components M_x and M_y of the equivalent bending moment M are calculated separately, in the fixed reference frame $S(x,O,y)$, by considering the actual stress distribution over all the shaft sections:

$$M_x(z) = \int_A \sigma_z \, b_x \, dA = \int_0^R \int_0^{2\pi} \sigma_z \left(r, \vartheta\right) r^2 \sin\vartheta \, dr \, d\vartheta$$

$$M_y(z) = \int_A \sigma_z \, b_y \, dA = \int_0^R \int_0^{2\pi} \sigma_z \left(r, \vartheta\right) r^2 \cos\vartheta \, dr \, d\vartheta \qquad (18)$$

These bending moment components are applied to node z and the same components, with the opposite sign, are applied to next node $z + 1$ of the 1D finite beam element model of the rotor. Figure 18 shows an example of the bending moments, in the horizontal direction, calculated for all the nodes of the 1D finite beam model affected by the thermal distribution during a simulation.

The bending moment generates a linear stress and strain distribution (shown in Figure 17) over the cross section, which is not at all distorted. Since an approximation has been made here, the validation of this method with the results obtained with a 3D f.e. model, analysed with a commercial f.e. code, has been performed and described in [62].

3. VIBRATIONAL BEHAVIOUR

The equivalent bending moments are used not only for simulating the static bow, but also for being superposed to the unbalance and other exciting forces, in order to simulate the dynamic behaviour of the rotor. Note that the equivalent bending moments on a rotating shaft generate a vibration, which is the superposition of the static rotating bow and the actual vibration.

Now all the forces and moments are applied to the finite beam element model of the fully assembled machine. Details on the model assembling can be found in [65]. If the rotor does not rub against the seal, its vibrational behaviour is due to its natural unbalance $\mathbf{F}_{unb}$ (and permanent bow $\mathbf{M}_b$ if it is the case). When rotor-to-stator rub occurs, the vibration vector shows a phase lag with respect to the rotor unbalance. the exciting system that modifies the vibrational behaviour of the rotor is composed of the contact force of components $\mathbf{F}_n$ and $\mathbf{F}_t$ of eq. (6) applied to the rotor section corresponding to the seal and by several moments $\mathbf{M}_x$ and $\mathbf{M}_y$ simulating the thermal bow, whose components are given by eqs.(18). The bending moments are distributed over the m nodes, in the axial direction around the HS, where the temperature distribution is calculated and their values are updated at each time step. Therefore the dynamic equation of the rotor system in the fixed reference frame $S(x,O,y)$ is:

$$[\mathbf{M}]\ddot{\mathbf{x}} + [\mathbf{D}(\Omega)]\dot{\mathbf{x}} + [\mathbf{K}(\Omega)]\mathbf{x} = \left(\mathbf{F}_{unb} + \mathbf{M}_b + \sum_1^m \mathbf{M}_x + \sum_1^m \mathbf{M}_y + \mathbf{F}_n + \mathbf{F}_t\right) e^{i\Omega t} \tag{19}$$

where all the forces are complex quantities, [**M**] is the mass matrix, [**D**(Ω)] is the damping matrix that includes internal damping and the gyroscopic effect and [**K**(Ω)] is the stiffness matrix. The global stiffness matrix [**K**(Ω)] in eq. (19) is the sum of different stiffness matrices associated with the shaft, journal bearing and foundation. Only the part related to the shaft stiffness is used to build up the internal damping matrix. Moreover, only the part related to the journal bearings is speed depending, but this justifies the addiction of the dependence on Ω.

The heat introduced by the rub creates a temperature difference between the diametrically opposite elements and the rotor starts bowing in an axial plane corresponding to the initial phase of the vibration vector. The bending moments, which model the bow, are vectors rotated by −90° with respect to that plane.

At each time step the new value of all the displacements of the nodes of the rotor model is determined by solving eq. (20) in the frequency domain.

$$\mathbf{X} = \left(-\Omega^2[\mathbf{M}] + i\,\Omega[\mathbf{D}(\Omega)] + [\mathbf{K}]\right)^{-1}\left(\mathbf{F}_{unb} + \mathbf{M}_b + \sum_1^m \mathbf{M}_x + \sum_1^m \mathbf{M}_y + \mathbf{F}_n + \mathbf{F}_t\right) \tag{20}$$

The vibration vector of the node corresponding to the seal $\mathbf{X}_s$ will be found rotated by a small angle due to the effect of the new exciting causes $\Sigma\mathbf{M}_x$, $\Sigma\mathbf{M}_y$, $\mathbf{F}_n$ and $\mathbf{F}_t$.

The components of $\mathbf{X}_s$ are then used to consider the 1X orbit and the rub occurrence is checked. If the rubbing conditions previously described are applicable, the energy introduced by the rub is calculated, along with the new temperature distribution of the rotor and the resulting bow moment $\Sigma\mathbf{M}_x$, $\Sigma\mathbf{M}_y$. This is introduced in eq. (19) along with the contact forces $\mathbf{F}_n$ and $\mathbf{F}_t$ and the simulation loops. If 1X orbit does not interfere with the clearance *R*, then the new temperature distribution and the equivalent $\Sigma\mathbf{M}_x$ and $\Sigma\mathbf{M}_y$ are determined and eq. (19) is now solved without considering the contact forces and the procedure loops.

Before presenting the results of the simulations and the experimental case, it is worthy to premise a short discussion about spiral vibrations and stability. The dynamical behaviour of a rotating system is generally stable if the vibration vector has a limited evolution in time [66].

Since spiral vibration phenomenon is characterized by the fact the vibration vector changes its amplitude and rotates even at the rated speed, is therefore a kind of instability.

However, the authors who have analysed the phenomenon use to define the spiral vibration as stable when it has a self-correcting trend and converges, even asymptotically, to a new value. Conversely, the spiral vibration is deemed as unstable when the amplitude has a divergent trend. This way, the stability concept is no longer associated with the mathematical concept of limited evolution, rather to the empirical one of a vibration whose amplitude does not diverge. In order to avoid misunderstandings in the following, the terms *spiral stability* and *spiral instability* will be used. The former indicates the convergence of the amplitude and phase to a new value, the latter indicates the divergence. Limit cycles will be also obtained in the following simulations, but no further definitions are necessary in this case.

4. SIMULATION OF THE DYNAMICAL BEHAVIOUR OF A STEAM TURBINE

The proposed method has been applied to a model of a HP-IP industrial steam turbine, shown in Figure 19, supported by anisotropic oil-film bearings modelled by means of speed dependent damping and stiffness coefficients. The rub occurs close to the middle of the rotor between the HP and the IP sections, where some seals are located in the real machine. Note in the figure that the mesh has been thickened in the seal zone to apply the thermal model. Details about the model are reported in Appendix 2.

Since only differential temperatures influence the behaviour, an (unrealistic) initial temperature of 25°C has been taken into account for both of the simulations presented. Also the heat exchange

coefficient is that of the air for both the simulations, which is correct for the second case only. The influence of this parameter on the behaviour is however rather small.

The frequency response of the rotor due to an unbalance in the seal is shown in Figure 20 up to 7000 rpm. Due to the anisotropy (see the orbit in the bearings at 1900 rpm in Figure 20), vertical and horizontal critical speeds are close, but not equal: the first is at about 2000 rpm, the second at about 5000 rpm.

At operating speeds below the first critical speed, the machine presents spiral instability. From Figure 21, that represents the polar plot of the vibration vector in the seal in the vertical direction, it is possible to note that the evolution of the spiral is getting slower when the speed increases. In fact, the limit imposed to stop the simulation (vibration amplitude of 5000 μm, which is intentionally exaggerated) is reached in more time steps and the spiral aspect becomes more evident (see the 1800 rpm curve, in which a spiral period is completed). Similar results are obtained for the horizontal direction.

At an operating speed of 1900 rpm, just below the first critical speed, the spiral vibration, shown in Figure 22, is quite evident and it takes 1000 s to reach an amplitude of 300 μm, even if the system presents spiral instability.

Note in Figure 22 that the spiral vibration has an “elliptical” aspect. This fact can be explained by means of analysis of the temperature distribution on the rotor surface in the seal section, as a function of the time steps. Figure 23 shows that the temperature has an increasing trend, but not monotonic, and that the element of highest temperature (not necessarily corresponding to the HS) migrates along the external surface.

When the operating speed is greater than the first critical speed, the vibration vector amplitude has a decreasing trend and the behaviour can be considered as spiral stability even if the spiral trend is not evident. An apparent steady-state situation is obtained in which a very light rub introduces sufficient heat to reduce the contact force. Moreover, system evolution appears to get slower when

the operating speed increases, since all the simulations of Figure 24 last the same amount of time (1000 s).

A slight change occurs at 3600 rpm, when the evolution of the vibration vector begins to become circumferential. At operating speeds greater than 4200 rpm the behaviour is that of spiral instability (Figure 25) and gets faster with the increasing of the speed. It is difficult to establish the threshold between spiral stability and instability. By referring to the frequency response of the rotor shown in Figure 20, it occurs when the amplitude is still decreasing and the phase, even if rather flat, is starting to increase.

As already observed for operating speeds close to the first critical speed, the evolution of the spiral vibration becomes slower approaching the second critical speed (Figure 26). At about 5000 rpm (Figure 27) the spiral vibration does not end in a period of 1000 s and at higher operating speeds the behaviour is that of spiral stability up to 6000 rpm (Figure 28).

Quite suddenly, for operating speeds greater than 6000 rpm, the behaviour again becomes that of spiral instability (Figure 29). Also in this case, if we try to correlate the stability threshold to the rotor frequency response (see Figure 20), we can observe that the amplitude is still decreasing, but the phase starts to increase.

All the results shown here are related to the chosen position of the rubbing seal. A rubbing seal in a different position can cause considerable differences in the behaviour, which are generally due to the modal participation. With regard to the effect of the original unbalance of the rotor, a general effect is that if it increases then the spiral evolution becomes faster.

5. SIMULATION OF THE DYNAMICAL BEHAVIOUR OF A GENERATOR

The second case presented in the paper uses the model of the generator of a 50 MW combined cycle power plant shown in figure 30. In the last section of the paper, the experimental case relative

to a rotor-to-stator rub of this particular machine will be presented. The model has been tuned by using several speed transients (coast-downs) of the machine in normal conditions. One example of these speed transients is shown in Figure 31. The simulated frequency responses to a couple of unbalances of 0.06 kgm in the planes corresponding to the dots in figure 30 are shown in Figure 32 to Figure 34 for bearings #1, 2 and 3. The first two critical speeds are reproduced by the model.

The rubbing section considered in the simulation on the exciter, is the same as that of the experimental case and is close to bearing #3. Simulation parameters are reported in Appendix 3.

Moreover, even if the actual generator has an operating speed of 3000 rpm, in order to show the possible different dynamical behaviour of a rotating machine as a consequence of rotor-to-stator rub, it is useful to also present the simulations at a higher rotating speed.

Below the operating speed, the machine presents spiral instability, which has a rather fast increasing of the amplitude (also in this case the limit is 5000 μm in the rubbing section, which is intentionally exaggerated), so that the vibration path in a polar plane is practically straight (Figure 35). At the operating speed and up 3400 rpm the spiral vibration is quite evident (Figure 36) and the evolution of the spiral is getting slower.

A sudden change in the dynamical behaviour occurs at 3500 rpm even if this rotating speed does not correspond to a critical speed of the frequency response (Figure 32 to Figure 34). The vibration vector presents a limit cycle (Figure 37 for horizontal and vertical directions) and during the simulation the rotor rubs against the stator for a certain period, warms up, changes its bow, looses contact with the stator, straightens itself, comes again in contact, and the sequence continues in the same way. This behaviour is more evident if the diagrams of the temperature distribution on the rotor surface corresponding with the rubbing section (Figure 38), of the equivalent bending moments (Figure 39 in vertical direction) and of the thermal power (Figure 40) as function of the time are considered. A similar behaviour occurs at 3600 rpm as well.

At 3700 rpm the vibration vector shows spiral stability (Figure 41) and at a higher rotating speed the behaviour is stable up to 4600 rpm. At even higher rotating speeds spiral instability is present again.

The dynamical behaviour of this specific machine due to rotor-to-stator rub can hardly be related to the critical speeds of the machine. Also the frequency response is rather complex and therefore, contrary to the previous case, is quite different from the rules stated by some authors (see [52]) on Jeffcott (modal) models, in which the spiral instability has to occur under a critical speed and general stability just over, but limit cycles are not included at all. The machine behaviour appears more similar to the cases forecasted by Adams [25].

6. SPIRAL INSTABILITY IN A REAL MACHINE

The proposed rotor-to-stator rub model is used to simulate the behaviour of the generator of a 50 MW combined cycle power plant of which the model was already shown in figure 30. A section of the exciter close to bearing #3 came in contact with a bakelite casing inside of a carter (figure 42) at the constant operating speed of 3000 rpm when the power increased from 20 MW to 45 MW. The condition monitoring system of the machine has a couple of proximity probes very close to the position of the rub (figure 42). The measurements were taken along two orthogonal directions, ±45° away from the vertical direction and then converted to an horizontal-vertical reference system. Data were gathered by a permanent monitoring system during normal operation (Figure 43). In the considered case, spiral instability of the vibration was observed after operation at the increased power level and it was necessary to limit the power to 20 MW to avoid excessive vibrations. This behaviour was repetitive when the power was increased and finally the machine was stopped and maintenance operations were performed. The first occurrence of rotor-to-stator rub is analysed here, which corresponds to the interval shown in Figure 43. The evolution of the spiral is quite slow,

lasting about 2 hours and 40 minutes. It started at 14:18:58 and ended at 16:57:24 (see figure 44, where the vertical direction of 1X vibration is shown) when the alarm level was reached, the power was reduced and eventually the generator was stopped.

The causes of the rub can be ascribed to the incorrect alignment of the generator with respect to the bakelite casing. In fact, after an operating period in which the amplitude of the vibration was constant at about 20 μm, corresponding to a power increase, the vibration vector phase slowly turns and the amplitude increases up to 50 μm. Because the phenomenon starts from a small amplitude, its evolution is slow and no other malfunctions occurred, a sealing misalignment can be a probable cause. The final confirmation of this hypothesis was possible after the machine stop. The carter was disassembled and a visual inspection confirmed that the bakelite casing was damaged by the rotor contact. Moreover, during the rub, the rotor carved a path inside the bakelite stator ring, making it slightly elliptical.

The simulation of this phenomenon has been performed by means of the proposed model and the results are compared to the experimental ones in figure 44. Some attempts were necessary to estimate the original unbalance and bow of the machine. While the spiral behaviour of the vibration vector is correctly reproduced, the simulation is less effective with regard to the phenomenon duration, since the simulation lasts only 1670 s, while the experimental transient last much longer before reaching the alarm level. This fact can be explained as follows:

- In the proposed model, the stator section where the rub acts is fixed, while in the actual machine it is connected to the complete machine supporting structure. Therefore, instead of comparing rotor shaft absolute vibration to the sealing clearance, the relative displacement comparison would be more precise. The model takes into consideration the sealing stiffness k_s and this parameter can be tuned in order to include the effects of the relative motion. It is also worthy to note that in the considered machine, at the operating speed, the supporting structure motion was negligible.

- The thermal parameters, such as the thermal conductivity or the convection coefficient, the friction coefficient and the above mentioned sealing stiffness have a strong influence on the thermal behaviour and the contact forces. The values introduced in the calculation are only roughly approximated and a better estimate of them could lead to more accurate duration matching, especially with regard to the friction coefficient that, in a sensitivity analysis, is very effective on the phenomenon duration.
- At present, the model cannot take into consideration plastic deformation of the sealing (which normally occurs as observed before in this case too), the consequent clearance increasing and the possible change of the physical characteristics, especially with regard to the stator stiffness, which can be taken into account by means of a sealing stiffness $k_s(t)$ function of time. The progressive increasing of the clearance tends to slow the phenomenon and could be taken into consideration in the model by means of a clearance $R(t)$ increasing as a function of the time. In any case the two time functions are hard to be defined *a priori*.
- Finally, since the motion equations are not integrated in the time domain, the interference between the rotor elliptical orbit and the stator reproduces only a contact over an extended arc of the stator and a reduced part the shaft limited to the HS. A more accurate modelling of the geometries in contact, taking into account also the previous remarks about plastic deformation, could suggest to consider more extended surfaces for the heat transfer on the rotor due to friction.

These considerations would allow improvement of the model. However they would introduce further complication in a model that is rather complex by itself and that is already effective in giving a more than acceptable interpretation of the examined phenomenon in the present form; the possible improvement would be of second order in any case.

7. CONCLUSIONS

The model for calculating rub conditions and rotor-to-stator rub induced vibrational behaviour, commonly called “spiral vibrations” or “thermally induced vibrations” of full size rotors, has been introduced. The main characteristic of the proposed method is the “domain swap”: only the 1X is taken into account and the rotor dynamics are solved in the frequency domain. On the contrary, the rub related thermal aspects are considered in the frequency domain, but their effects on the rotor are considered by means of equivalent 1X bending moments.

Two numerical applications are presented. In the first, a relatively simple machine is considered. In this case critical speeds are clearly identifiable from the rotor frequency response. Spiral vibrations and their relationship with the rotating speed vs. critical speed are considered. The results are similar to those obtained by means of simpler modal models. On the contrary, in the second case presented, relative to a real machine, stability, spiral vibrations with self-propagating or self-correcting trends and limit cycles are present and there is not an evident relationship between rotating speed and critical speed.

Finally the capability of the proposed method to reproduce the behaviour of real machines has been validated on the experimental case of rub of a 50 MW generator.

ACKNOWLEDGEMENTS

Paolo Pennacchi wishes to gratefully thank Agnes Muszynska for the interesting discussion about this topic and for her suggestions during ISROMAC-10 Conference in Honolulu, Hawaii, March 2004.

REFERENCES

1. Ahrens, J., Jiang, J., Ulbrich, H. and Ahaus, G., 2001, “Experimentelle Untersuchungen zum Schaufelanstreifen”, *Schwingungen in Rotierenden Maschinen V”*, H. Irretier, R. Nordmann, H. Springer Editors, Vieweg Verlag, Braunschweig/Wiesbaden, Germany, pp. 95-108.
2. Ahrens, J., Söffker, D. and Ulbrich, H., 2002, “Model Based Estimations of Contact Forces of a Rotating Blade”, Proc. of *6th IFToMM Int. Conference on Rotor Dynamics*, Sydney, pp. 160-166.
3. Sinha S.K., 2004, “Dynamic characteristics of a flexible bladed-rotor with Coulomb damping due to tip-rub”, *Journal of Sound and Vibration*, Volume: 273(4-5),, pp. 875-919.
4. Edwards S., Lees A.W. and Friswell M.I., 1999, “The influence of torsion on rotor/stator contact in rotating machinery”, *Journal of Sound and Vibration*, 225(4), pp. 767-778.
5. Huang D., 2000, “Experiment on the characteristics of torsional vibration of rotor-to-stator rub in turbomachinery”, *Tribology International*, 33(1), pp. 75-79.
6. Deng X., Liebich R. and Gasch R., 2000, “Coupled bending and torsional vibrations due to rotor-to-stator contacts”, Proc. of *IMechE-7th Int. Conf. on Vibrations in Rotating Machinery*, Nottingham, pp. 291-300.
7. Childs D.W. and Siddiqui N.A., 2001, “Rotordynamics Involving axial Rubbing Against a Disk”, Proc. of *ASME Design Engineering Technical Conferences and Computer and Information in Engineering Conference*, Pittsburgh, pp. 1-5.
8. Childs D.W., 1979, “Rub-Induced Parametric Excitation in Rotors, *ASME Journal of Mechanical Design*, 101(5), pp. 640-644.
9. Curami A., Pizzigoni B. and Vania A., 1986, “On the rubbing phenomena in turbomachinery”, Proc. of *IFToMM International Conference on Rotordynamics*, Tokyo, pp. 481-486.
10. Isaksson J.L., 1994, “Dynamics of a rotor with annular rub”, Proc. of *4th IFToMM Int. Conference on Rotor Dynamics*, Chicago, pp. 85-90.

11. Goldman P. and Muszynska A., 1995, “Rotor to stator, Rub-related, Thermal/Mechanical Effects in Rotating Machinery”, *Chaos, Solitons & Fractals*, 5(9), pp. 1579-1601.
12. Bently D.E., Yu J.J. and Goldman P., 2000, “Full Annular Rub in Mechanical Seals, Part I: Experiment Results”, *ISROMAC-8 Conference*, March 2000, Honolulu, Hawaii, pp. 995-1002.
13. Bently D.E., Yu J.J. and Goldman P., 2000, “Full Annular Rub in Mechanical Seals, Part II: Analytical Study”, *ISROMAC-8 Conference*, March 2000, Honolulu, Hawaii, pp. 1003-1010.
14. Choi Y.-S. and Bae C.-Y., 2001, “Nonlinear Dynamic Analysis of Partial Rotor Rub with Experimental Observations”, Proc. of *ASME Design Engineering Technical Conferences and Computer and Information in Engineering Conference*, Pittsburgh, pp. 1-8.
15. Choi Y.-S., 2000, “Experimental investigation of partial rotor-rub against a non-rotating part”, Proc. of *IMechE-7th Int. Conf. on Vibrations in Rotating Machinery*, Nottingham, pp. 281-290.
16. Jiang, J. and Ulbrich, H., 2003, “Stability Analysis of Full Annular Rub in Rotor-to-Stator Systems”, *PAMM – Proc. Appl. Math. Mech.*, 2(1), pp. 88-89.
17. Jiang, J. and Ulbrich, H., 2001, “Stability Analysis of Sliding Whirl in a Nonlinear Jeffcott Rotor with Cross-Coupling Stiffness Coefficients”, *Nonlinear Dynamics*, 24, pp. 269-283.
18. Muszynska A., 2002, “Rotor-to-stationary part full annular contact modelling”, *ISROMAC-9 Conference*, February 2002, Honolulu, Hawaii, pp. 1-8.
19. Ehehalt U., Markert R. and Wegener G., 2002, “Stability of Synchronous Forward Whirl at Rotor-Stator-Contact”, *ISROMAC-9 Conference*, February 2002, Honolulu, Hawaii, pp. 1-8.
20. Ehehalt U. and Markert R., 2003, “Instability of Unbalance Excited Synchronous Forward Whirl at Rotor-Stator-Contact”, *PAMM – Proc. Appl. Math. Mech.*, 2(1), pp. 60-61.
21. Ehehalt U. and Markert R., 2003, “Rotor motion during stator contact”, Proc. of *6th IFToMM Int. Conference on Rotor Dynamics*, Sydney, pp. 913-920.

22. Cole M.O.T. and Keogh P.S., 2003, “Asynchronous periodic contact modes for rotor vibration within an annular clearance”, *Proc. Instn. Mech. Engrs.* Vol. 217 Part C: J. Mech. Engr. Sc., pp. 1101-1115.
23. Keogh P.S. and Cole M.O.T., 2003, “Rotor vibration with auxiliary bearing contact in magnetic bearing systems. Part 1: synchronous dynamics”, *Proc. Instn. Mech. Engrs.* Vol. 217 Part C: J. Mech. Engr. Sc., pp. 377-392.
24. Cole M.O.T. and Keogh P.S., 2003, “Rotor vibration with auxiliary bearing contact in magnetic bearing systems. Part 2: synchronous dynamics”, *Proc. Instn. Mech. Engrs.* Vol. 217 Part C: J. Mech. Engr. Sc., pp. 393-409.
25. Adams M.L., 2001, “Rotating Machinery Vibration”, Marcel Dekker Inc., New York, pp. 282-283, 312-319.
26. Yang W. and Tang X., 1994, “Chaotic response of rotor/stator rubs”, Proc. of *4th IFToMM Int. Conference on Rotor Dynamics*, Chicago, pp. 90-96.
27. Yang W., Tang X. and Hogart S., 1996, “Nonlinear Response of Rotor to Stator Rubs”, Nasa CP-3344 *Rotordynamic Instability Problems in High-Performance Turbomachinery*, pp. 269-278.
28. Adams M.L. and Abu-Mahfouz I.A., 1994, “Exploratory research on chaos concepts as diagnostic tools for assessing rotating machinery vibration signatures”, Proc. of *4th IFToMM Int. Conference on Rotor Dynamics*, Chicago, pp. 29-39.
29. Muszynska A. and Goldman P., 1995, “Chaotic Responses of Unbalanced Rotor/Bearing/Stator Systems with Looseness or Rubs”, *Chaos, Solitons & Fractals*, 5(9), pp. 1683-1704.
30. Wu Z. and Chen Y., 2001, “Prediction for the rub-impact phenomena in rotor systems”, Proc. of *ASME Design Engineering Technical Conferences and Computer and Information in Engineering Conference*, Pittsburgh, pp. 1-5.

31. Dai X., Zhang X. and Jin X., 2001, “The partial and full rubbing of a flywheel rotor-bearing-stop system”, *International Journal of Mechanical Sciences*, 43(2), pp. 505-519.
32. Zapoměl J., Fox C.H.J., Malenovský E., 2001, “Numerical Investigation of a Rotor System with Disc-Housing Impact”, *Journal of Sound and Vibration*, Volume: 243(2), pp. 215-240.
33. Sawicki, J.T., 2002, “Some Advances in Diagnostics of Rotating Machinery Malfunctions”, *JSME Annual Meeting 2002 - International Symposium on Machine Condition Monitoring and Diagnosis*, Tokio, pp. 17-24.
34. Feng Z.C and Zhang X-Z, 2002, “Rubbing phenomena in rotor-stator contact”, *Chaos, Solitons & Fractals*, 14(2), pp. 257-267.
35. Hu N.Q. and Wen X.S., 2002, “Chaotic behaviour identification of a rub-impact rotor using short-term predictability of measured data”, *Proc. Instn. Mech. Engrs.* Vol. 216 Part C: J. Mech. Engr. Sc., pp. 675-681.
36. Yuan H.Q., Wang D.Y., Yang J.D., Liu Y.X. and Wen B.C., 2002, “Study on the bifurcation and chaos behavior of rubbing rotor-stator systems”, Proc. of *6th IFToMM Int. Conference on Rotor Dynamics*, Sydney, pp. 984-988.
37. Lucifredi A., Magnetto A. and Silvestri P., 2002, “Experimental validation of an original software package based on chaos theory for monitoring and diagnostics of rotating machinery”, Proc. of *6th IFToMM Int. Conference on Rotor Dynamics*, Sydney, pp. 257-264.
38. Zhang Y., Wen B. and Leung A.Y.T., 2002, “Reliability Analysis for Rotor Rubbing”, *ASME Journal of Vibration and Acoustics*, 124(1), pp. 58-62.
39. Zhang Y.M. and Wen B.C., 2002, “Uncertain responses of rotor systems with rubbing”, Proc. of *6th IFToMM Int. Conference on Rotor Dynamics*, Sydney, pp. 989-994.
40. Qin W., Chen G. and Meng G., 2004, “Nonlinear responses of a rub-impact overhung rotor”, *Chaos, Solitons & Fractals*, 19(5), pp. 1161-1172.

41. Ehrich F.F., 1976, “Self Excited Vibrations”, *Shock and Vibration Handbook*, Chapter 5, McGraw-Hill.
42. Kennedy F.E., 1982, “Single Pass Rub Phenomena – Analysis and Experiment, ASME Journal of Lubrication Technology, 104(4), pp. 582-588.
43. Hashemi Y., 1984, “Vibration problems with thermally induced distortions in turbine generator rotors”, *IMechE paper C271/84*, pp. 481-490.
44. Larsson B., 1999, “Journal Asymmetric Heating – Part I: Non Stationary Bow”, *ASME Journal of Tribology*, 121(1), pp. 157-163.
45. Larsson B., 1999, “Journal Asymmetric Heating – Part II: Alteration of Rotor Dynamic Properties”, *ASME Journal of Tribology*, 121(1), pp. 164-168.
46. Larsson B., 2000, “Rub-heated shafts in turbines”, Proc.of *IMechE-7th Conference Vibrations in Rotating Machinery*, pp 269-278.
47. Larsson B., 2003, “Heat Separation in Frictional Rotor-Seal Contact”, *ASME Journal of Tribology*, 125(3), pp. 600-607.
48. Takahashi N., Hiroshima M., Miura H. and Fukushima Y., 2003, “Instability Induced by Iron Losses in Rotor-Active Magnetic Bearing System, Proc. of *ISCORMA-2*, Gdańsk, pp. 1-10.
49. Yanabe S., 1998, “Whirl Simulation of a Rotor Colliding with Annular Guard during Acceleration”, Proc. of *5th IFToMM Int. Conference on Rotor Dynamics*, Darmstadt, pp. 780-789.
50. Vania, A., Bachschmid, N. and Pennacchi, P., 2001, “Analysis of Light Rotor-to-Stator Contacts in Large Turbine-Generator Units”, Proc. of *Surveliance 4 – Acoustical and Vibratory Surveillance Methods and Diagnostic Techniques*, Compiègne, pp. 507-516.
51. Bachschmid, N., Pennacchi, P., Vania, A., Zanetta, G.A. and Gregori, L., 2003, “Identification of Rub and Unbalance in a 320MW Turbogenerator”, *International Journal of Rotating Machinery*, 9(2), pp.97-112.

52. Kellenberger, W., 1980, “Spiral vibrations due to the seal rings in turbogenerators thermally induced interaction between rotor and stator”, *Journal of Mechanical Design*, Vol. 102(1), pp. 177-184.
53. Schmied J., 1987, “Spiral Vibration of Rotors”, Proc. of *ASME Design Technology Conference*, Boston, pp. 449-456.
54. Stegemann D., Reimche W., Beermann H. and Südmersen U., 1993, “Analysis of Short-Duration Rubbing Process in Steam Turbines”, *VGB Kraftwerkstechnik*, 73(10), pp. 739-745.
55. Muzynska A., 1993, “Thermal rub effect in rotating machines”, *ORBIT*, Bently Nevada, 14(1), pp. 8-13.
56. Liebich, R. and Gasch, R., 1996, “Spiral vibrations - modal treatment of a rotor-rub problem based on coupled structural/thermal equations”, Proc. of *IMechE-6th Conference Vibrations in Rotating Machinery* C500/042/96, pp 405-413.
57. Newkirk, B.L., 1926, “Shaft rubbing: relative freedom of rotor shafts from sensitiveness to rubbing contact when running above their critical speeds”, Mechanical Engineering, 48(8), pp. 830-832.
58. Taylor H.D., 1924, “Rubbing shafts above and below the resonance speed (critical speed), General Electric Company, R-16709, Schenectady, NY.
59. Liebich, R., 1998, “Rub induced non-linear vibrations considering the thermo-elastic effect”, Proc. of *5th IFToMM Int. Conference on Rotor Dynamics*, Darmstadt, pp. 802-815.
60. Gruber J., 1998, “A Contribution to the Rotor Stator Contact”, Proc. of *5th IFToMM Int. Conference on Rotor Dynamics*, Darmstadt, pp. 768-779.
61. Sawicki, J.T., Montilla-Bravo, A. and Gosiewski, Z., 2003, “Thermomechanical Behaviour of Rotor with Rubbing”, *International Journal of Rotating Machinery*, 9(1), pp. 41-47.

62. Bachschmid, N., Pennacchi, P. and Venini, P., 2000, “Spiral Vibrations in Rotors Due to a Rub”, Proc. of *IMechE-7th Int. Conf. on Vibrations in Rotating Machinery*, Nottingham, pp.249-258.
63. Bachschmid, N., Pennacchi, P. and Vania, A., 2001, “Spiral Vibrations Due to Rub: Numerical Analysis and Field Experiences”, *Schwingungen in Rotierenden Maschinen V*, H. Irretier, R. Nordmann, H. Springer Editors, Vieweg Verlag, Braunschweig/Wiesbaden, Germany, pp. 61-74.
64. Bachschmid N., Pennacchi P. and Vania A., 2004, “Modelling of Spiral Vibrations Due to Rub in Real Rotors”, paper ISROMAC10-2004-096, *ISROMAC-10 Conference*, March, Honolulu, Hawaii, pp. 1-10.
65. Lalanne M. and Ferraris G., 1998, “Rotordynamics Prediction in Engineering”, John Wiley & Sons Inc, Chichester, England.
66. Kapitaniak T., 2000, “Chaos for Engineers”, Springer Verlag, Berlin, pp. 23-27.
67. Morton K.W. and Mayers D.F., 1994, “Numerical solution of partial differential equations: an introduction”, Cambridge University Press, pp.1-227.
68. Thomas J.W., 1995, “Numerical partial differential equations: finite difference methods”, Springer, pp. 1-437.

APPENDIX 1

Fourier's equation (8) is a parabolic PDE that is solved by means of numerical methods. If the solution methods were implicit, the convergence of the solution would be guaranteed independent of the time step *dt* chosen and the equation would be said to be unconditionally stable. Since the method used is explicit, the equation is no longer unconditionally stable and the time step must satisfy special conditions. Some examples are reported in [67,68], but in general for a parabolic, free PDE like:

$$\frac{\partial T}{\partial t} = \frac{K}{\rho C}\left[\frac{\partial^2 T}{\partial x^2} + \frac{\partial^2 T}{\partial y^2} + \frac{\partial^2 T}{\partial z^2}\right] \tag{21}$$

the condition, necessary and sufficient, is:

$$\frac{K}{\rho C}\left[\frac{\Delta T}{(\Delta x)^2} + \frac{\Delta T}{(\Delta y)^2} + \frac{\Delta T}{(\Delta z)^2}\right] \leq \frac{1}{2} \tag{22}$$

while the condition only becomes necessary when the equation is forced as in case of eq. (12). There exist mathematical methods that guarantee the sufficient condition also in case of forced parabolic PDE, but they require knowledge of the exciting term. Since in the considered case, the force, i.e. the last term of eq. (12) is function of the time, this condition should be evaluated for each step of the calculation, being of difficult application. So the approach used was heuristic. It has been noticed that there is a strong relationship between the geometrical dimensions of the elements of the 3D mesh and the time step: the smaller the element, the smaller the time step. A linear relationship does not exist, but in each one of the considered cases several simulations were made by reducing the time step until the convergence of the solution was reached.

APPENDIX 2

The rotor model of the industrial turbine is made of 33 nodes and the bearings are located in nodes 5 and 31. The sealing is centred in node 19 and the original rotor unbalance was positioned in the same node. Dynamic coefficients of the bearing are reported in Figure 45 to Figure 48. Simulation parameters are listed in Table 1.

APPENDIX 3

The rotor model of the generator is made of 94 nodes and the bearings are located in nodes 7, 43, 78, 88 and 92. The rubbing section is centred in node 70 and the original rotor unbalance was positioned in the same node. Simulation parameters are listed in Table 2.

Table 1 Simulation parameters for the industrial turbine.

Model parameters		
Mass per unit volume	[kg/m^3]	7850
Young' modulus	[N/m^2]	2.06E+11
Poisson's coefficient		0.29
Rubbing section parameters		
Seal stiffness k_s	[N/m]	4e+6
Seal width	[m]	0.2
Clearance R	[μm]	100
Horizontal misalignment $x_{O'}$	[μm]	10
Vertical misalignment $y_{O'}$	[μm]	10
Friction coefficient		0.2
Thermal parameters		
Thermal conductivity coefficient K	[W/m K]	50
Specific heat C	[J/kg K]	440
Thermal convective coefficient H	[W/m^2 K]	35
thermal expansion coefficient $\hat{\alpha}$	[1/K]	0.000015
Initial temperature T_0	[K]	25
Temperature of the surrounding fluid T_f	[K]	25
Axial step of thermal mesh dl	[m]	0.092
Radial step of thermal mesh dr	[m]	0.0838
Angular step of thermal mesh $d\theta$	[°]	10
Number of the nodes of the axial thermal mesh corresponding to the finite beam model		13
Number of the nodes of the radial thermal mesh		5
Number of the nodes of the angular thermal mesh		36
Number of the angular nodes of the contact between rotor and seal		2
Number of the axial nodes of the contact between rotor and seal		3
Rotor characteristics		
Rotor overall length	[m]	7.08
Distance between brg. #1 and brg. #2	[m]	5.74
Distance between brg. #1 and rubbing section	[m]	3.09

Eigenfrequencies calculated at 1950 [rpm]

	[rpm]	[Hz]	dimensionless damping
No. 1	2040.20	34.00	8.79071e-002

No. 2	4370.64	72.84	1.01703e-001
No. 3	4374.21	72.90	7.51402e-002
No. 4	4953.25	82.55	8.06705e-002
No. 5	4980.67	83.01	8.08865e-002
No. 6	7804.17	130.07	2.92243e-001
No. 7	7994.74	133.25	2.37350e-001

Table 2 Simulation parameters for the generator.

Model parameters		
Mass per unit volume	[kg/m^3]	7850
Young' modulus	[N/m^2]	1.95E+11
Poisson's coefficient		0.29
Rubbing section parameters		
Stator section stiffness k_s	[N/m]	4e+6
Stator section width	[m]	0.08
Clearance R	[μm]	100
Horizontal misalignment $x_{O'}$	[μm]	10
Vertical misalignment $y_{O'}$	[μm]	10
Friction coefficient		0.2
Thermal parameters		
Thermal conductivity coefficient K	[W/m K]	50
Specific heat C	[J/kg K]	440
Thermal convective coefficient H	[W/m^2 K]	35
Thermal expansion coefficient $\widehat{\alpha}$	[1/K]	0.000015
Initial temperature T_0	[K]	25
Temperature of the surrounding fluid T_f	[K]	25
Axial step of thermal mesh dl	[m]	0.0369
Radial step of thermal mesh dr	[m]	0.0244
Angular step of thermal mesh $d\theta$	[°]	10
Number of the nodes of the axial thermal mesh corresponding to the finite beam model		13
Number of the nodes of the radial thermal mesh		5
Number of the nodes of the angular thermal mesh		36
Number of the angular nodes of the contact between rotor and seal		2
Number of the axial nodes of the contact between rotor and seal		3
Rotor characteristics		
Rotor overall length	[m]	11.61
Distance between brg. #1 and brg. #2	[m]	5.41
Distance between brg. #2 and brg. #3	[m]	2.07
Distance between brg. #3 and brg. #4	[m]	1.55
Distance between brg. #4 and brg. #5	[m]	1.21
Distance between brg. #2 and rubbing section	[m]	1.71

Eigenfrequencies calculated at 1250 [rpm]			
	[rpm]	[Hz]	dimensionless damping

No. 1	1278.96	21.32	7.23269e-002
No. 2	1795.18	29.92	5.27878e-002
No. 3	2510.42	41.84	7.39130e-002
No. 4	2524.86	42.08	5.98773e-002
No. 5	2913.22	48.55	6.76651e-002
No. 6	3080.80	51.35	2.34159e-002
No. 7	3107.55	51.79	2.71323e-001
No. 8	3957.32	65.96	7.09329e-002
No. 9	3973.64	66.23	1.39198e-002

FIGURE CAPTIONS

Figure 1. Flowchart of the proposed domain swap method.

Figure 2. Reference systems employed: $S(x,O,y)$ is rigidly connected to the seal; $S'(x',O',y')$ has the axes parallel to those of S and is centred in the centre O' of the rotor orbit; $S''(x'',O'',y'')$ coincide with the of the elliptic orbit axes (x'' coincident with major axis).

Figure 3. Position of the elliptical orbit with respect to the reference systems adopted. KP is the key-phasor dot.

Figure 4. Comparison between the orbit and the clearance.

Figure 5. Large partial annular rub of type I.

Figure 6. Deflection in large partial annular rub of type I.

Figure 7. Large partial annular rub of type II.

Figure 8. Deflection in large partial annular rub of type II.

Figure 9. Full annular rub.

Figure 10. Deflection in full annular rub.

Figure 11. Reference of point STR.

Figure 12. Reference system on the rotor.

Figure 13. Definition of the hot spot phase in the rotor reference system.

Figure 14. Contact forces on the rotor.

Figure 15. 3D mesh for the temperature distribution calculation.

Figure 16. Boundary condition of a general element.

Figure 17. Strain ε_z in the HS section and equivalent distribution.

Figure 18. Equivalent bending moments.

Figure 19. Rotor model.

Figure 20. Frequency response due to unbalance in the seal and corresponding orbits in the bearings at 1900 rpm.

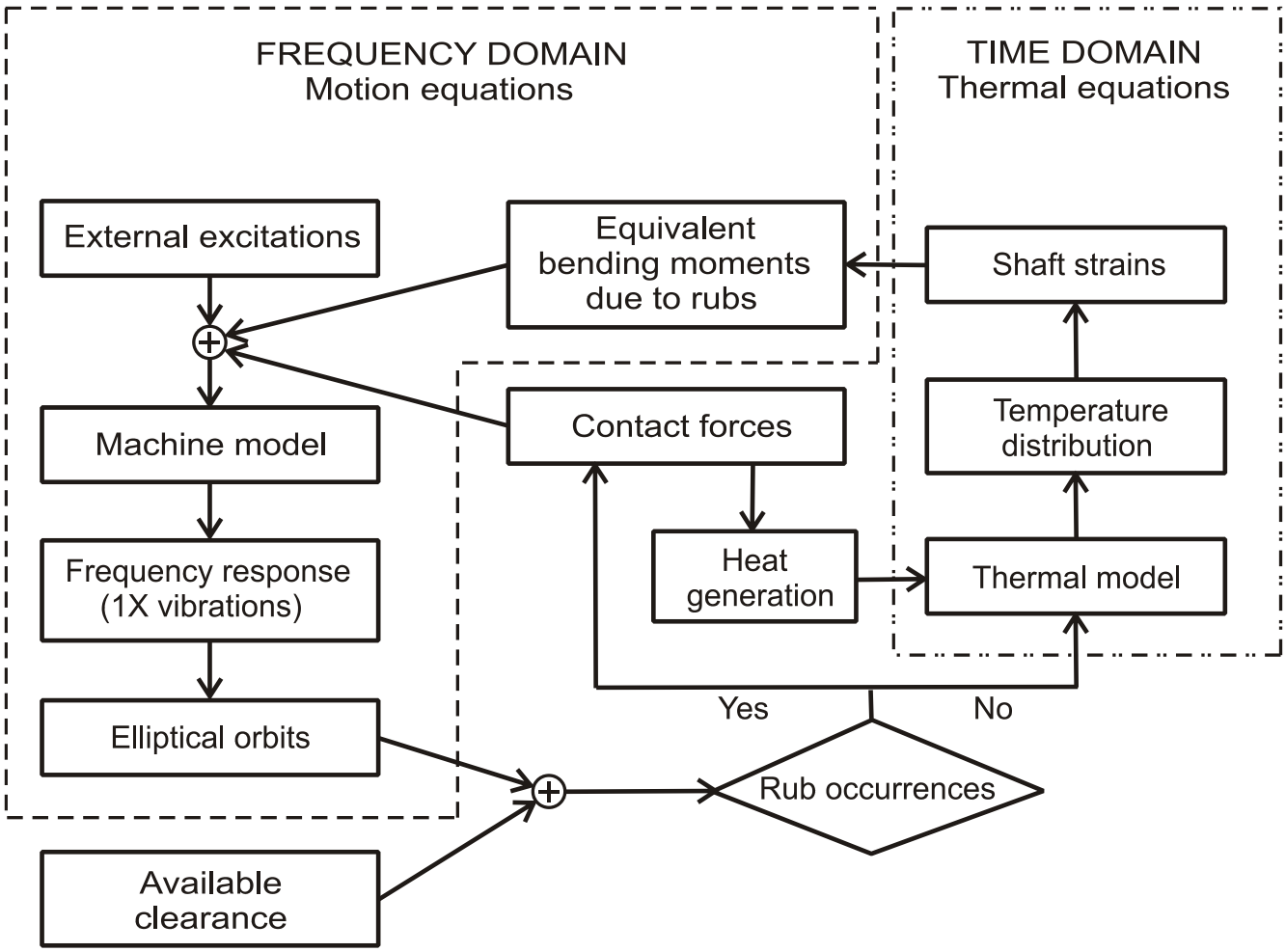

Figure 1. Flowchart of the proposed domain swap method.

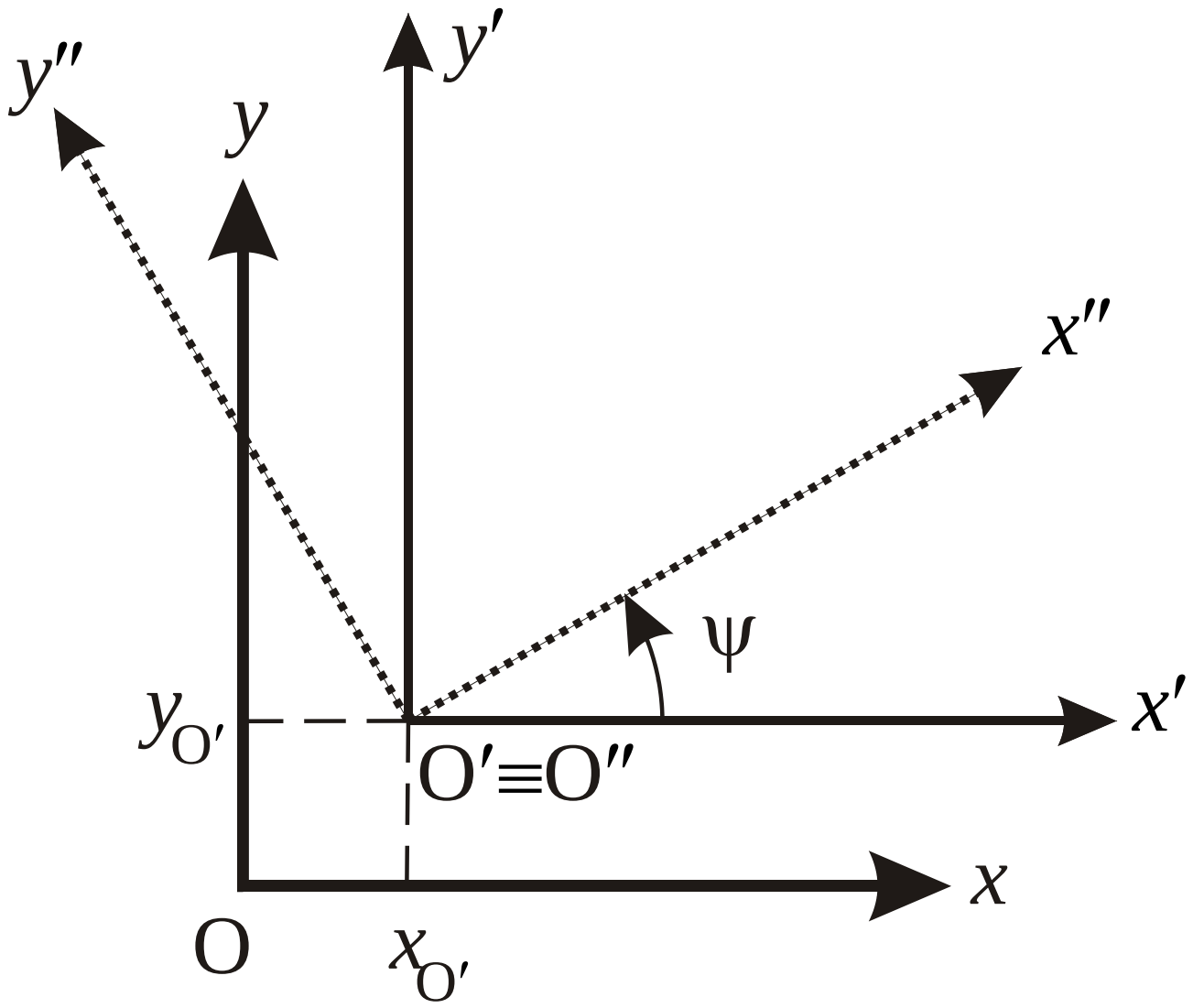

Figure 2. Reference systems employed: $S(x,O,y)$ is rigidly connected to the seal; $S'(x',O',y')$ has the axes parallel to those of S and is centred in the centre O' of the rotor orbit; $S''(x'',O'',y'')$ coincide with the of the elliptic orbit axes (x'' coincident with major axis).

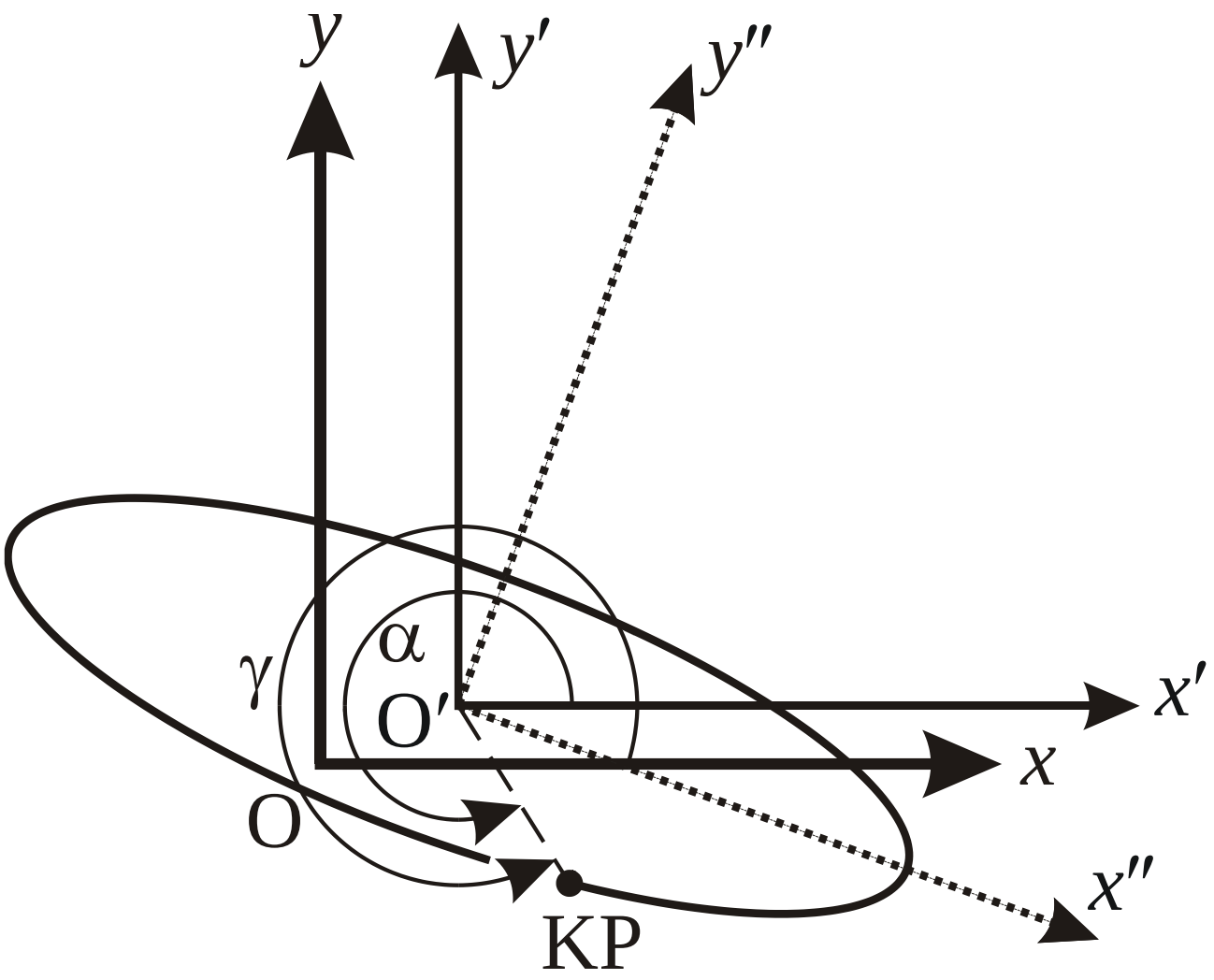

Figure 3. Position of the elliptical orbit with respect to the reference systems adopted. KP is the key-phasor dot.

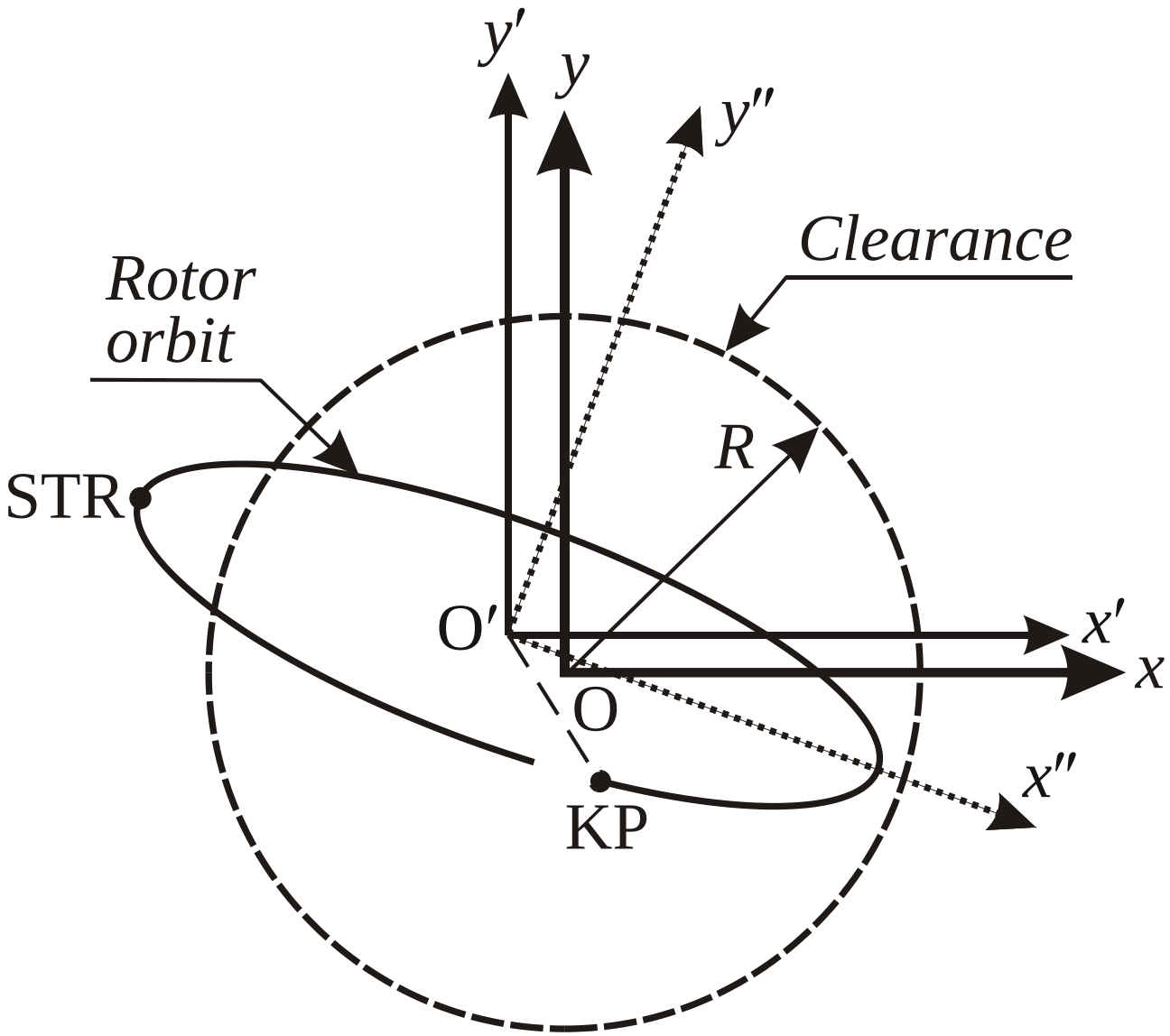

Figure 4. Comparison between the orbit and the clearance.

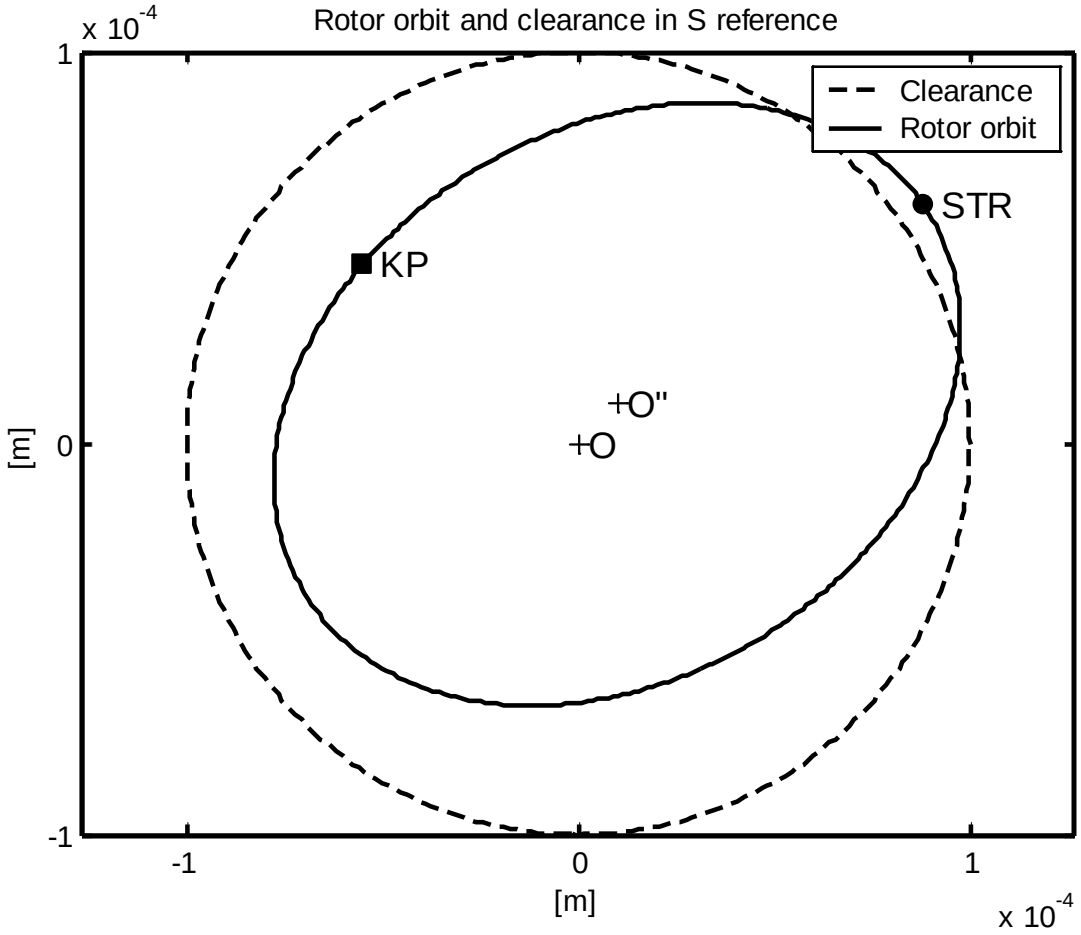

Figure 5. Large partial annular rub of type I.

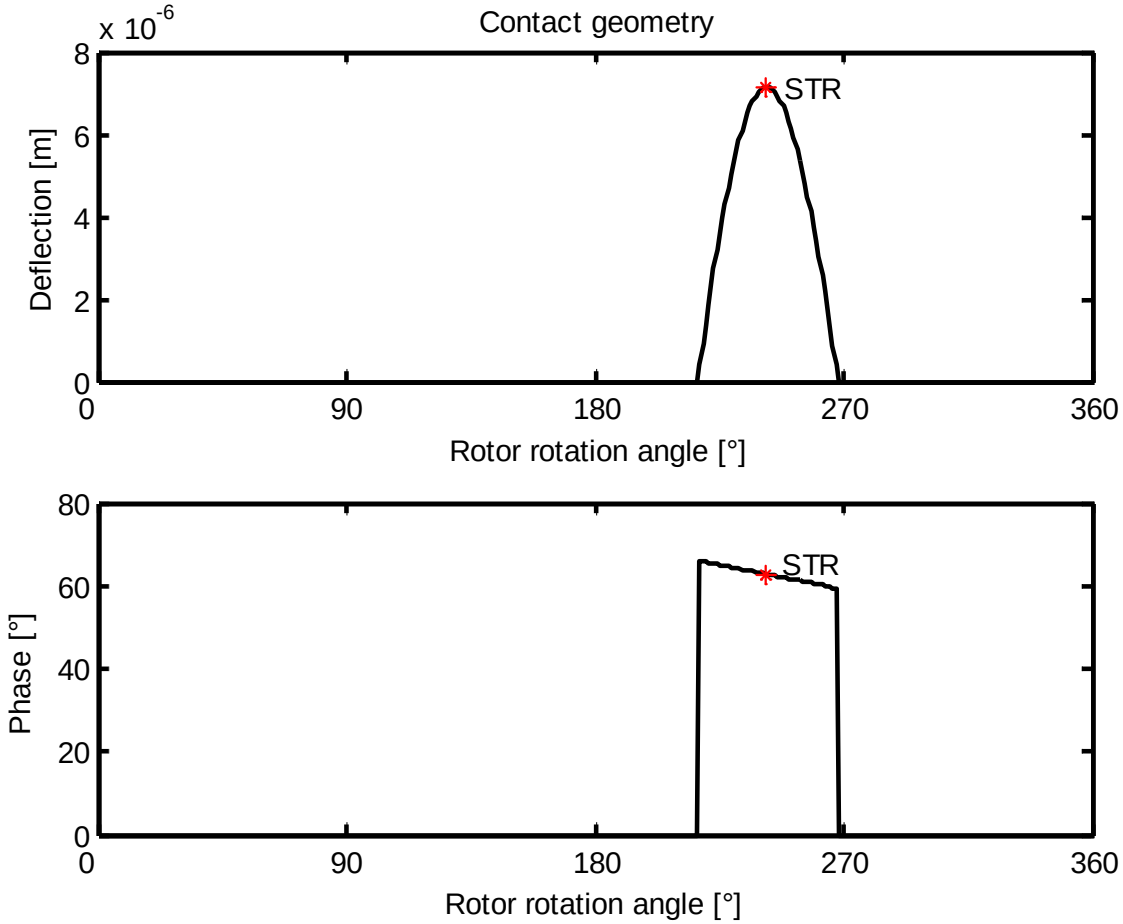

Figure 6. Deflection in large partial annular rub of type I.

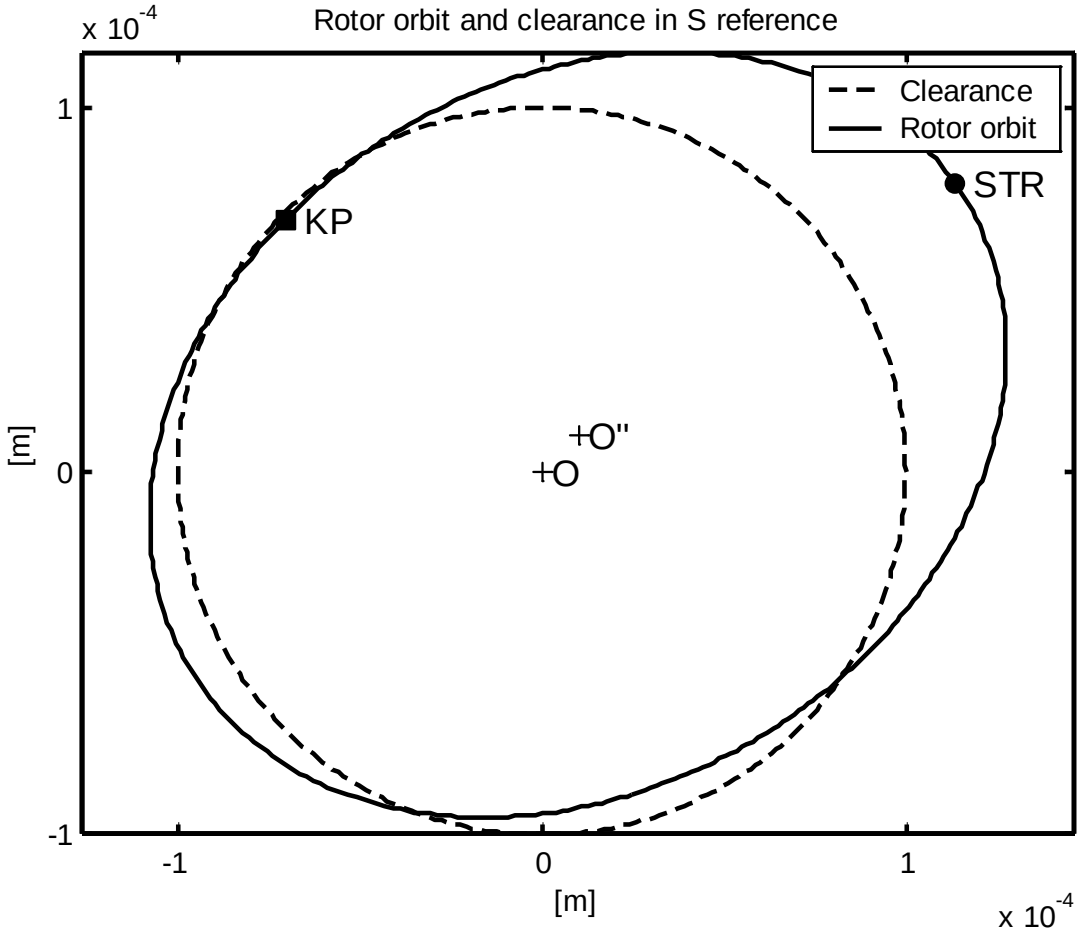

Figure 7. Large partial annular rub of type II.

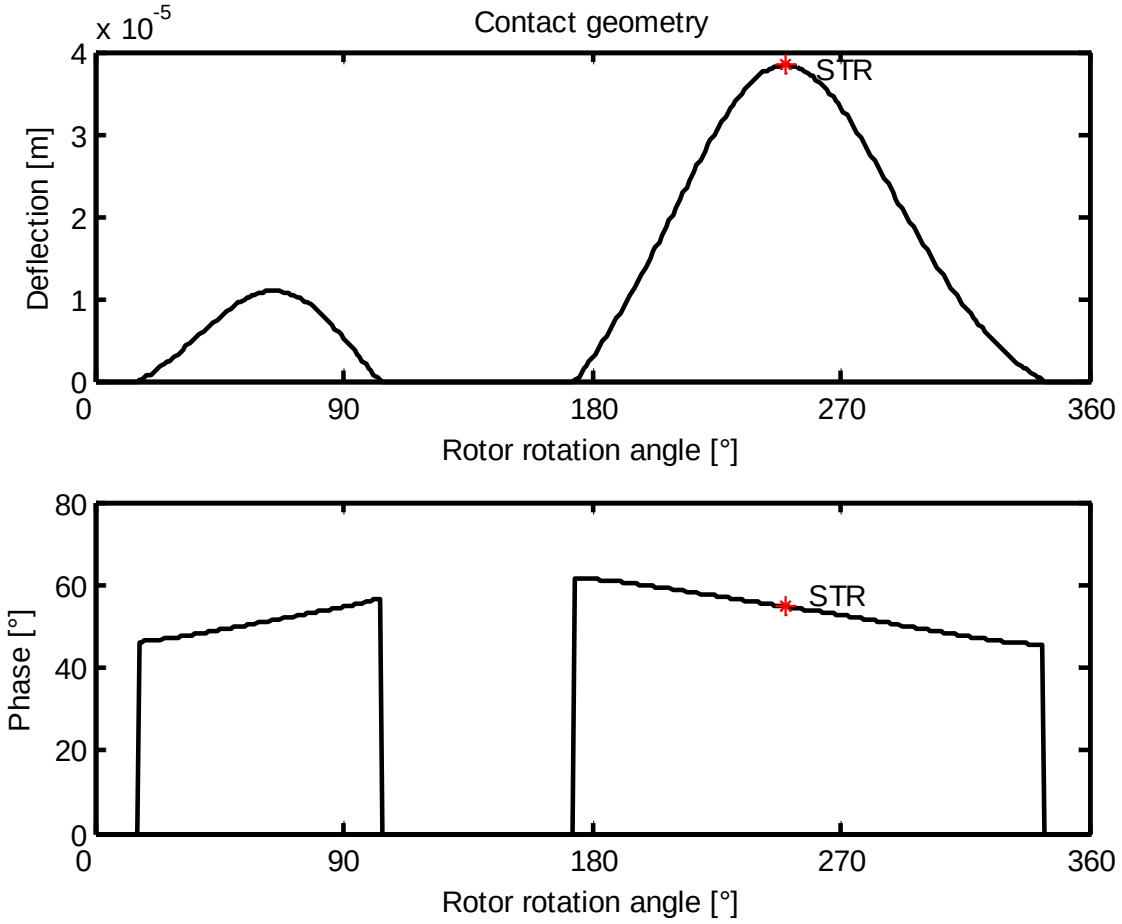

Figure 8. Deflection in large partial annular rub of type II.

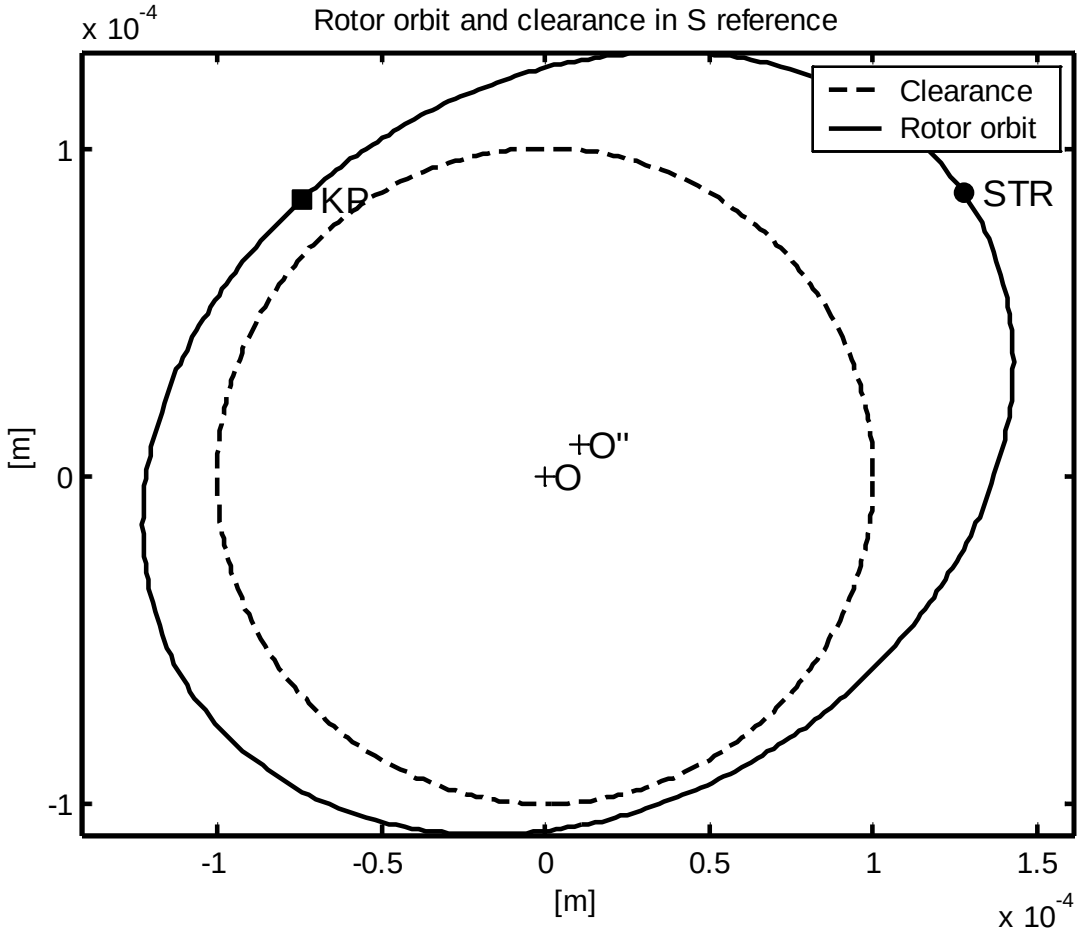

Figure 9. Full annular rub.

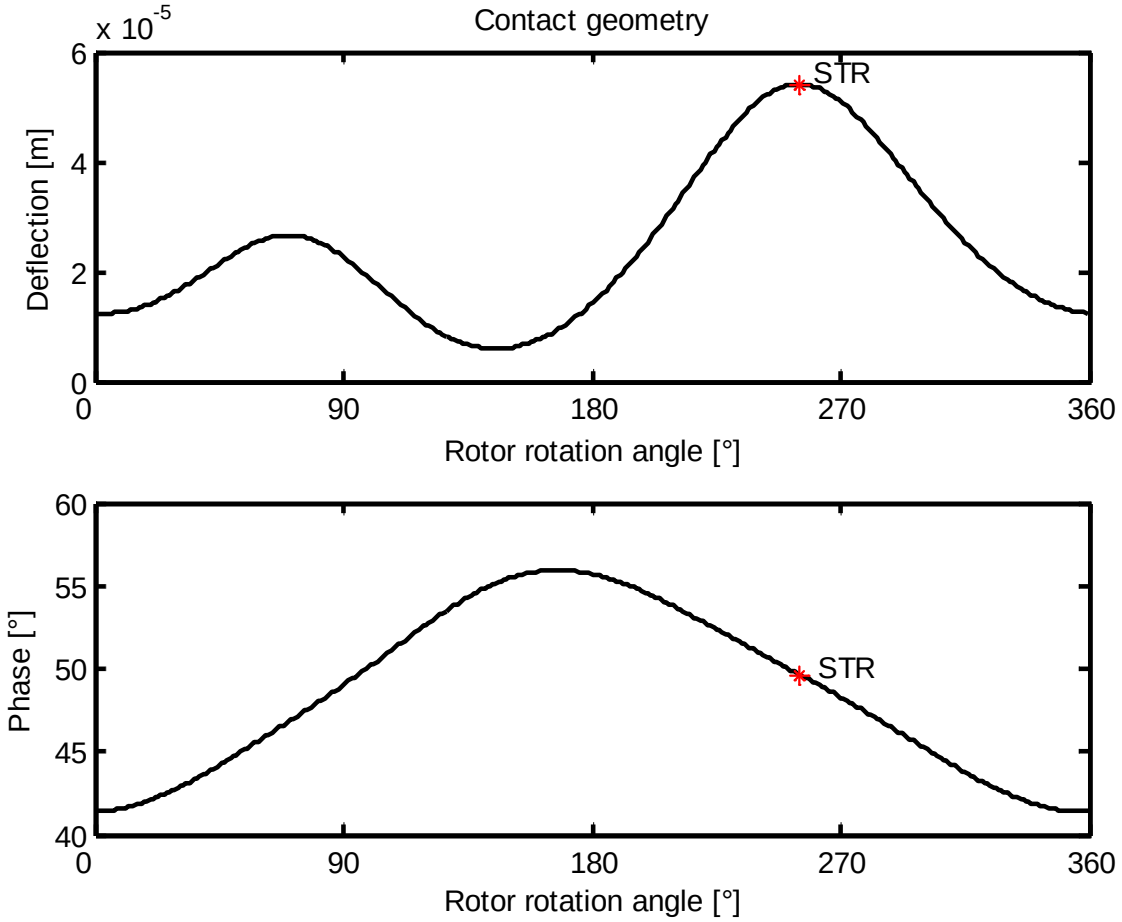

Figure 10. Deflection in full annular rub.

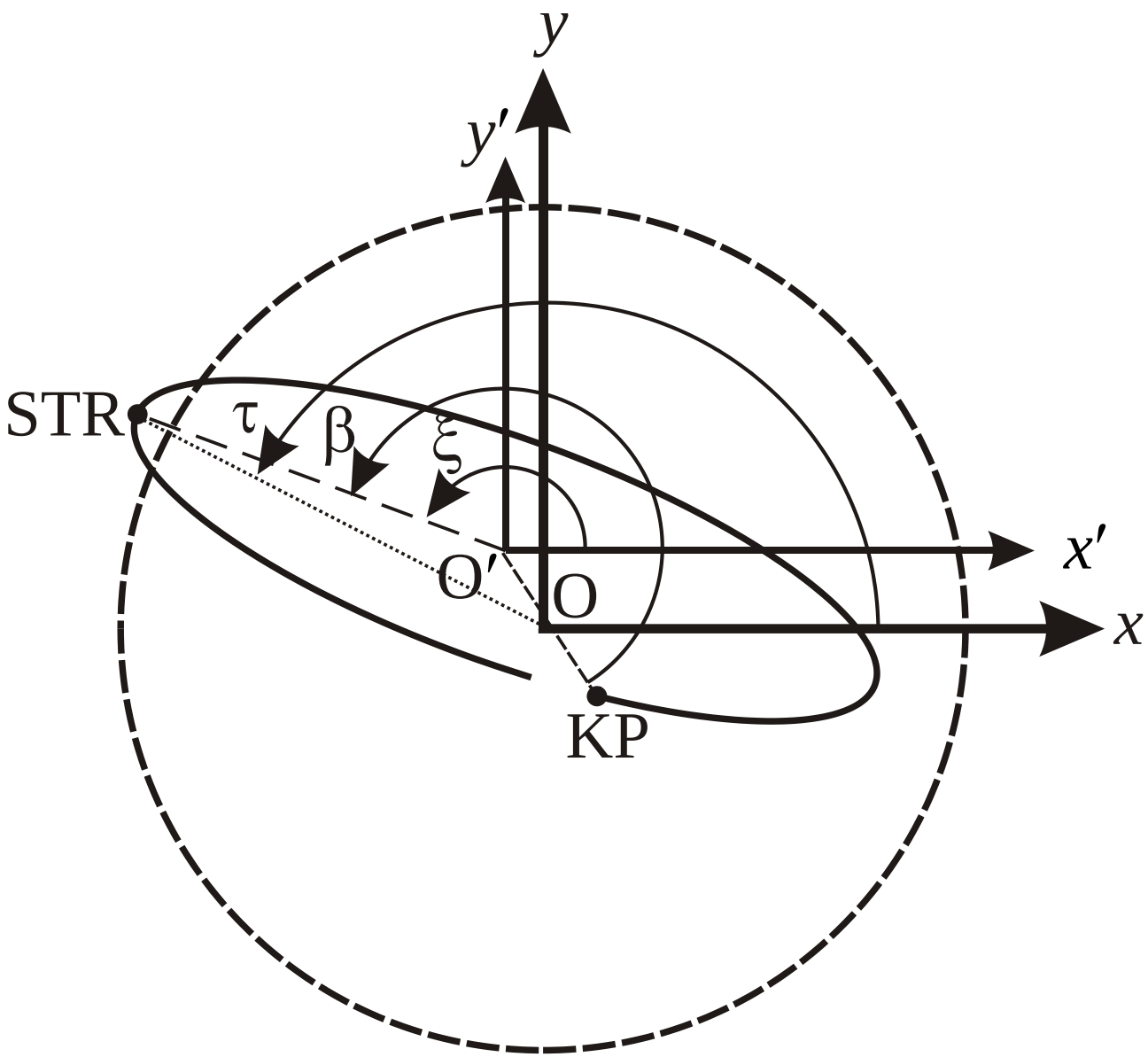

Figure 11. Reference of point STR.

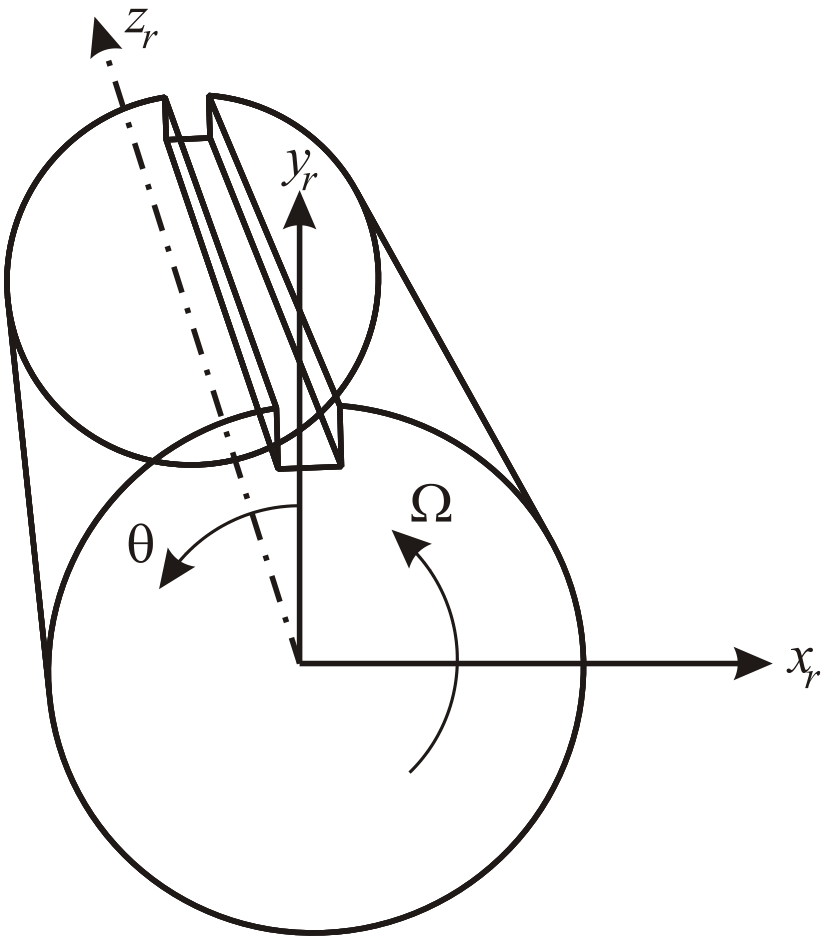

Figure 12. Reference system on the rotor. The notch indicates the phase reference position.

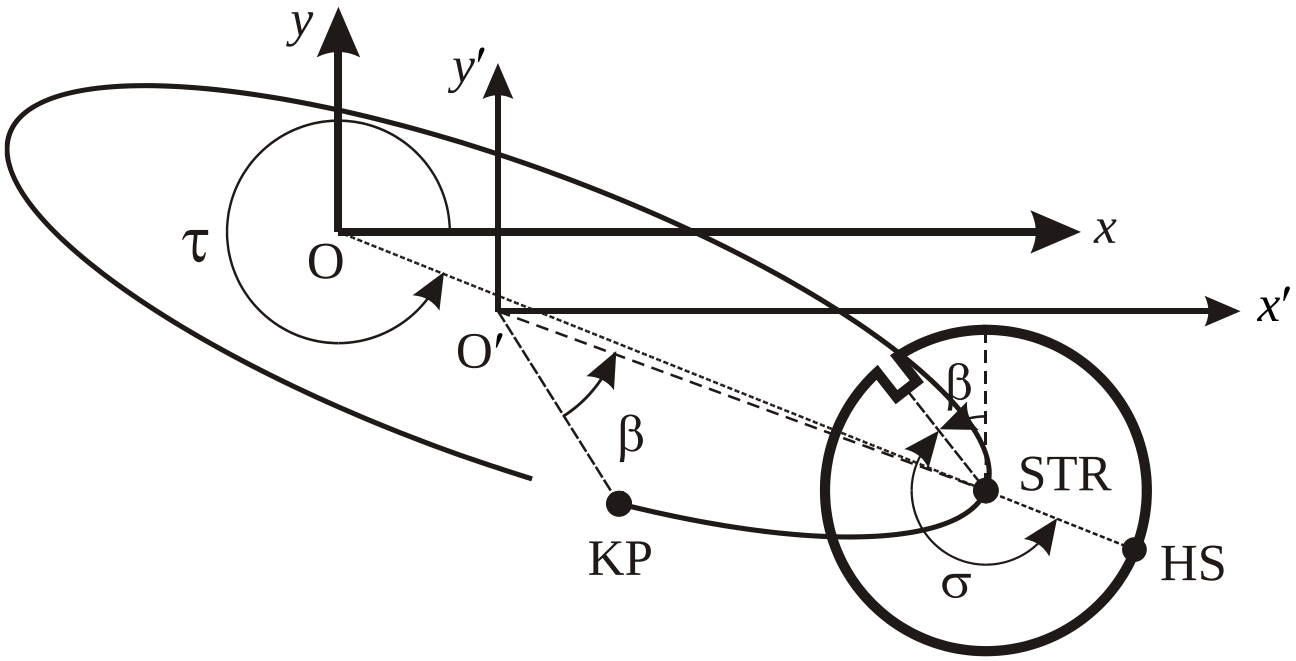

Figure 13. Definition of the hot spot phase in the rotor reference system.

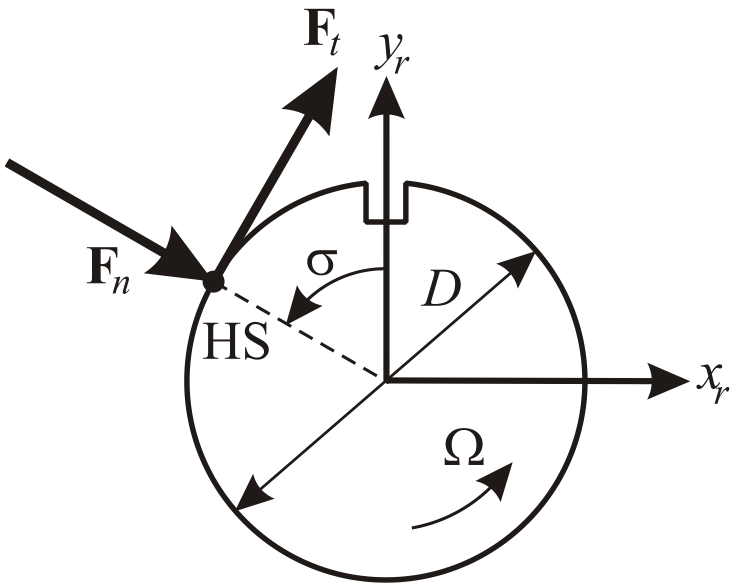

Figure 14. Contact forces on the rotor.

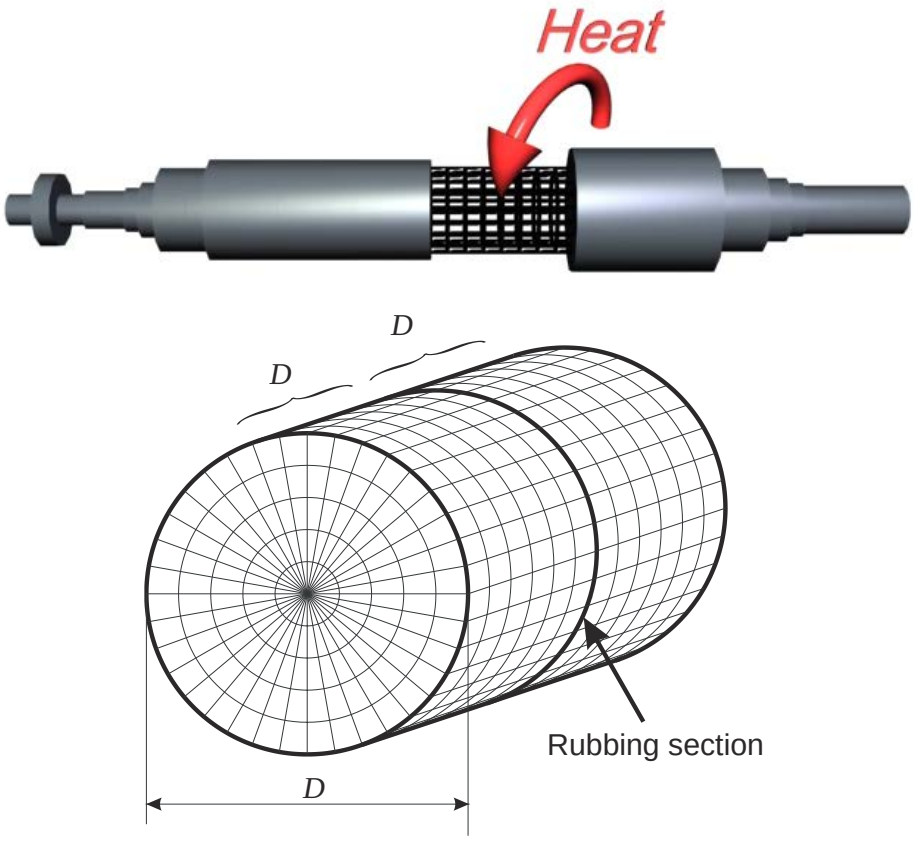

Figure 15. 3D mesh for the temperature distribution calculation.

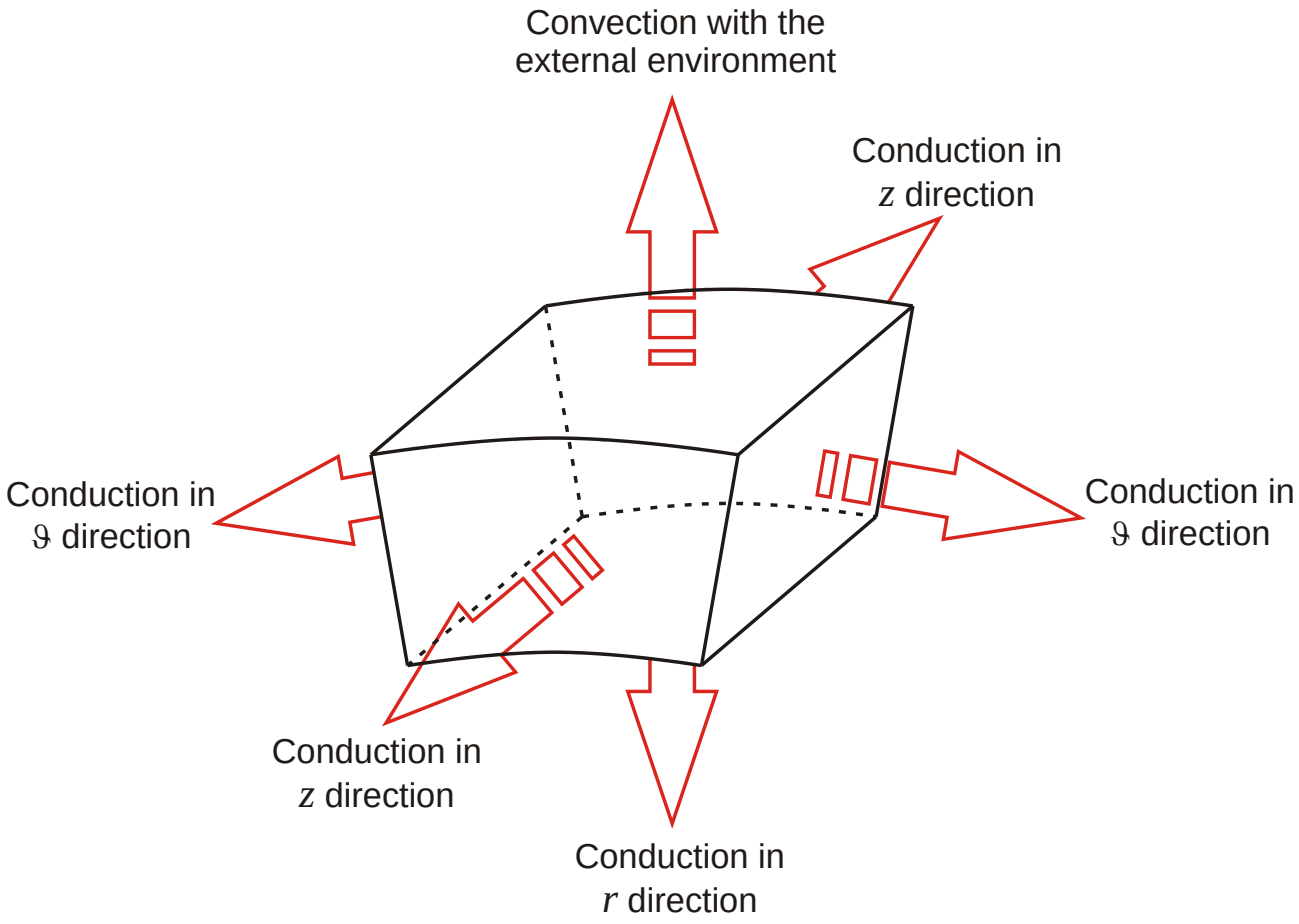

Figure 16. Boundary condition of a general element.

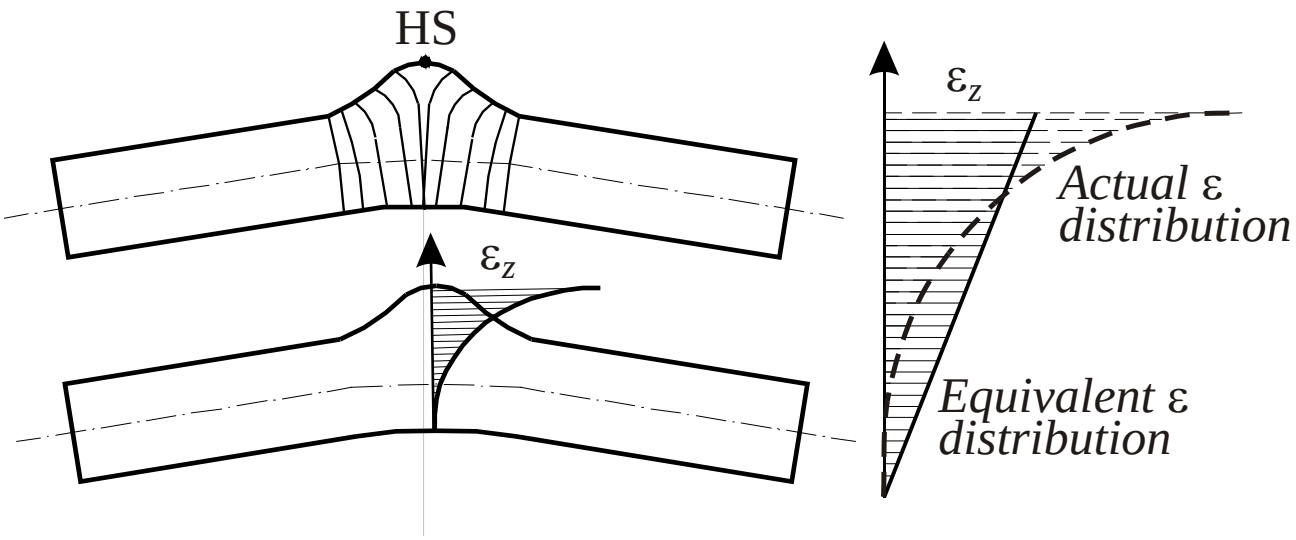

Figure 17. Strain ε_z in the HS section and equivalent distribution.

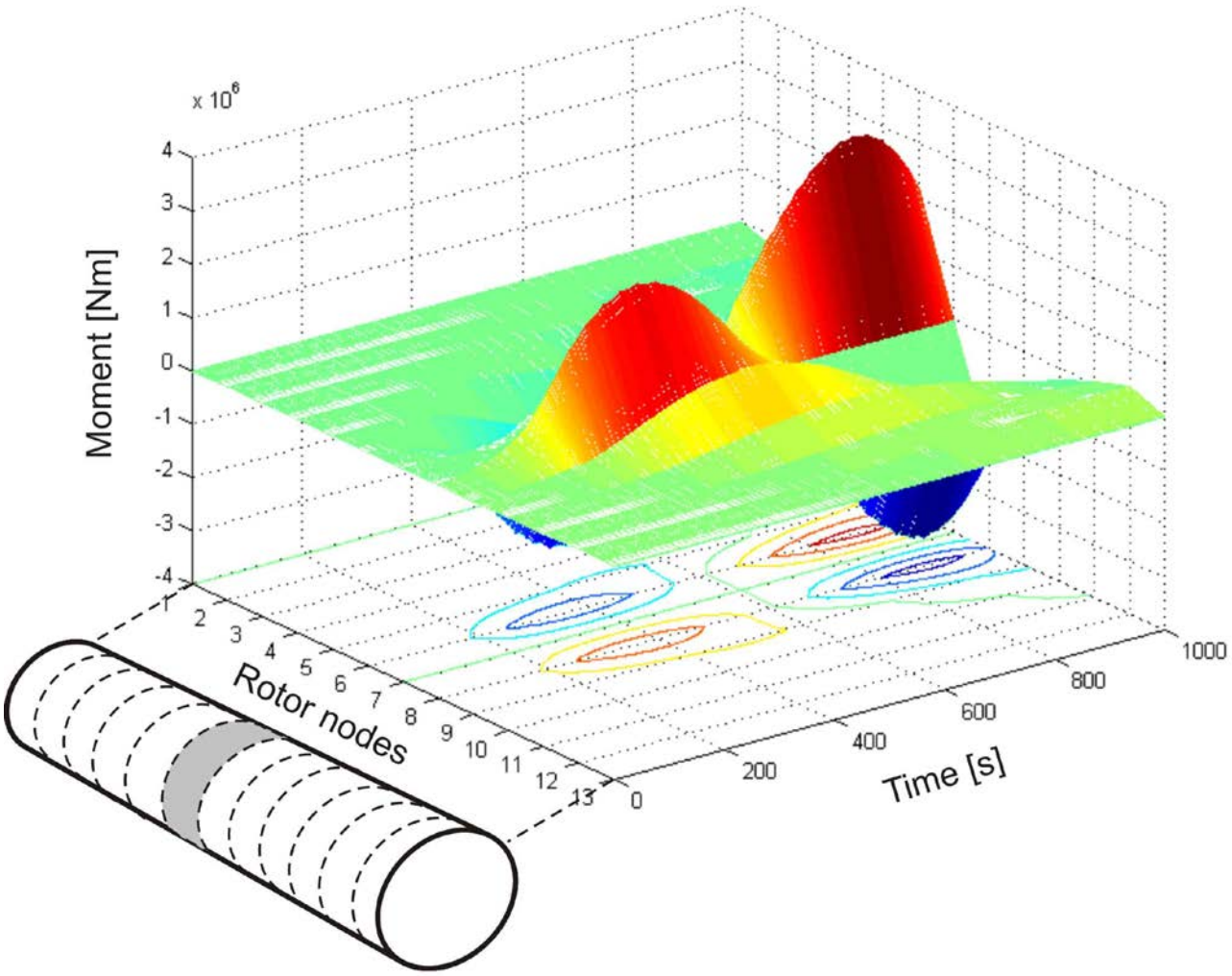

Figure 18. Equivalent bending moments.

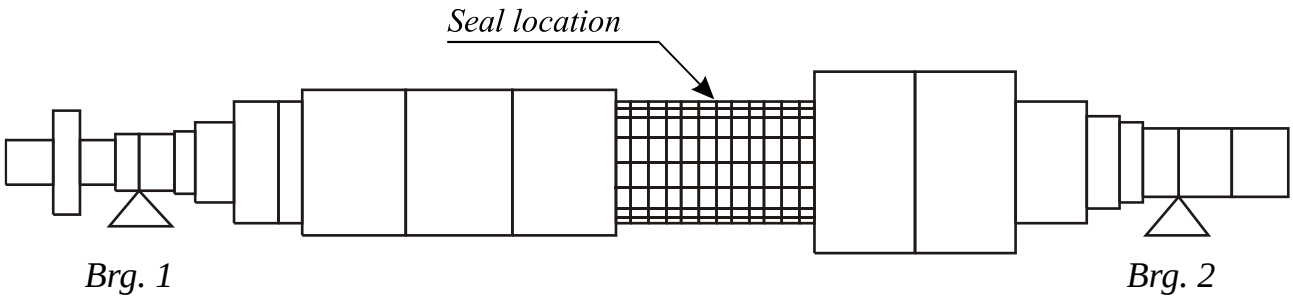

Figure 19. Rotor model.

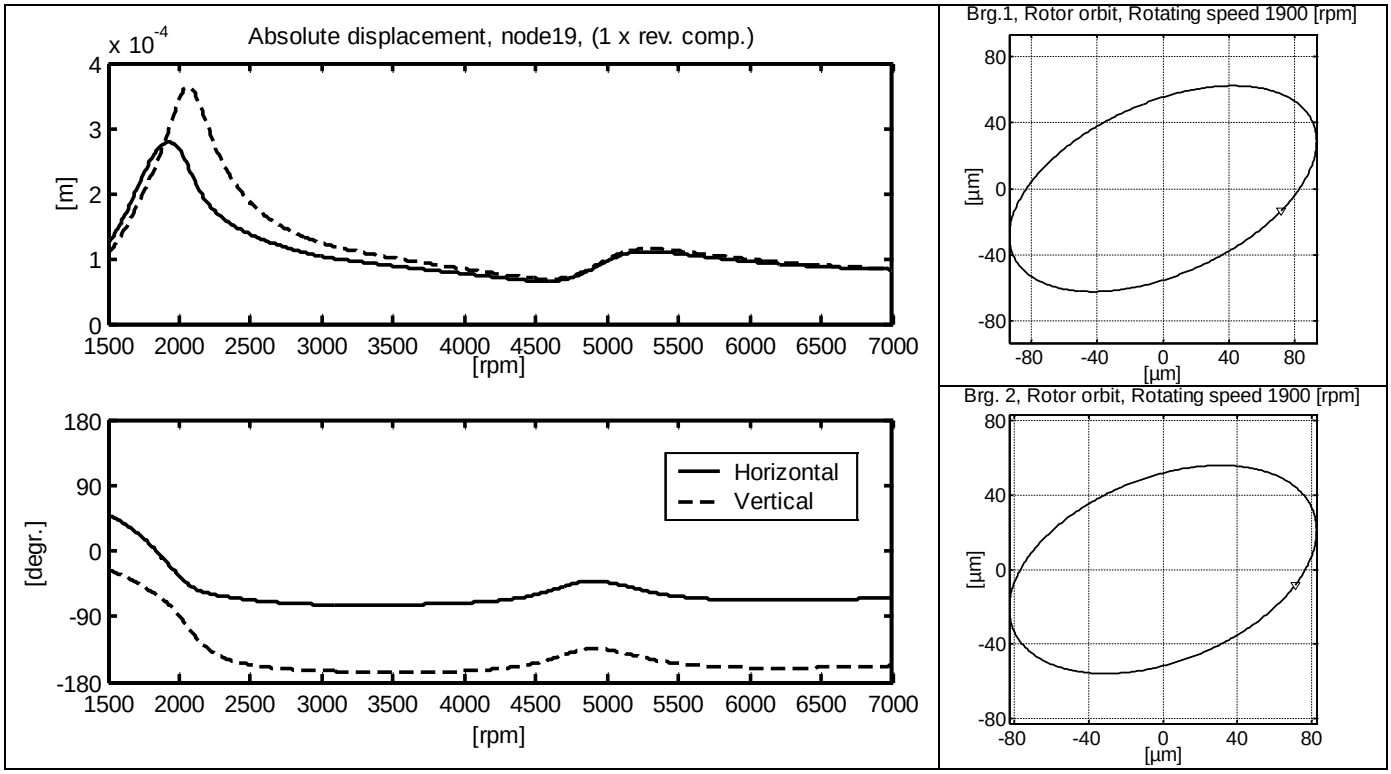

Figure 20. Frequency response due to unbalance in the seal and corresponding orbits in the bearings at 1900 rpm.

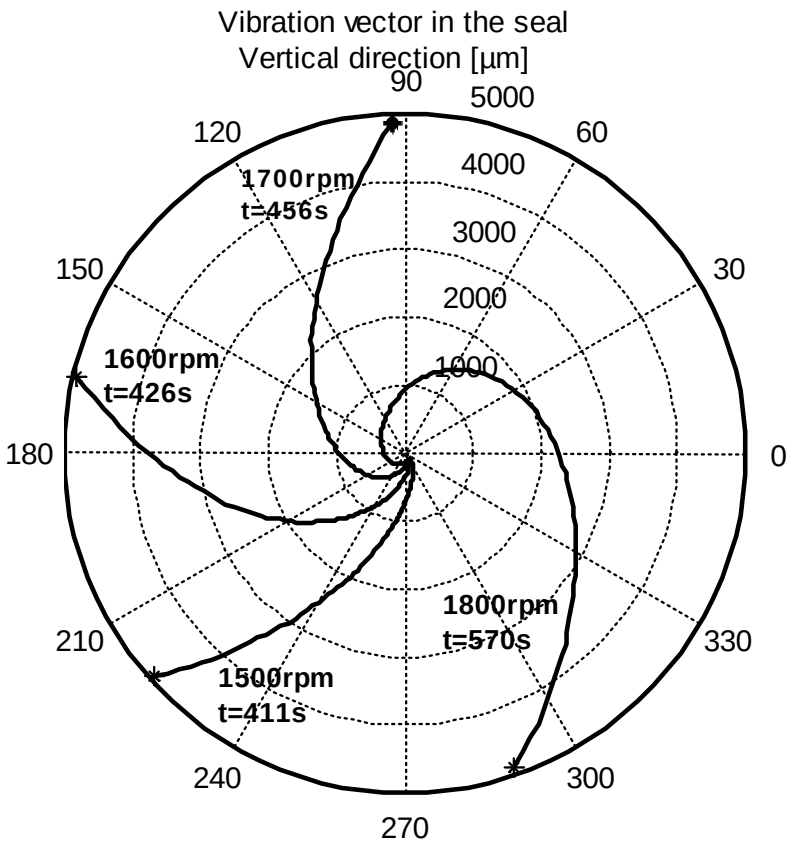

Figure 21. Polar plot of the vibration vector in vertical direction in the speed range 1500-1800 rpm: spiral instability.

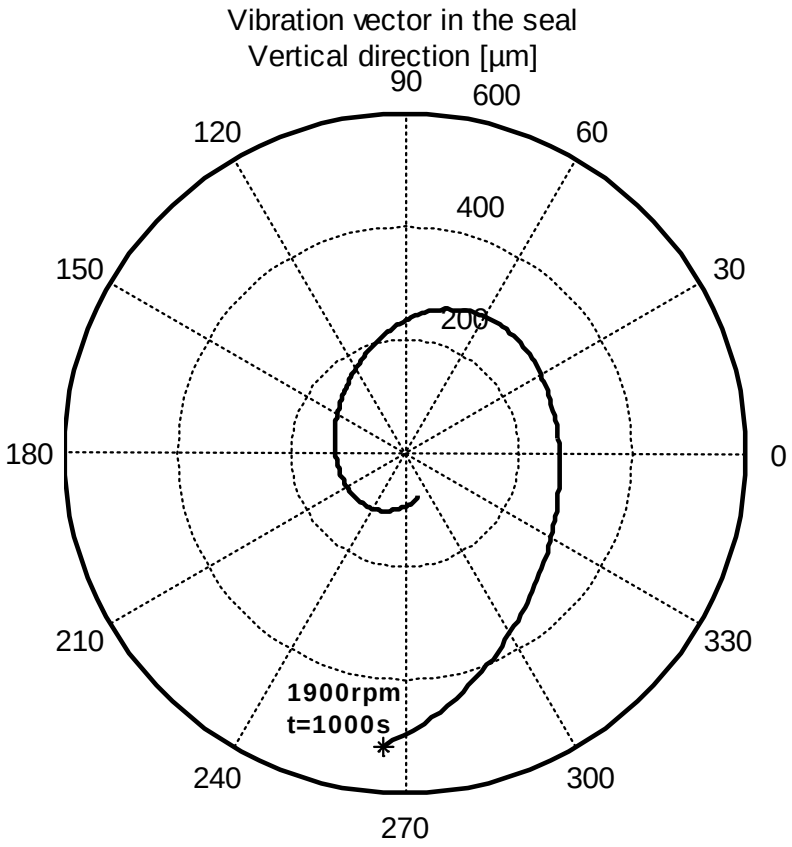

Figure 22. Polar plot of the vibration vector in vertical direction at 1900 rpm.

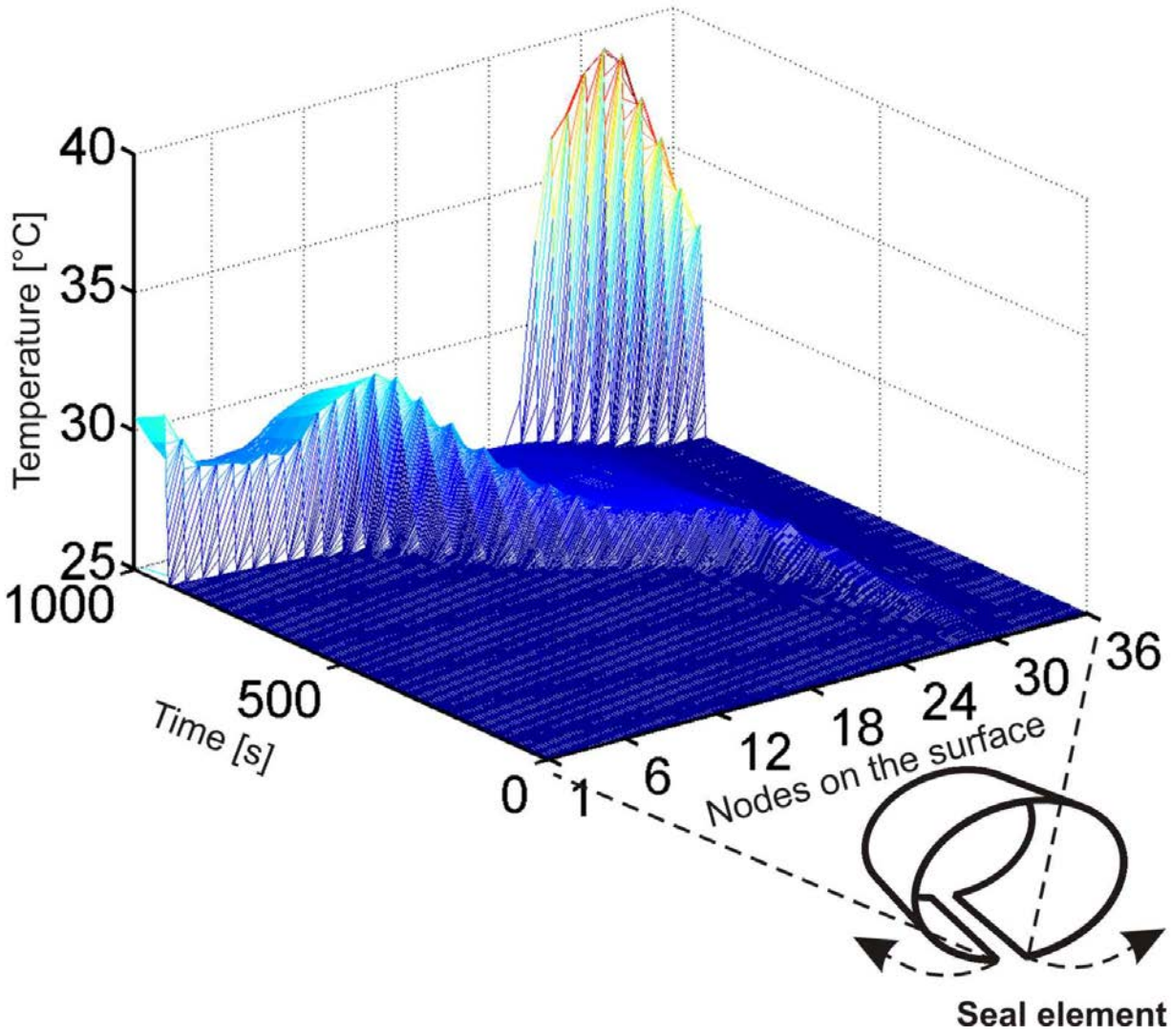

Figure 23. Temperature distribution on the rotor surface in the element rubbing to the seal.

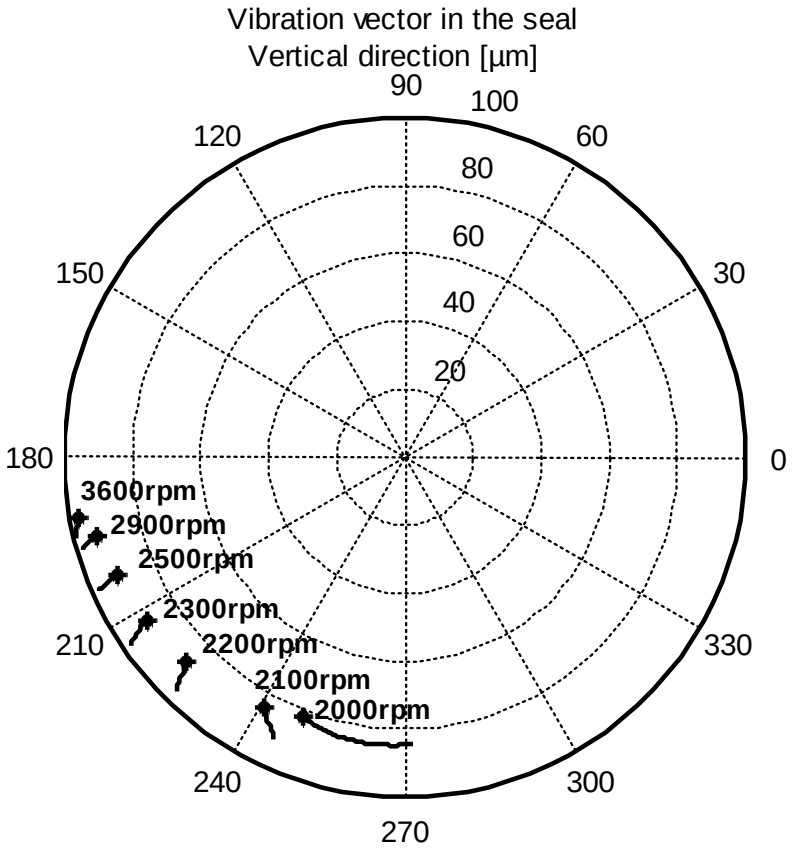

Figure 24. Polar plot of the vibration vector in vertical direction: speed range 2000-3600 rpm.

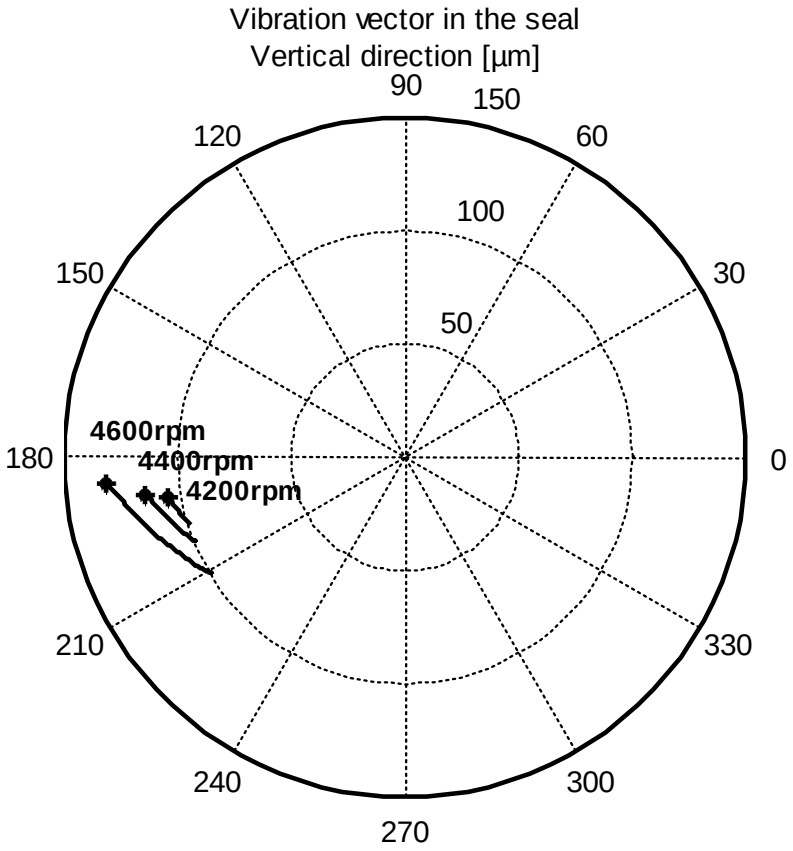

Figure 25. Polar plot of the vibration vector in vertical direction: speed range 4200-4600 rpm.

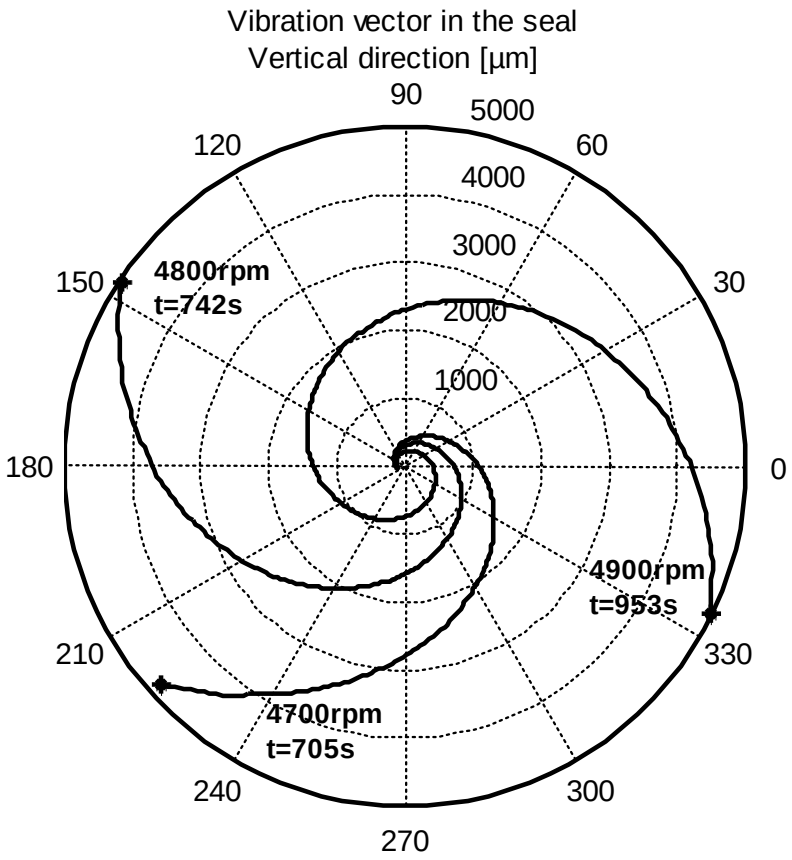

Figure 26. Polar plot of the vibration vector in vertical direction: speed range 4700-4900 rpm.

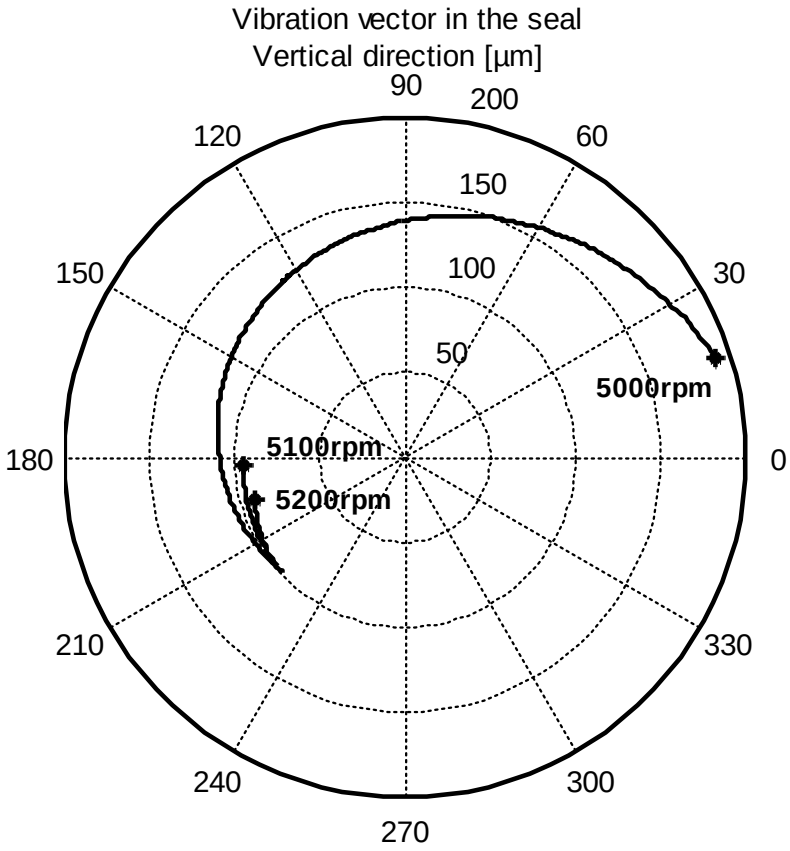

Figure 27. Polar plot of the vibration vector in vertical direction: speed range 5000-5200 rpm.

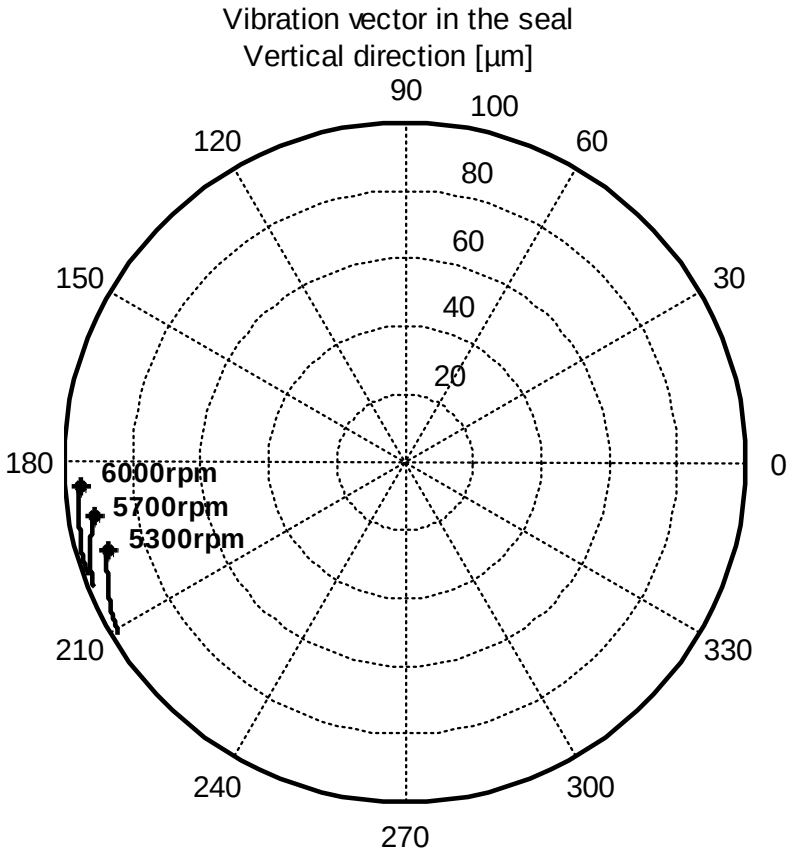

Figure 28. Polar plot of the vibration vector in vertical direction: speed range 5300-6000 rpm.

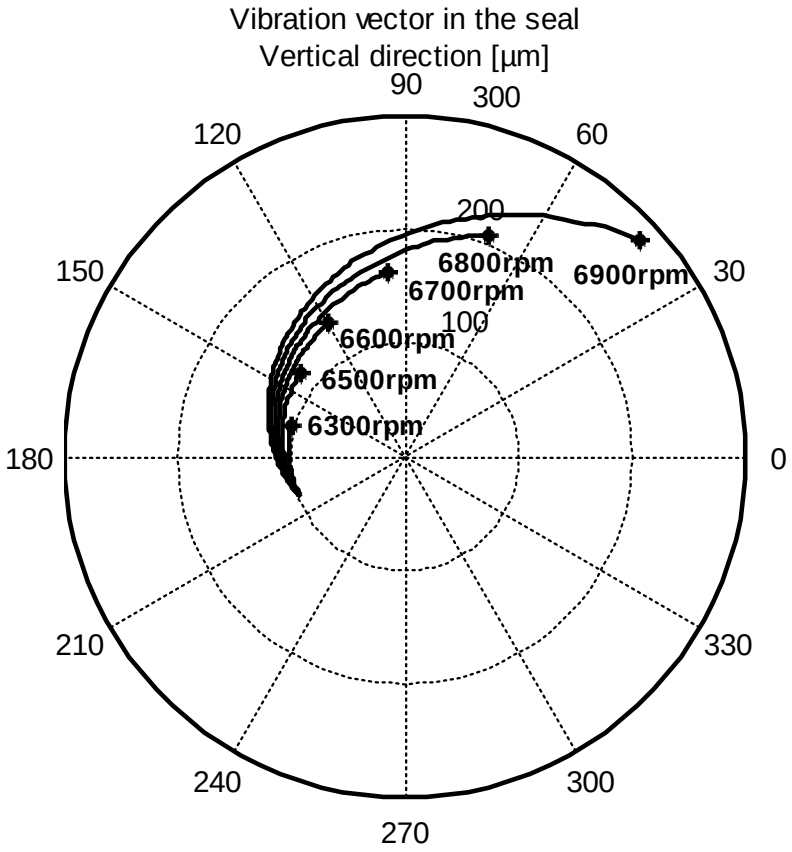

Figure 29. Polar plot of the vibration vector in vertical direction: speed range 6300-6900 rpm.

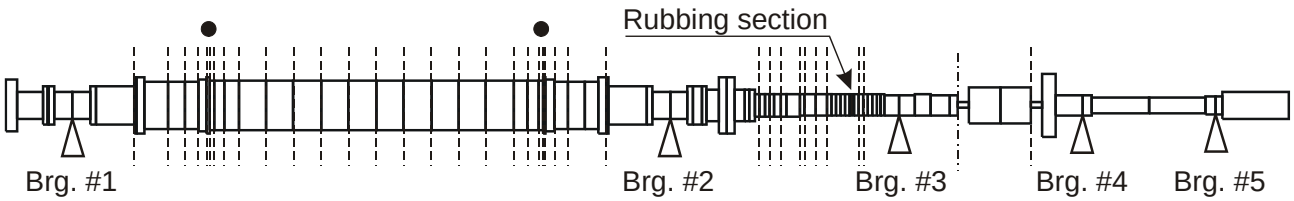

Figure 30. Generator model.

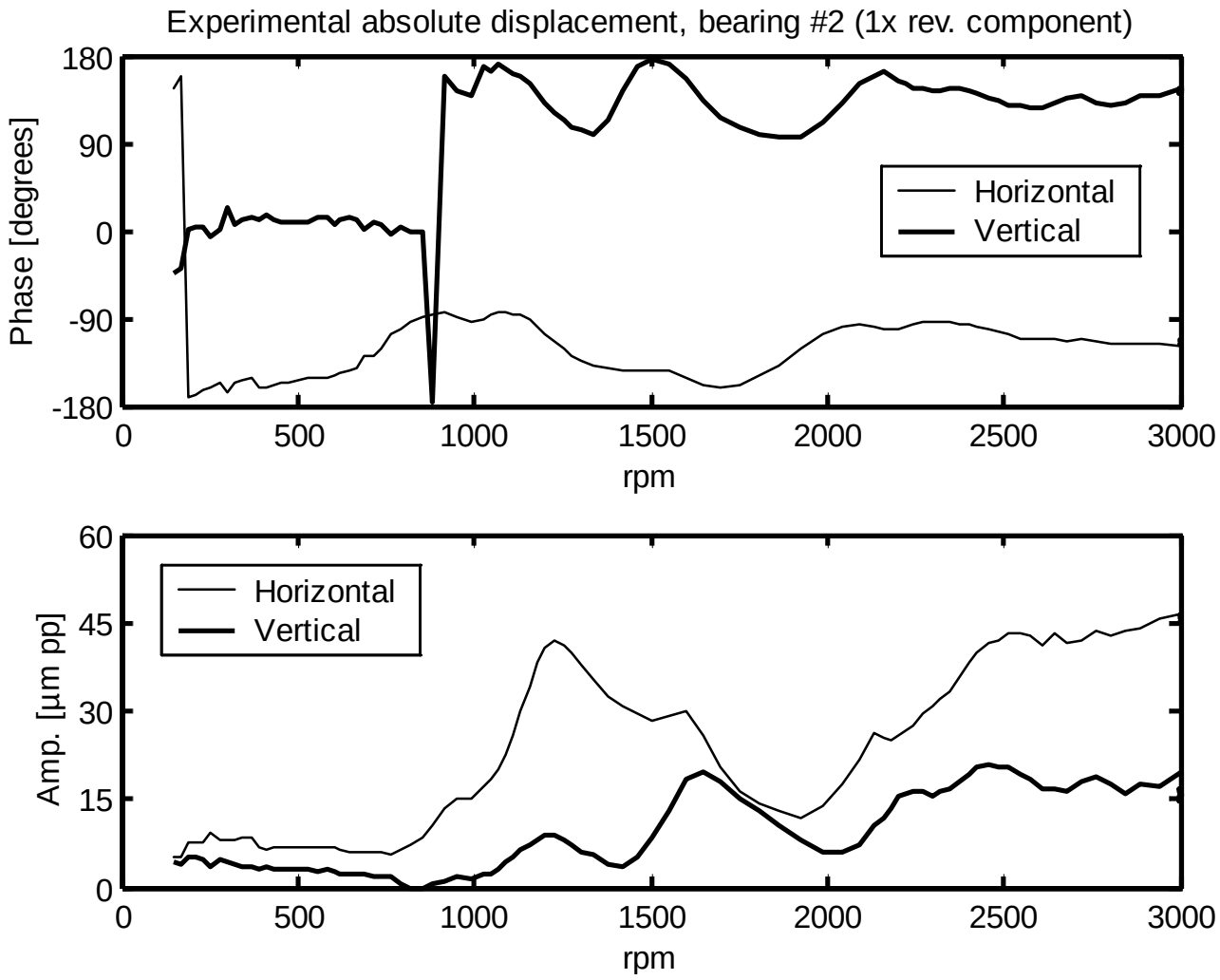

Figure 31. Experimental coast-down of the generator.

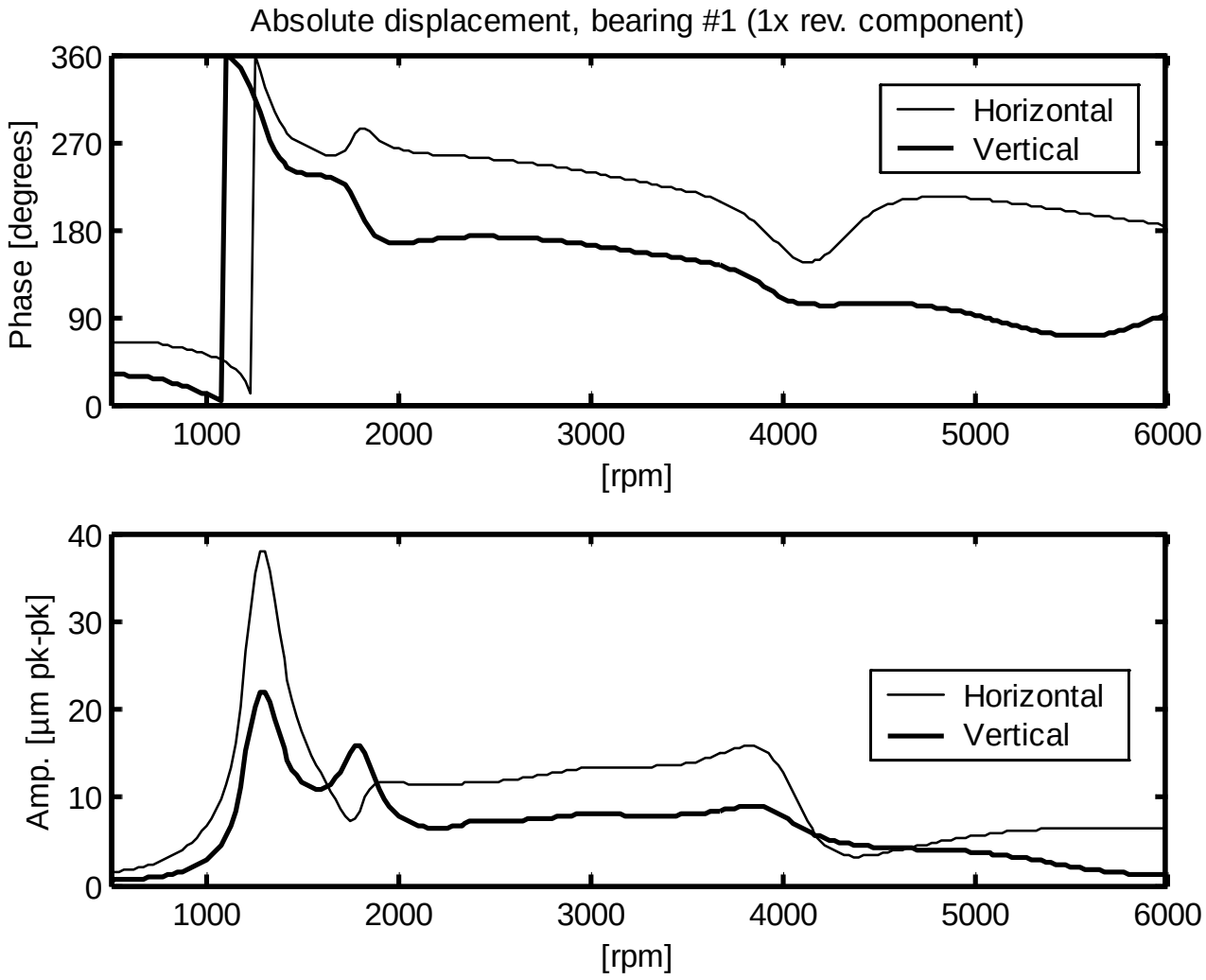

Figure 32. Frequency response due to unbalances in bearing #1.

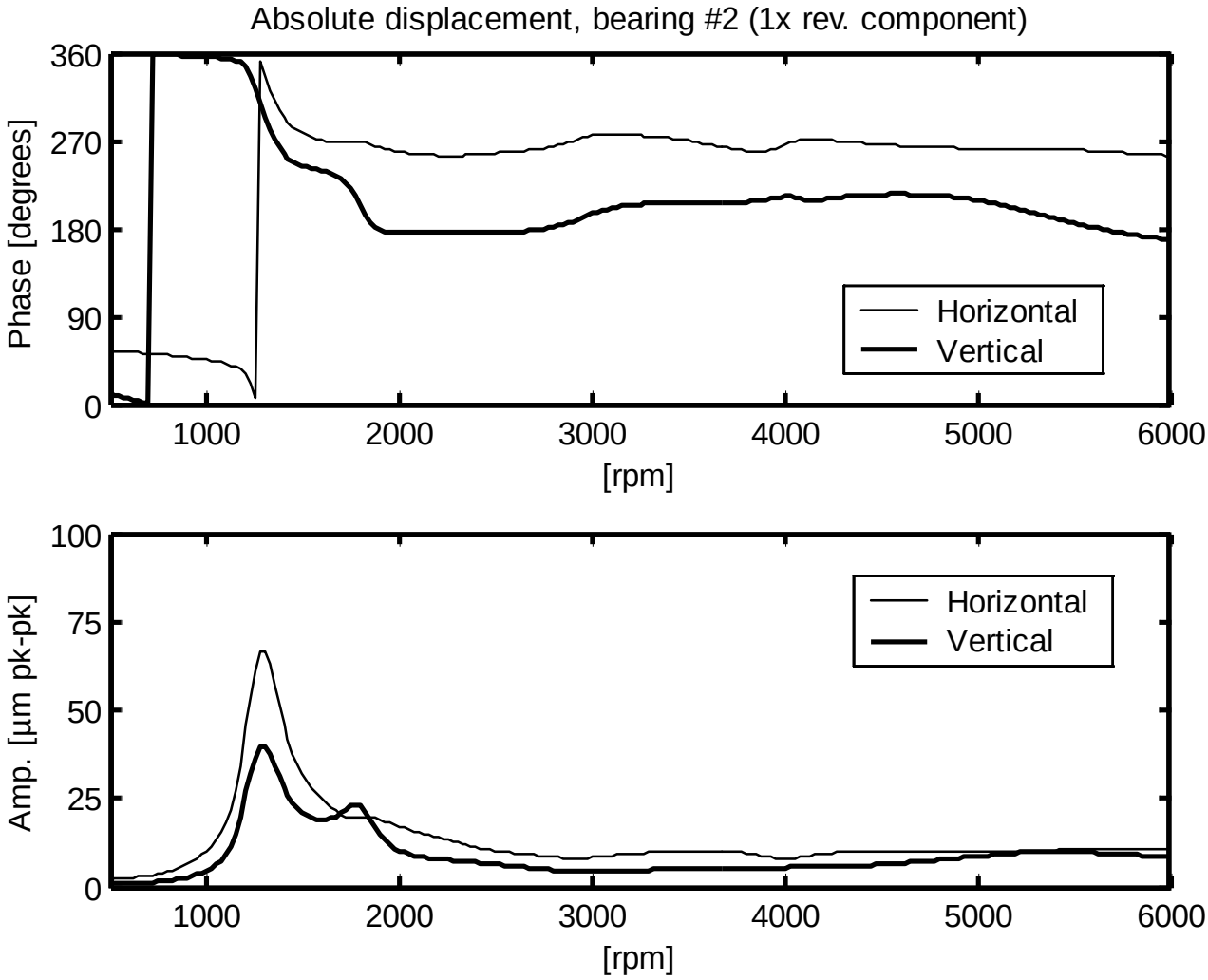

Figure 33. Frequency response due to unbalances in bearing #2.

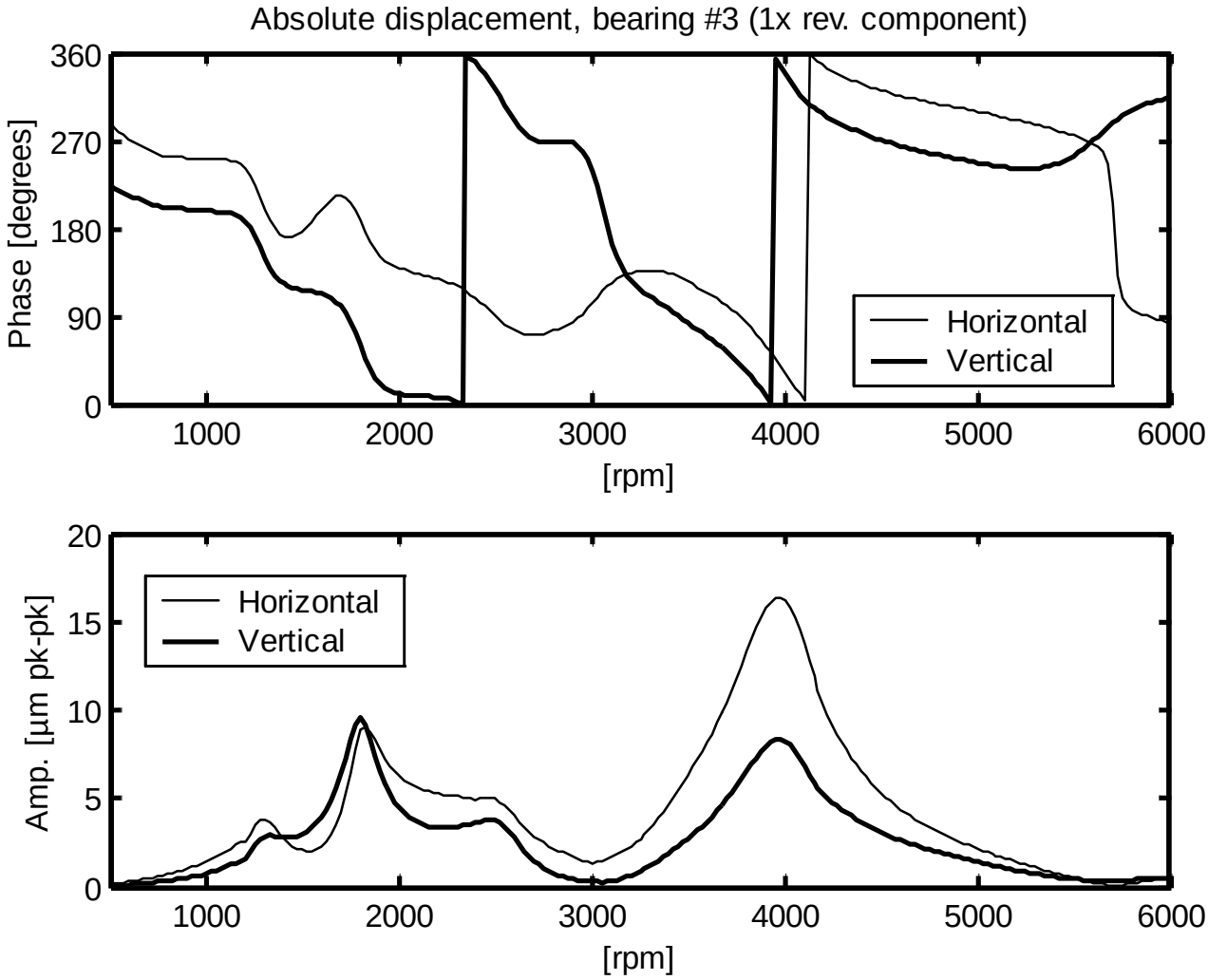

Figure 34. Frequency response due to unbalances in bearing #3.

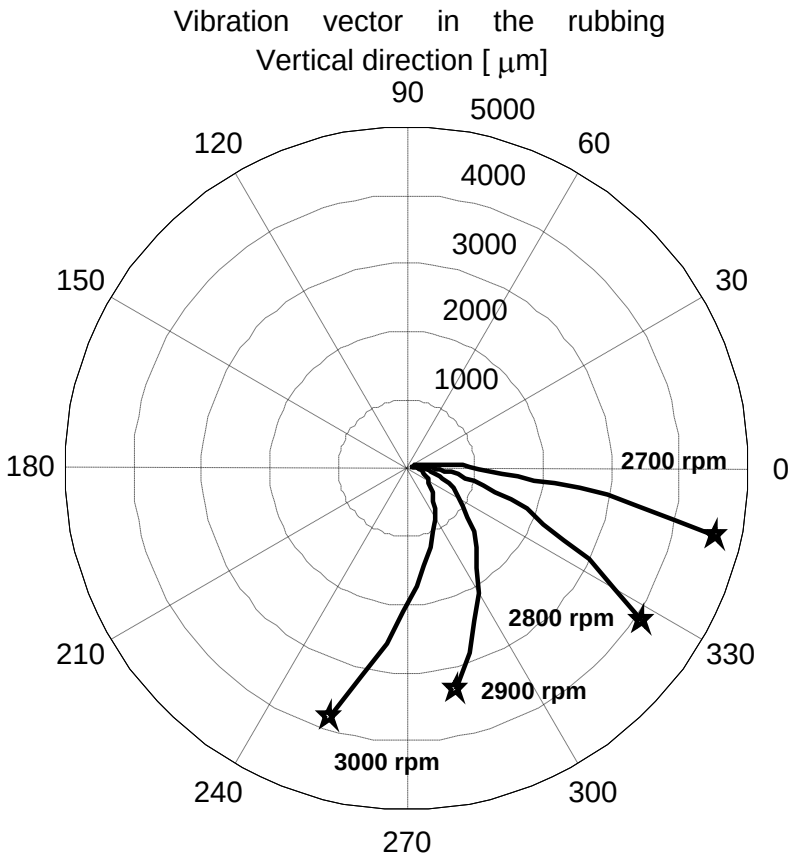

Figure 35. Polar plot of the vibration vector in vertical direction; speed range 2700-3000 rpm.

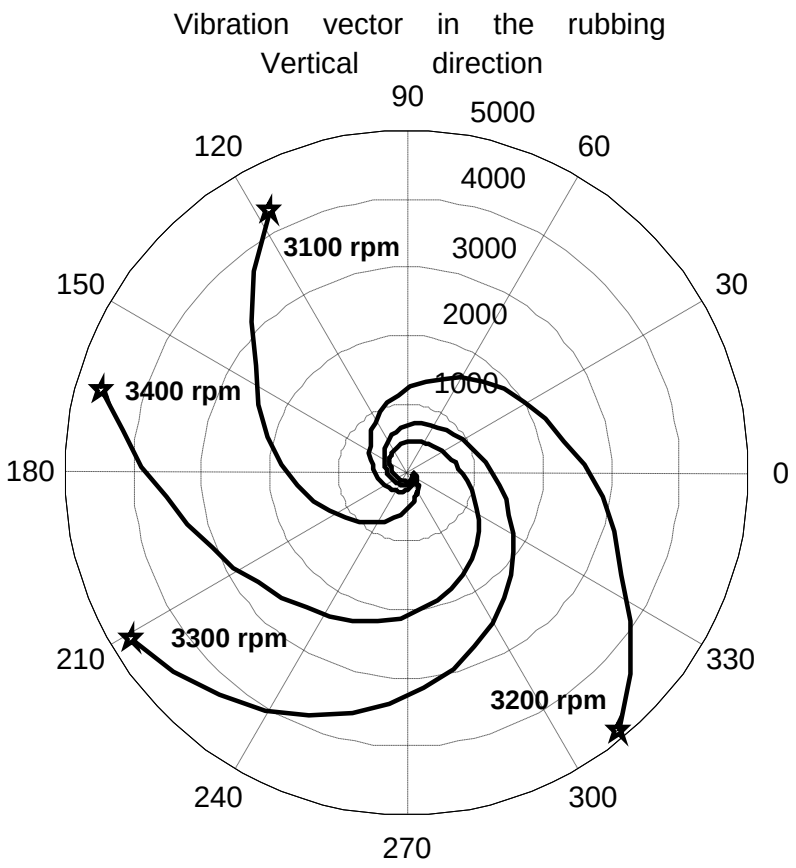

Figure 36. Polar plot of the vibration vector in vertical direction; speed range 3100-3400 rpm.

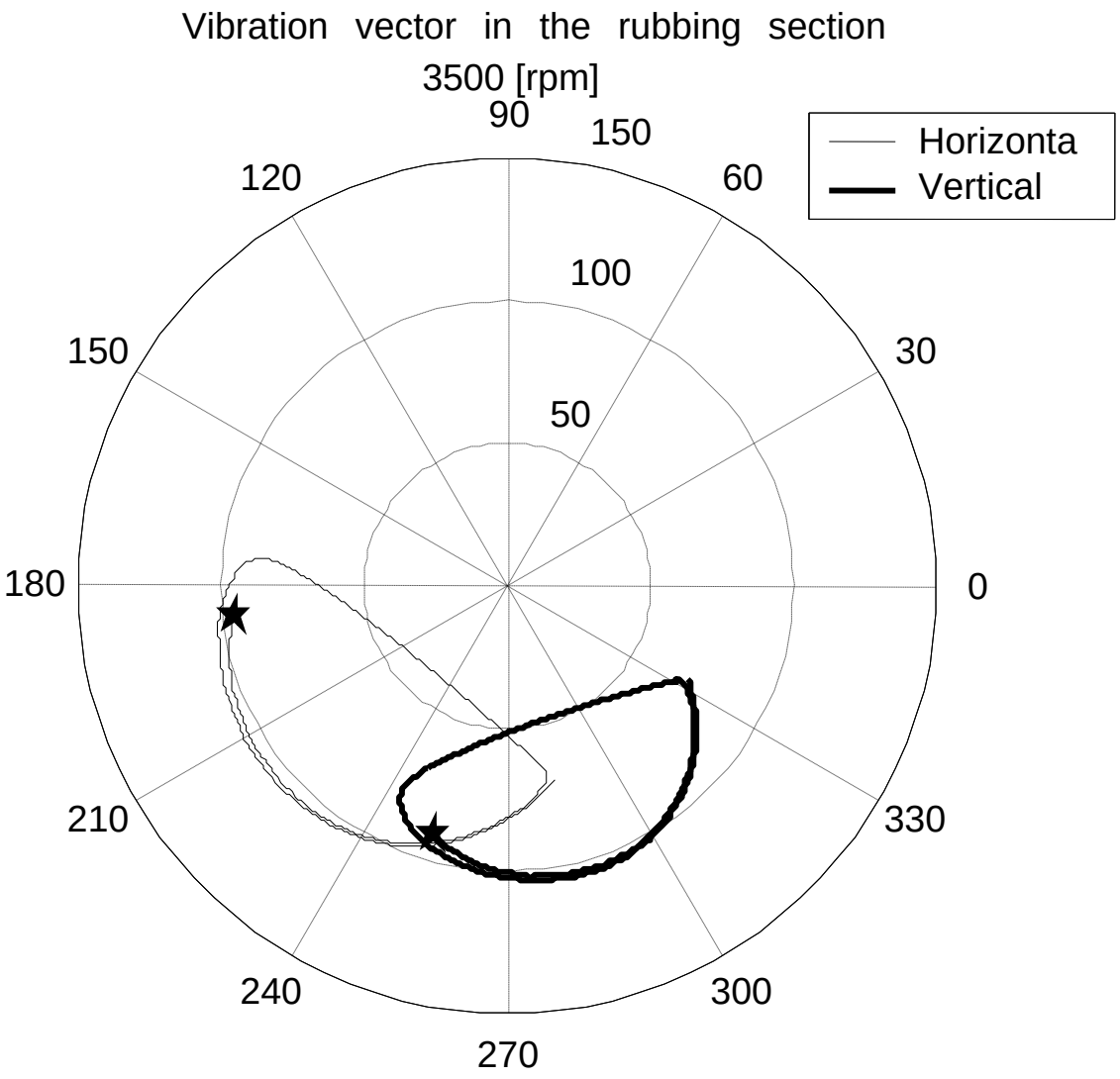

Figure 37. Polar plot of the vibration vector at 3500 rpm.

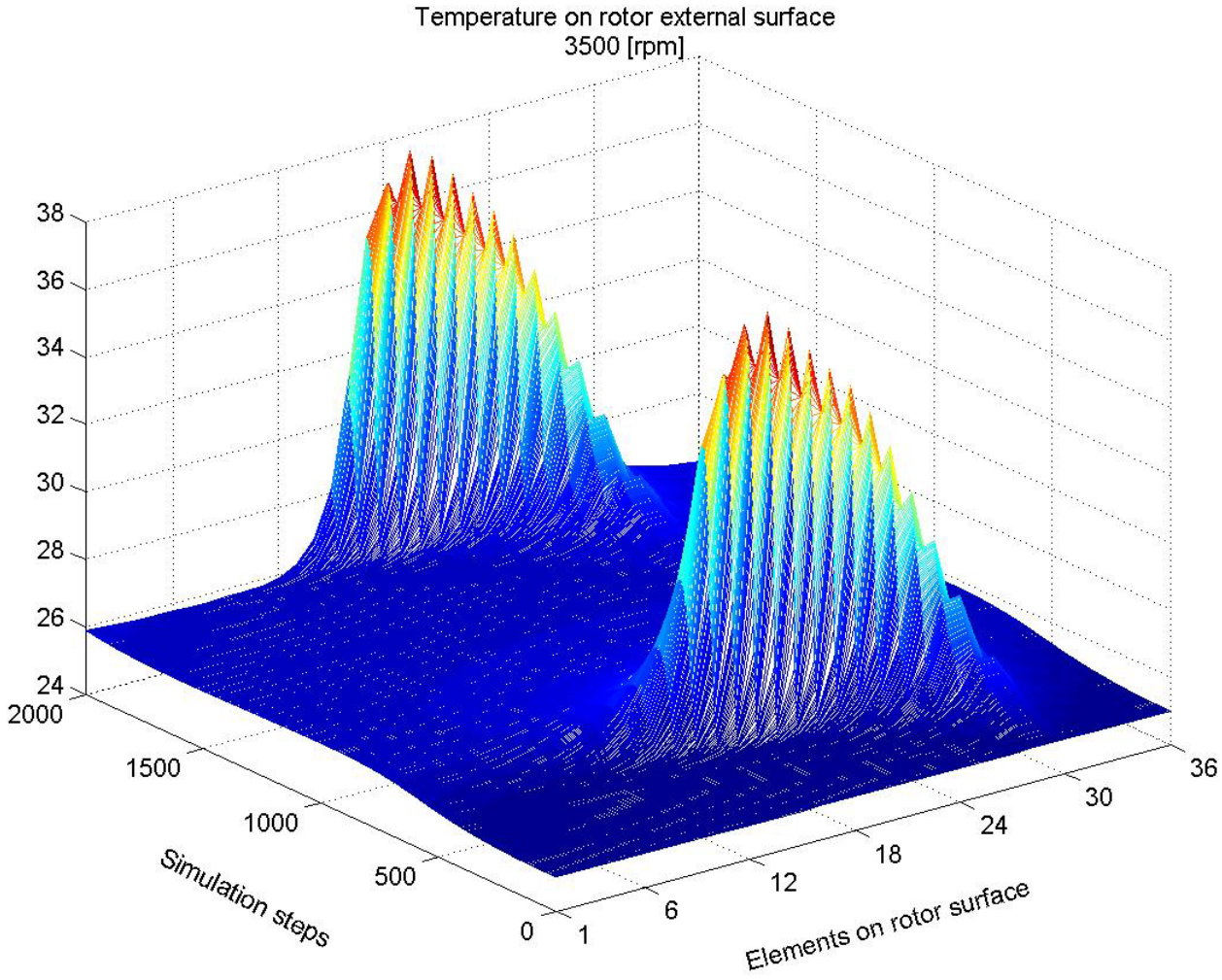

Figure 38. Temperature distribution on the rotor surface in the element rubbing to the rotor at 3500 rpm.

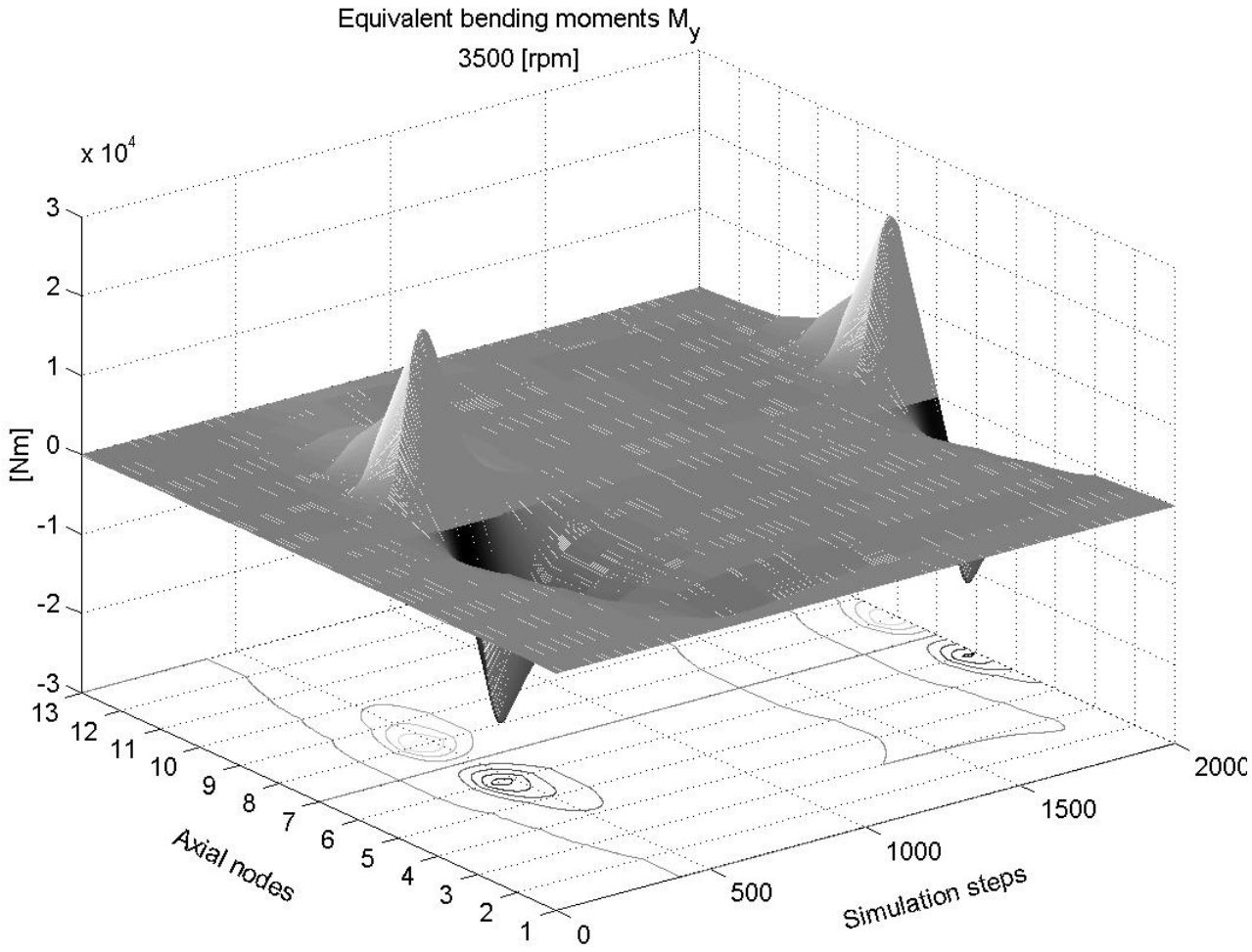

Figure 39. Equivalent bending moments in vertical direction at 3500 rpm.

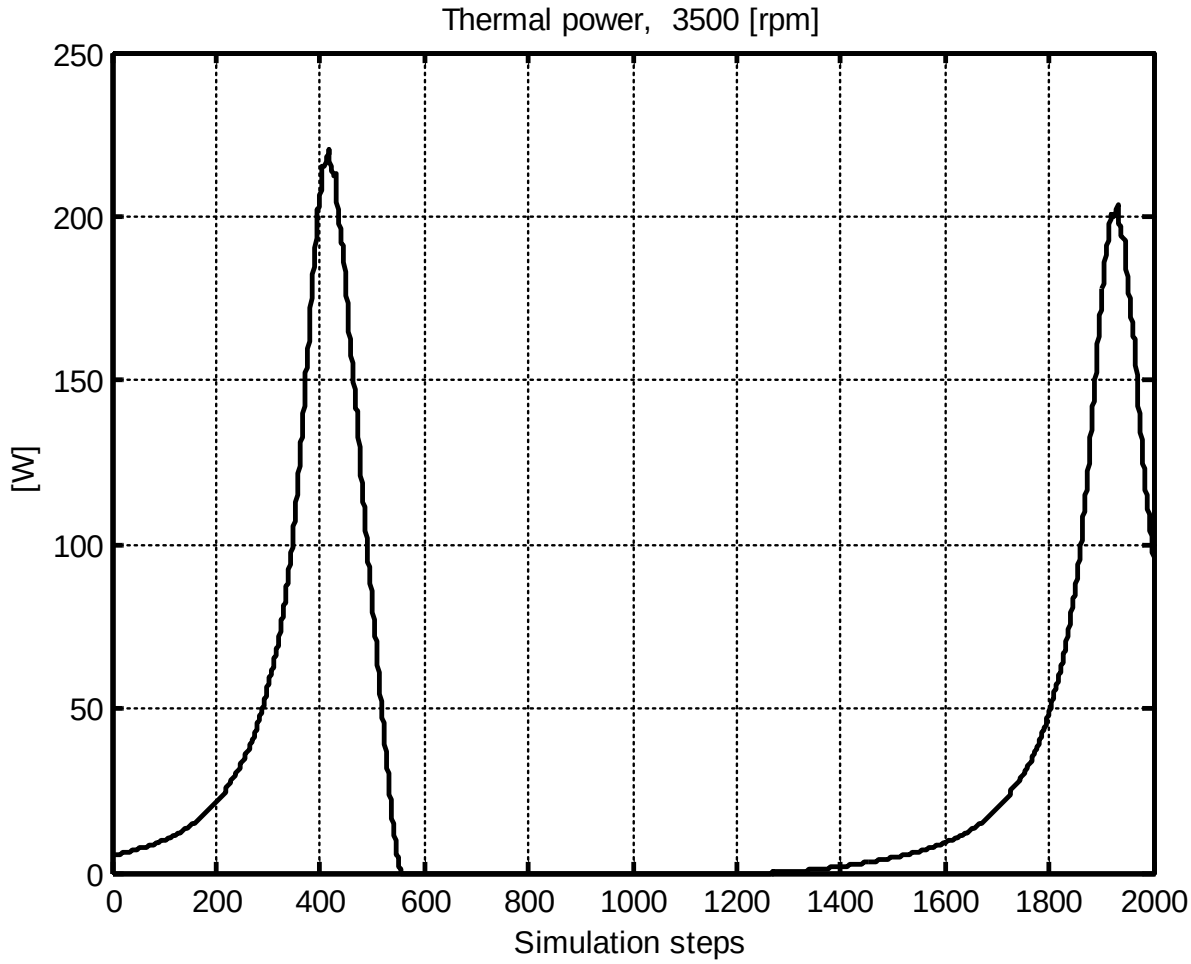

Figure 40. Thermal power introduced at 3500 rpm.

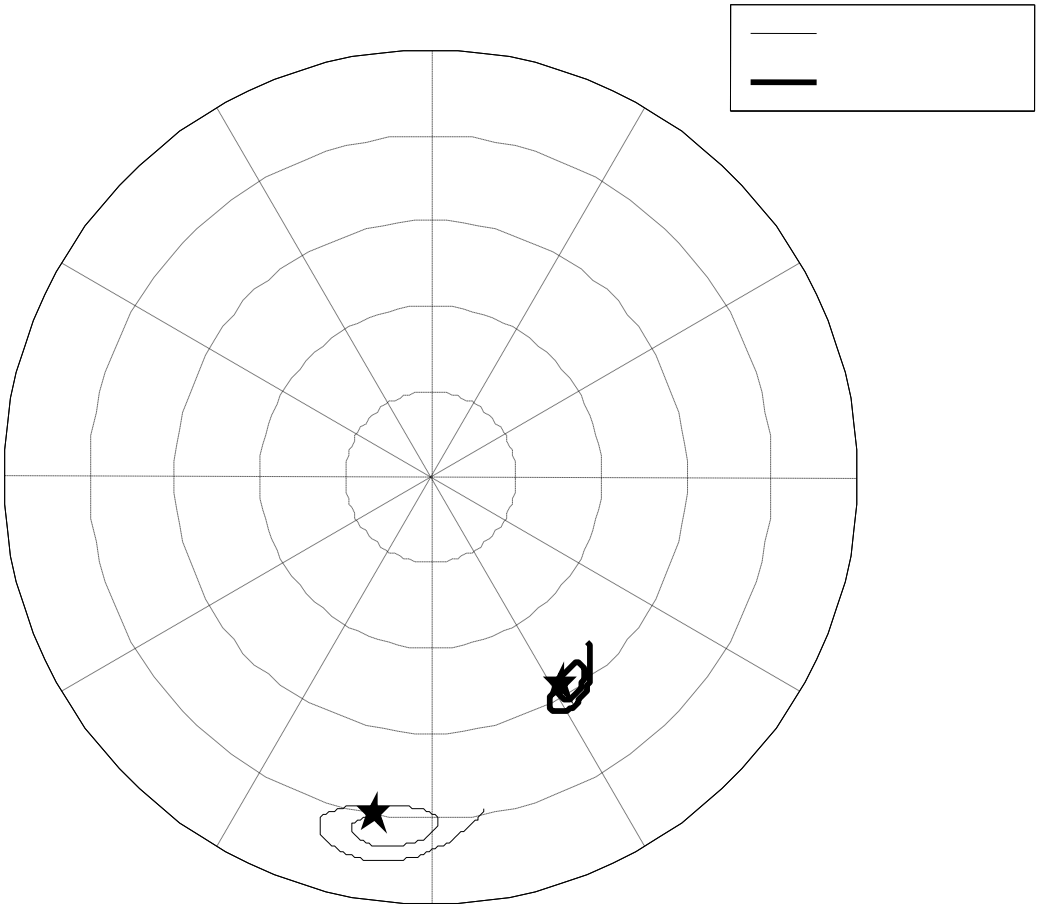

Figure 41. Polar plot of the vibration vector at 3700 rpm.

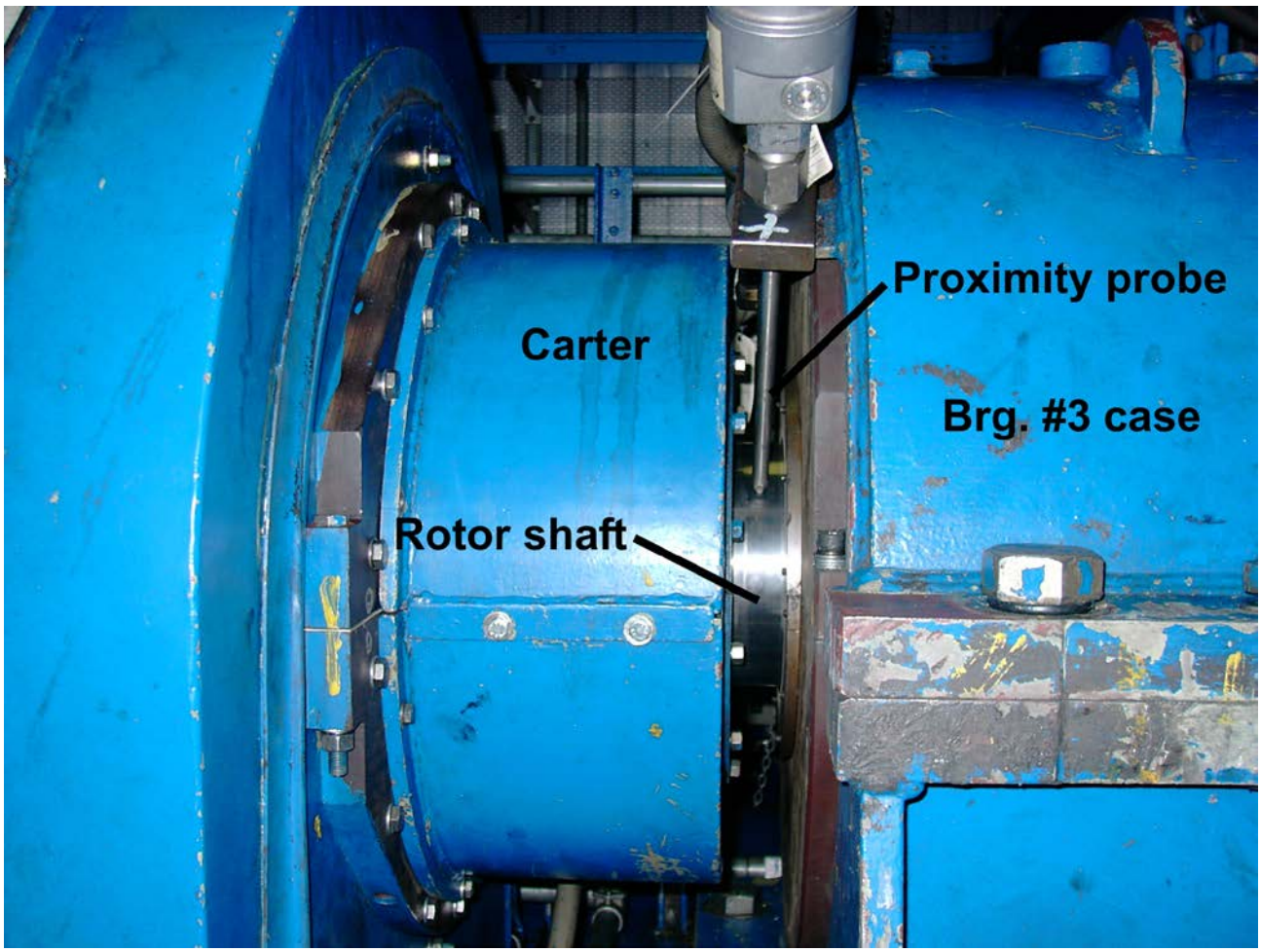

Figure 42. Close up of bearing #3 and carter sectors.

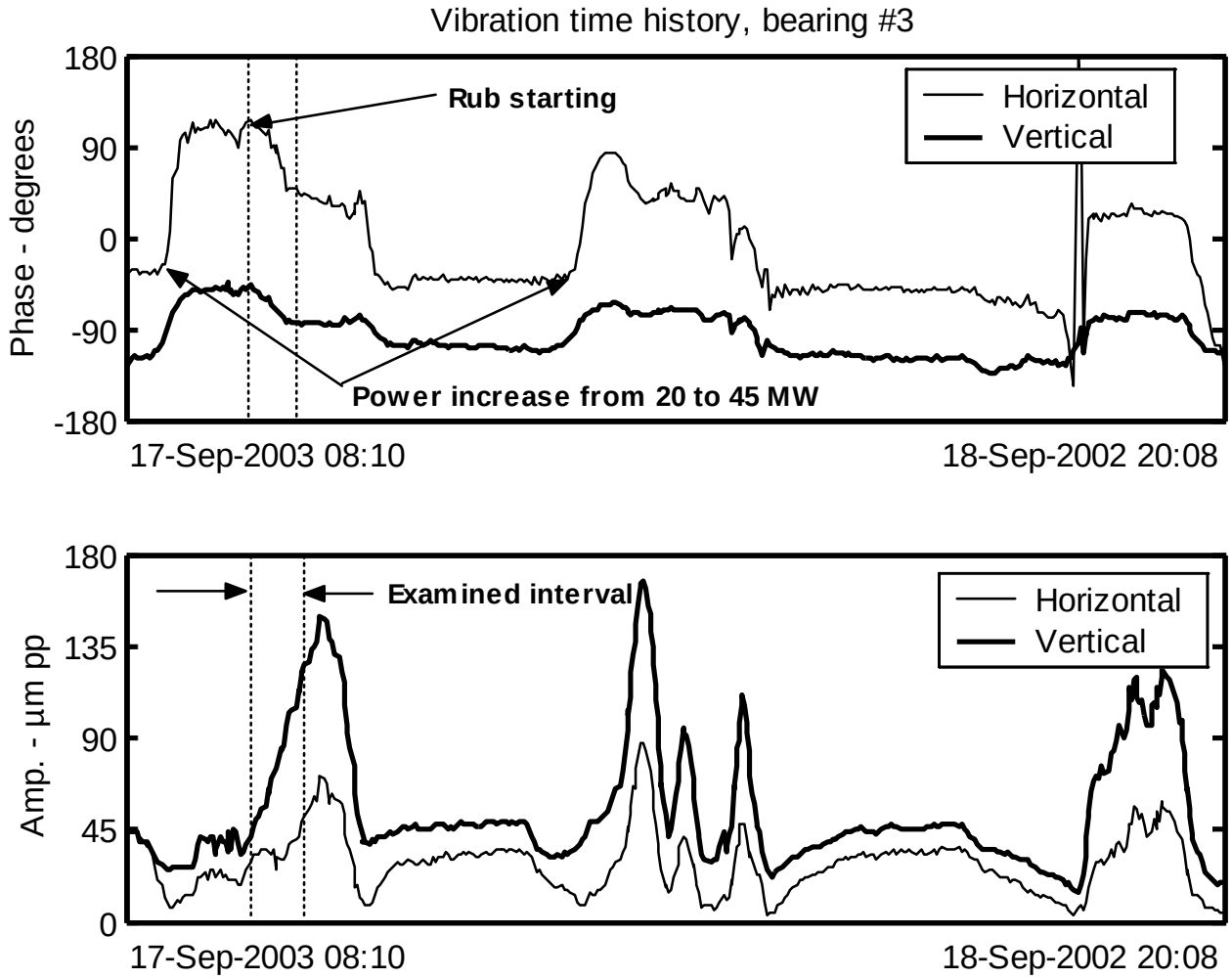

Figure 43. Time history of the vibration in bearing #3.

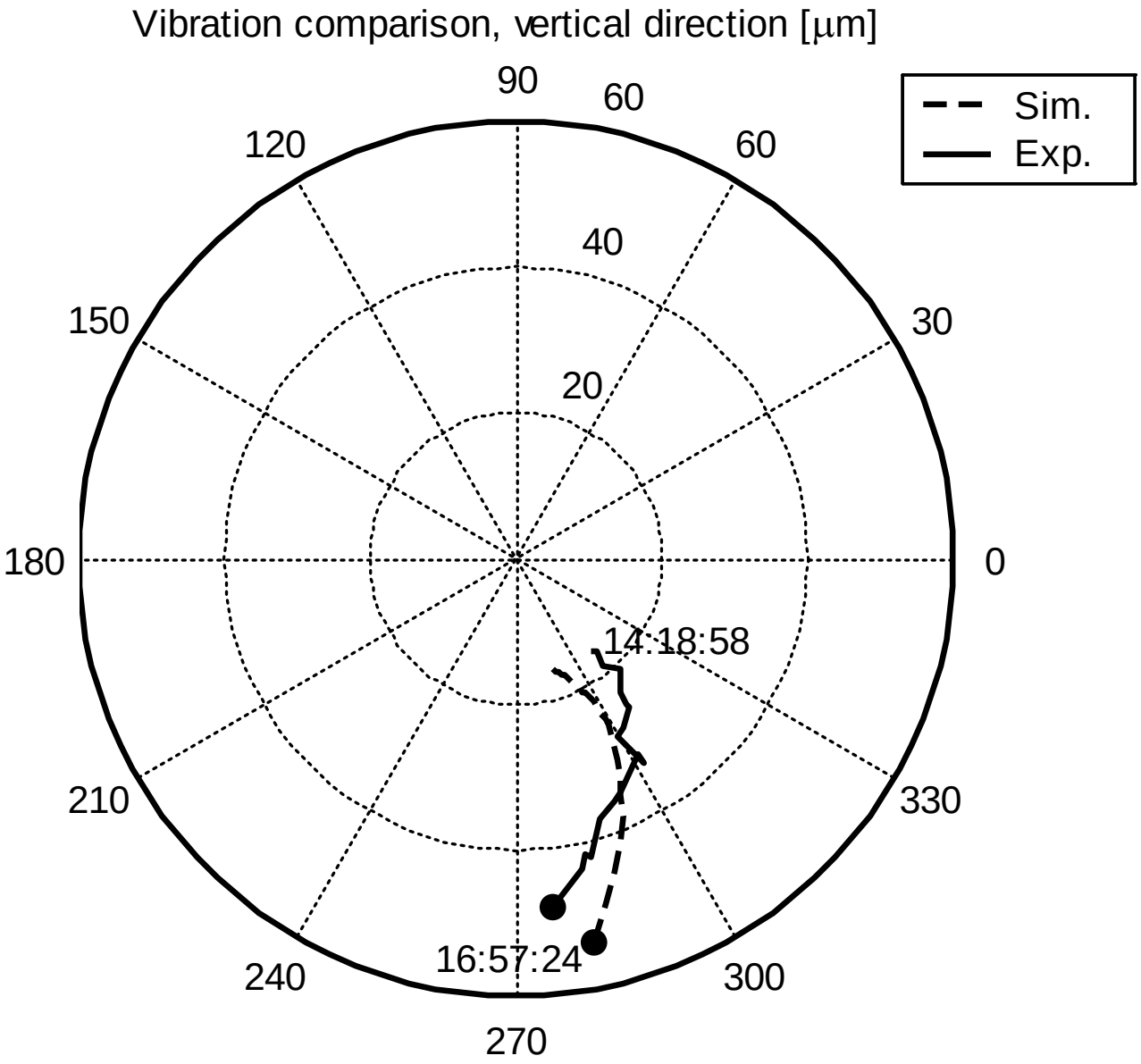

Figure 44. Comparison between experimental and simulated spiral vibration in the measuring section close to bearing #3 of the generator.

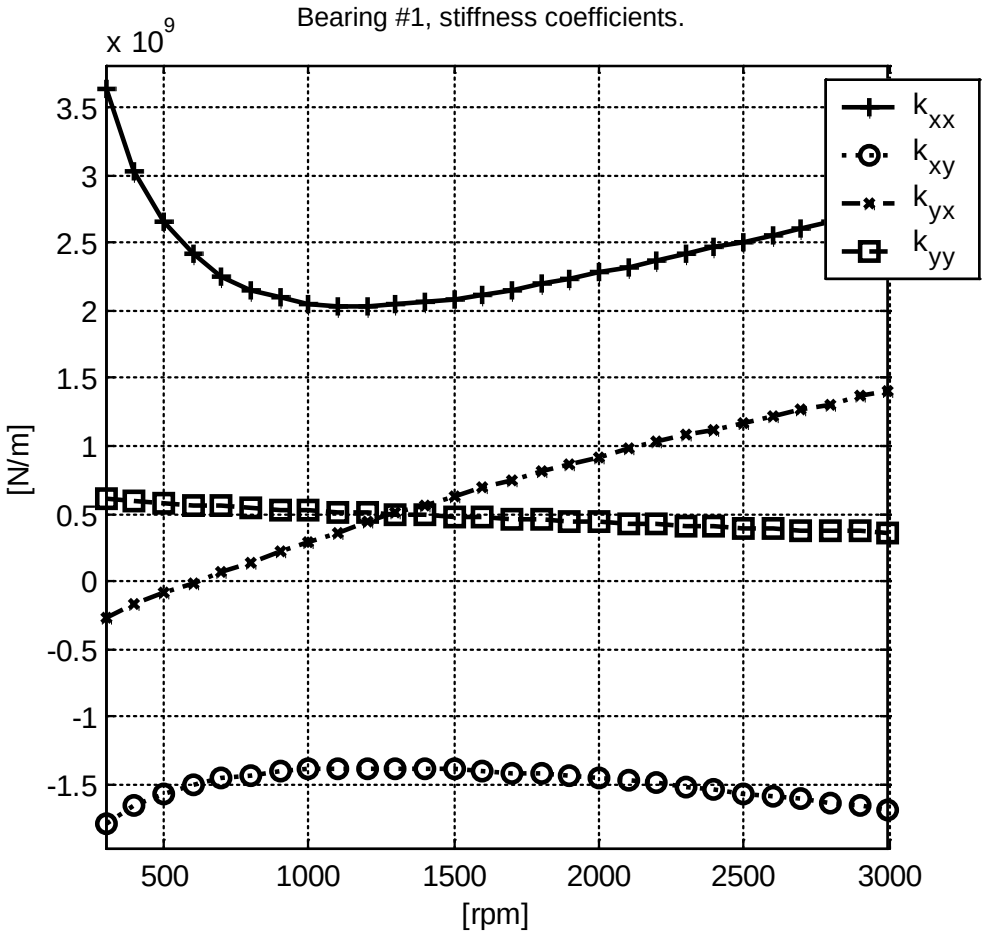

Figure 45. Stiffness coefficients of brg. #1 in the range 300-3000 rpm.

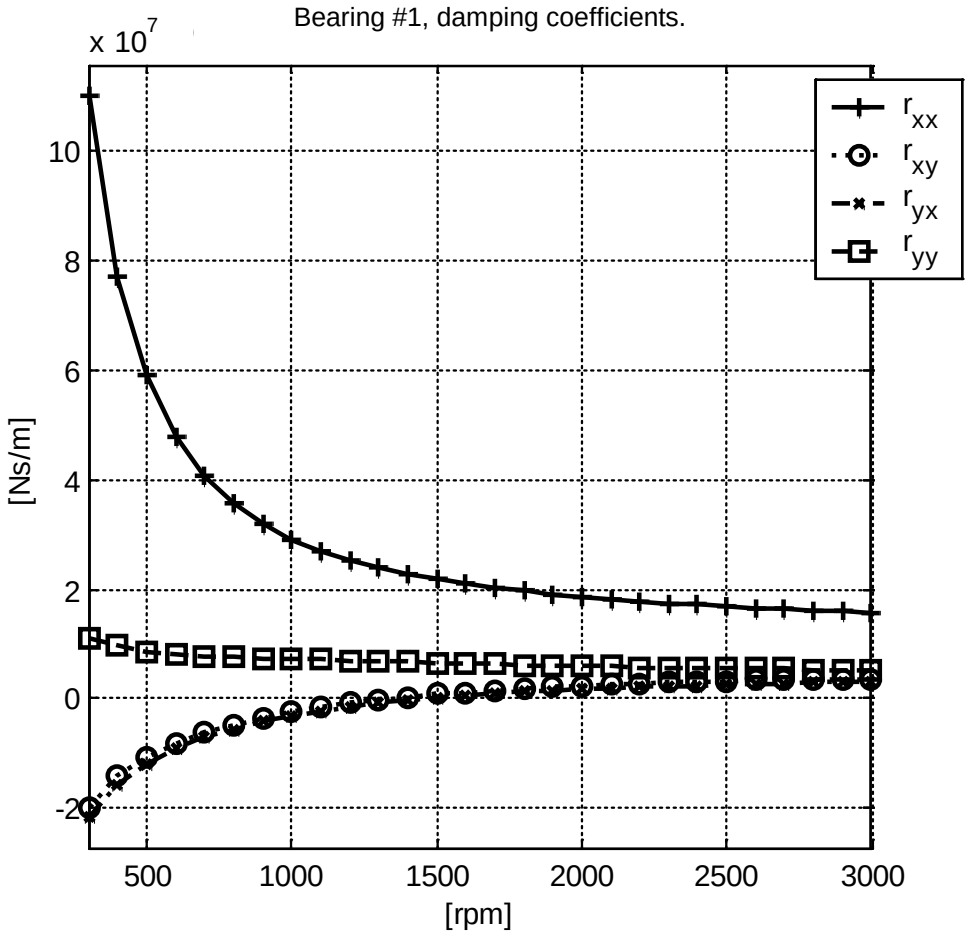

Figure 46. Damping coefficients of brg. #1 in the range 300-3000 rpm.

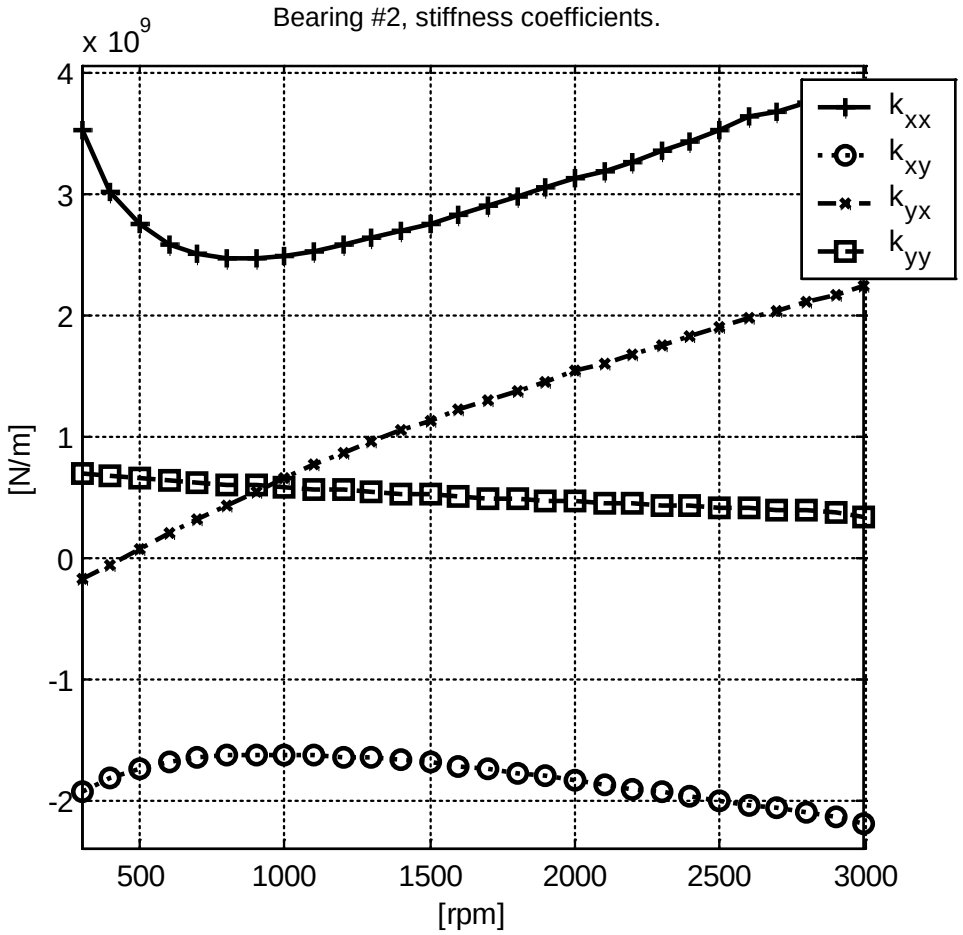

Figure 47. Stiffness coefficients of brg. #2 in the range 300-3000 rpm.

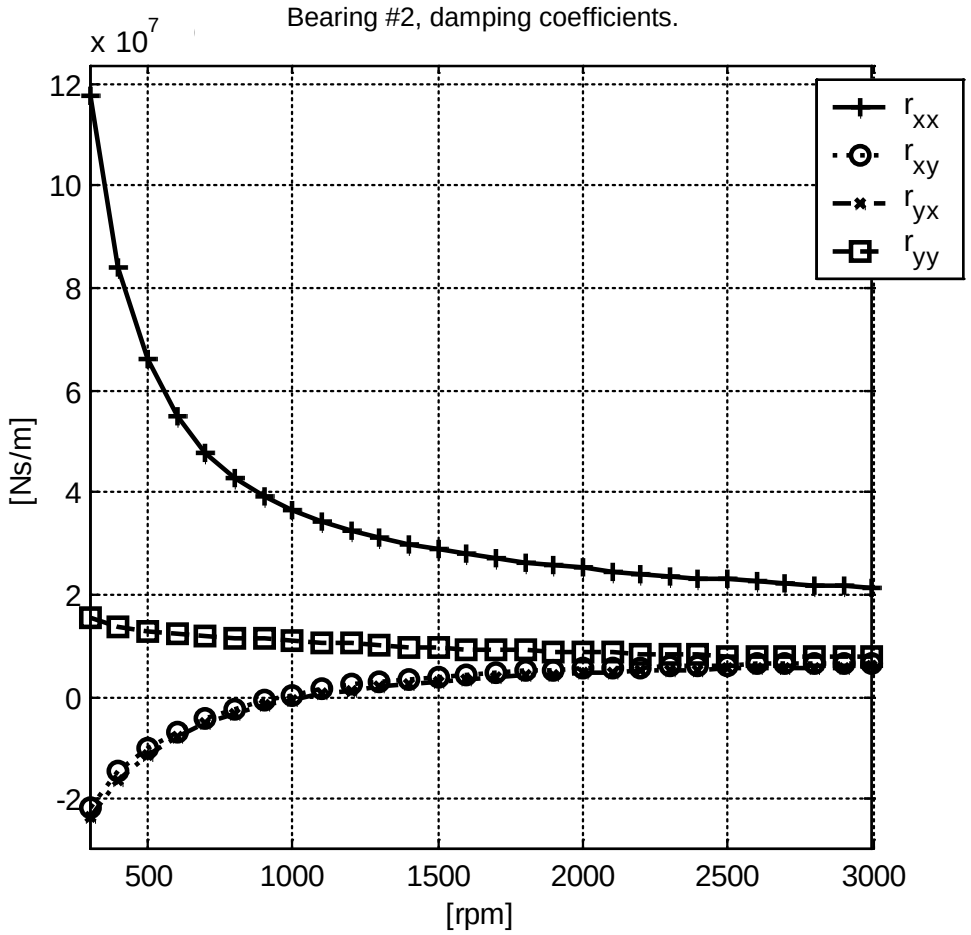

Figure 48. Damping coefficients of brg. #2 in the range 300-3000 rpm.